A physically based approach to simulate sub-grid snow depth and ground surface temperature distribution

Robin B. Zweigel

Thesis submitted for the degree of
Master of Science in Geoscience
60 credits

Department of Geosciences
The Faculty of Mathematics and Natural Sciences
University of Oslo

Department of Arctic Biology
The University Centre in Svalbard

June 2020

I now walk into the wild

Abstract

The ground thermal regime in most cold environments is during winter governed by the unique properties of snow. In the Arctic and other tree-less regions, the redistribution of snow through wind drift gives a highly non-uniform distribution of snow depths within the landscape. In addition, snow metamorphism and lateral water percolation produce local variations in snow density. These processes are controlled by small-scale topography, and the snow cover can exhibit large spatial variability within landscapes that are subject to rather uniform meteorological forcing. As the snow cover exerts a strong control on energy exchange between the atmosphere and the ground, substantial spread in ground surface temperature are observed in areas subject to snow redistribution. However, the grids of current climate- and weather models are not capable to resolve these processes, and land surface models are thus limited in their ability to simulate the thermal dynamics of these regions.

This study aims to alleviate the scale gap between available near-surface meteorological data and ground observations. Parameterizations of snow microphysics from the detailed snow scheme CROCUS are added in a tiled version of the CryoGrid permafrost-modelling framework. Sub-grid lateral exchange of snow and water is implemented among the simulated tiles in a process-based fashion. These amendments allow for a transient, spatially variable, buildup and ablation of the snow cover not possible in standalone simulations. The approach is compared against a comprehensive dataset of snow properties and ground surface temperatures from the Bayelva area on Svalbard, for the last three snow seasons. Simulating this area by three tiles, representing different topographic settings, successfully reproduces the observed end-of-season snow distribution and spread in wintertime ground surface temperatures.

The capabilities of this setup are further explored for sites in the Norwegian Arctic. It is evident that the approach is limited to simulating the entire system within which exchange of snow and water occurs. However, periglacial landforms such as nunataqs and palsas are successfully reproduced. The setup shows potential for simulation of sub-grid variability in a climate change context, and potential applications extend over disciplines such as permafrost research, ecology and hydrology.

Acknowledgements

I want to extend a thank you to all my supervisors, who despite having different backgrounds and interest in my MSc work, allowed it to be shaped according to my abilities and interests. A special thank goes to Sebastian Westermann, whose assistance exceeded what I could expect from a main supervisor. Apart from the guidance regarding the development of the model, his support in acquiring an Arctic Field Grant, planning the field campaigns, participation at SSC2019 and the 2nd CryoGrid hackathon, and submission of a manuscript, are noteworthy.

Indeed, all the co-authors for said manuscript deserve credit: Sebastian Westermann, Jan Nitzbon, Moritz Langer, Julia Boike, Bernd Etzelmüller and Thomas Vikhamar Schuler. Thank you for helping a novice master student through the process of writing and submitting a manuscript!

Also, I want to extend my gratitude to my field assistants: Joscha Sommerkorn (spring campaign) and Julia Boike (autumn campaign). It was a pleasure to stay in Ny-Ålesund with you, and your help was paramount when collecting data from the field. During the writing part of my MSc, my thoughts have often drifted back to our joint experiences in these wonderful surroundings.

The role of the University Center in Svalbard (UNIS), where I am a guest student, needs also to be acknowledged. The field based teaching offered at UNIS was essential to trigger my interest in integrating observations and modelling of snow. I am grateful for the opportunity to spend three terms in Longyearbyen, and for all the friendships I've made there.

On the note of friendship, I want to mention my fellow students in room 217 in ZEB. Thank you for the good times, especially all the "fredagstaco" – too sad we could not continue the tradition to the end.

I also want to thank my parents, who have supported me through my studies in numerous ways. My recent decision to move back to Trondheim during the corona situation has proven almost surprisingly enjoyable. Thank you for the "kontorfellesskap", the good food and the moral support!

Til endans, so ynski eg at takka mín føroyska dama, Rakul. Eg kann ikki ímynda mær hvussu tað síðsta árið hevði verði uttan teg.

Table of Contents

Abstract ii

Acknowledgements iii

Note on terminology 1

List of abbreviations 2

1 Introduction 3

- 1.1 The role of snow in the Earth system 3
- 1.2 Motivation, aims and objectives 5

2 Background 6

- 2.1 Snow 6
- 2.2 Land surface models 9
- 2.3 Parallel computing 10

3 Methods and data 11

- 3.1 Study area 11
    - 3.1.1 Geography 11
    - 3.1.2 Climate 11
    - 3.1.3 Permafrost history 13
    - 3.1.4 Study sites 13
- 3.2 Data 19
    - 3.2.1 Field observations 19
    - 3.2.2 Forcing data 21
- 3.3 CryoGrid framework 23
    - 3.3.1 Numerical structure 24
    - 3.3.2 Snow scheme 25
    - 3.3.3 Lateral exchange of water and snow 32
    - 3.3.4 Derivation of surface runoff 35
- 3.4 Model setup 35

3.4.1 Bayelva 35
3.4.2 Nordenskiöld land 38
3.4.4 Garwoodtoppen 39
3.4.3 Suossjavri..39
4 Results..40
4.1 Process-based lateral redistribution SWE..40
4.1.1 Example events of snow and water exchange..40
4.1.2 Surface runoff..43
4.2 Validation study..45
4.2.1 Sub-grid evolution of snow depth and SWE 45
4.2.2 Sub-grid evolution of ground surface temperatures 47
4.2.3 Sensitivity of CG Crocus to drift factor..51
4.3 Further results – exploring applications 53
4.3.1 Elevation gradients, Nordenskiöld land..53
4.3.2 Observed landforms: Nunataqs..55
4.3.3 Observed landforms: Palsa mire..56
5 Discussion..58
5.1 Representation of snow processes in CG Crocus..58
5.2 Representation of spatial variability in CG Crocus..60
5.3 Practical limitations 64
5.4 Outlook..68
6 Conclusions 72
Reference list 73
Appendix..80
Other elements of the MSc work 80
Poster, Svalbard Science Conference 80
Submitted manuscript, JGR – Earth Surface 80

Note on terminology

This study focuses on the modelling of snow, and to avoid confusion, a clarification of relevant terms regarding both snow and the models is given.

CROCUS – The detailed snowpack scheme presented in Vionnet et al. (2012).

Crocus scheme – the new snow scheme presented in this study, which includes parameterizations from CROCUS.

CG Crocus – The version of CryoGrid used in this study.

Snow erosion – the removal of snow from the ground by the wind.

Snow bed – a terrain feature where above average amounts of snow accumulate in winter.

Drifting snow – snow in the process of being transported by the wind, regardless of transport mode and vertical extent.

Drift event – a time where meteorological and snow conditions allow snow to be transported.

Snow redistribution – erosion and deposition of snow already on the ground

List of abbreviations

AL – Active layer

ELA - Equilibrium line altitude

ESM – Earth system model

fSCA – Fractional snow-covered area

GCM – General circulation model

GST – Ground surface temperature

LSM – Land surface model

MAGST – Mean annual ground surface temperature

NH – Northern hemisphere

NWP – Numerical weather prediction

ROS – Rain-on-snow

SEB – Surface energy balance

SWE – Snow water equivalent

1 Introduction

1.1 The role of snow in the Earth system

The Earths snow cover is acknowledged as an important element of the climate system, both through its unique properties and through its interaction with the other elements of the Earth system (IPCC, 2018; Pörtner et al., 2019). Its most influential properties include the high albedo and the low thermal conductivity, which distinctively modify the Earth's surface energy balance (SEB) compared to the surface material it overlies. Snow is also a key element of the cryosphere, having decisive influence on most of its components (see Vaughan et al., 2013). In some cases the effect is categorical, e.g. snow is essential to nourish glaciers and ice sheets, and summer snow cover reduces their melt rates. In other cases snow has a equivocal impact; a moderate snow cover will hamper sea ice growth while heavy loads lead to submergement and subsequent accelerated growth. The insulating properties of snow are also of central importance for perennial frozen ground (permafrost), which currently stores great carbon stocks (ca. 1700 PgC; IPCC, 2018). While snow cover can slow down the freezing of the active layer (AL) and protect the permafrost from overlying, cold air masses, it can also reduce the heat transfer from warm air. Which of these effects dominate is subject to the thickness and duration of the snow cover, and the timing of snowfall. Snow has also been recognized as the variable of principal importance for the distribution of vegetation in alpine and arctic environments, with distinct plant communities along the gradient from windblown areas to snowbeds (Walker et al., 2001). Changes in snow cover thus have a complex impact on the climate system, with the direct effects superimposed by its influence on other elements of the Earth system.

The unprecedented warming of the climate system over the last decades is accompanied by observations of a clear reduction in snow cover (IPCC, 2018). Brown et al. (2017) report a significant decline in Arctic snow cover, and attribute this to polar amplification of climate change, and the snow-albedo feedback. Indeed, the Arctic is the region where current climate change is most pronounced, warming close to twice the global rate (Osborne et al., 2018). Future projections also indicate that rain will become the dominant form of precipitation in the Arctic (Bintanja & Andry, 2017) and that the frequency and intensity of winter warming events will increase (Vikhamar-Schuler et al., 2016). This will entail major changes to the regional snow climate, making extrapolation of current snow relationships for future scenarios problematic. In the pursuit of reliable predictive capabilities, it is thus of major importance to include the effects changes in climate have on snow properties.

The distribution of snow within a landscape is generally variable, being the result of complex interaction between the atmosphere, topography and vegetation on regional and local scales (Clark et al., 2011). The snow distribution is especially non-uniform in Arctic and alpine environments, where the low vegetation is unable to inhibit wind drift of snow. This spatial variability of snow depths impacts the local distribution of wintertime ground surface temperatures (GST), with areas having greater snow depths being warmer, as they are better insulated from cold air temperatures (Zhang, 2005). These local patterns of snow depths gives rise to large small-scale variations in mean annual GST (MAGST), vegetation cover, and AL thickness' in permafrost areas. To capture the impact of local snow distribution, it is essential to represent the physical processes generating it at the relevant spatial and temporal scale.

The ability of a model to simulate the small-scale variability of snow cover is subject to a scaling issue, namely whether the model scale resolves the scale of the relevant processes (Blöschl, 1999). Currently, the grids of weather and climate models are typically around a few km, which is sufficient to resolve the main gradients of the SEB across the terrain. However, they do not capture the variations in topography and vegetation that give rise to local snow distribution (Clark et al., 2011). Different attempts have been made to overcome this scale gap, including statistical approaches (e.g. Gisnås et al., 2014) and tiling approaches (e.g. Aas et al., 2017; Nitzbon et al., 2019). While these schemes are able to reproduce an observed snow distribution, they overlook the physical processes producing the distribution. Consequently, there are still limitations in the ability to simulate spatially variable snow depth evolution.

1.2 Aims and objectives

The overarching aim of this MSc thesis is to enhance our ability to capture small-scale variability of snow cover in a land surface model (LSM). The effort is on including relevant physical processes in the detail and scale required to reproduce the range of local snow distribution, while limiting the added computational expense. To achieve this, available parameterizations of snow microstructure (CROCUS; Vionnet et al.,2012) are implemented in a parallelized permafrost modelling framework (CryoGrid; Nitzbon et al., 2019; Westermann et al., 2016). The thesis will have a regional focus on the Norwegian Arctic, empathizing on reproducing the lateral effects at play in a high Arctic and maritime climate. Ultimately, the goal is to present a tool that is applicable for exploring other snow related topics in adjacent scientific disciplines.

Based on the aforementioned, the research objectives of this thesis are:

1. To implement snow microphysics as detailed in CROCUS within the CryoGrid modelling framework.
2. To include process-based redistribution of snow through wind drifting and lateral percolation of water in a parallelized version of CryoGrid.
3. To realistically reproduce observed local variability of ground surface temperatures and snow pack evolution.
4. To explore the capabilities of the numerical setup for sites in the Norwegian Arctic, and outline potential applications within climate change research, permafrost sciences, hydrology and ecology.

2 Background

The theoretical background for this thesis is divided into an overview of snow and its most relevant properties (Sect. 2.1), general theory about LSMs (Sect. 2.2), and a short introduction to parallel computing (Sect. 2.3). Section 2.1 includes a presentation of snow properties and how they impact the terrestrial SEB, and a presentation of processes that redistribute snow and water. Section 2.2 features general theory of LSMs, their representation of snow, and how sub-grid variability can be tackled by tiling schemes. Section 2.3 provides a brief overview of the aspects of parallel computing that are relevant for this study, including their syntax in Matlab.

2.1 Snow

Snow consists of ice crystals, which form in the atmosphere, precipitate and accumulate on the ground where they undergo metamorphosis, before melting or sublimating away. On a seasonal basis, snow covers around 45x10^6 km^2 (January) to 2x10^6 km^2 (August) of the Northern Hemispheres land area (Lemke et al., 2007), making snow the largest element of the cryosphere. Snow exhibits reflective, moisture retaining and insulating properties that strongly modulate of the terrestrial energy and water balance, and have profound impacts on the climatic, hydrological and ecological systems where it is present.

Fresh snow has a high albedo, reflecting between 80 and 90 % of the incoming solar radiation (Lemke et al., 2007). As the snow ages and metamorphoses, its albedo is somewhat lowered due to accumulation of light absorbing impurities and transition to more compacted and spherical grains (Kump et al., 2009). However, any significant snowfall event will elevate the surface albedo again, and the strongest decrease in snow albedo is typically found during spring melt, when the snow is wet and subsequent old snow layers are exposed. Nevertheless, the snow albedo is typically much higher than the underlying ground surface, having a strong impact on the SEB when present (Kump et al., 2009). The high reflectivity of snow gives rise to the snow-albedo feedback, where an increase (decrease) in snow extent and/or duration will elevate (lower) the fraction of reflected solar radiation, resulting in a negative (positive) impact on the SEB and a decrease (increase) in surface and air temperatures.

Apart from reflecting energy that would otherwise be absorbed, the presence of snow also modulates the thermal regime through latent effects. When the snow temperatures are increased to the melting point, additional incoming energy is taken up by the process of converting snow to water, giving a period of temperatures around the melting point (Zhang, 2005). This is because of the high latent heat of fusion of water (~335 kJ/kg) and the upward bound of snow temperatures to 0°C.

This prolonged period of stable temperatures is known as the zero-curtain-effect, an effect that also can be observed during the freezing of water-rich soils.

The crystalline structure of snow gives a matrix consisting of a larger fraction of air than ice, which gives it a low thermal conductivity, while also inhibiting effective mixing of the entrained air (Kump et al., 2009). These properties make snow an excellent insulator able to maintain large temperature gradients, with snow depths of ~1m effectively decoupling the ground from the atmosphere (Hachem et al., 2012). This frequently manifests itself through substantially higher temperatures at the ground surface than in the above lying air, known as the nival offset (Smith & Riseborough, 2002; Trofaier et al., 2017). The offset between mean annual air temperatures and MAGST is called the surface offset, and includes the effect of vegetation as well as the nival offset.

The snowpacks large porosity and layered structure governs the infiltration and movement of liquid water within it. When water enters the snowpack through melt or rain-on-snow (ROS) events, parts of it is retained within the snow matrix. The volumetric fraction of water which the snowpack can hold against the pull of gravity is known as the field capacity (θ). The exact value of θ is variable and depends heavily on snow structure and density, but a frequently used estimate is that the field capacity comprises 5 % of the available pore space (Pahaut, 1976). Water exceeding this will infiltrate and flows further through the snowpack. The movement of water through snow is generally inhomogeneous (Colbeck, 1979), being subject to the snowpacks layered structure and associated variations in permeability. This leads to the formation of ice layers and preferential flow paths within the snowpack, and one-dimensional theories of water percolation can only be applied over a sufficiently large area average (Colbeck, 1972). If the soil below the snowpack is frozen, infiltration can be inhibited (Dingman, 2015), and in topographic settings where water accumulates this can lead to water stored at the base of the snowpack, slowly refreezing and creating a layer of basal ice. These effects give rise to large variability in snow density, and hydrologists thus often quantify the snow pack not by its depth, but rather by the water column it represents, the snow water equivalent (SWE). For the case that a layer of basal ice is present within the snowpack, the SWE can be calculated as:

$$SWE = \frac{d_{snow} * \bar{\rho}_{snow} + d_{ice} * \rho_{ice}}{\rho_{water}}$$

(Eq. 1)

where d_{snow} and d_{ice} denote measured snow and ice thickness, and $\bar{\rho}_{snow}$ is the measured bulk snow density. ρ_{water} is the density of water and ρ_{ice} is the density of pure ice, 1000 and 917 kg/m^3, respectively.

Most research on the movement of water within the snow has focused on the vertical dimension (e.g. Colbeck, 1972), while no knowledge basis is established for lateral percolation. However, automated snow monitoring near Ny-Ålesund, Svalbard (Westermann et al., 2015) shows how water within the snow cover accumulates in the same areas where surface runoff flows in summer (Figure 1), indicating that liquid water within the snowpack generally flows according to the hydraulic potential of the ground surface.

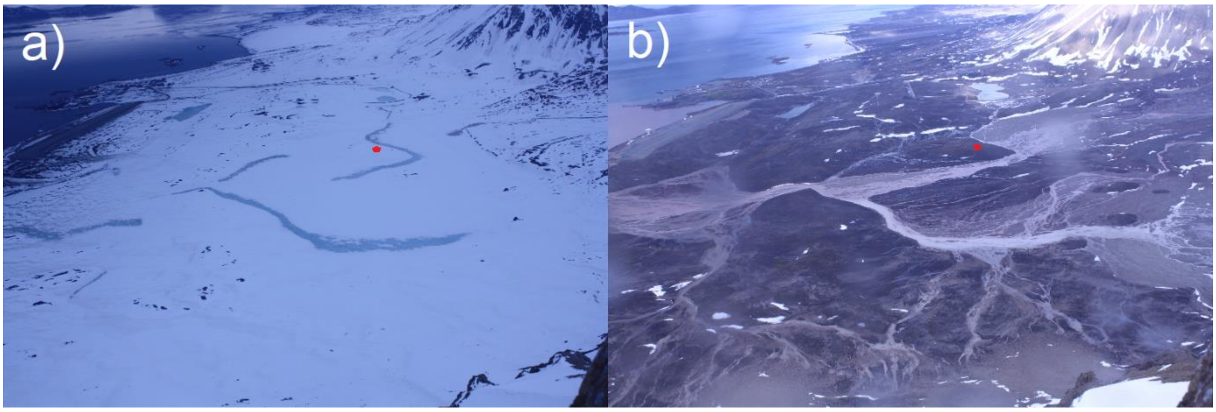

Figure 1: Image depicting surface conditions in the Bayelva area at the onset of spring melt on the 3.6.2013 (a), and early summer on the 30.6.2013 (b). The red dot indicates the approximate location of the Bayelva high Arctic Permafrost research site (Sect. 3.1.4).

The wind can rework the snow surface into various distinct bedforms (Kochanski et al., 2019), but the net effect of wind induced snow redistribution is a smoothing of the landscape (Mott et al., 2010). Aeolian snow transport occurs through three different modes: creep, saltation and turbulent suspension (Tabler, 1994). Snow transport within all these modes is denoted *drifting snow*, and the efficiency depends on the prevailing wind and its interplay with topography. Areas which are exposed experience snow erosion during drift events, whereas lee sides and topographical depressions are net receivers of drifting snow (Tabler, 1994). Landscapes subject to snow redistribution display distinct areas of snow accumulation and erosion, which is visible through the large variation in local melt out dates (Figure 2).

Figure 2: The spatial variability of the snow cover is visible during spring melt in the Bayelva Catchment, Svalbard. Image taken on the 20.6.2013, from Westermann et al. (2015).

2.2 Land surface models

Land surface models are numerical schemes aimed towards simulating the exchange of energy and matter (water, carbon, etc.) along the interface between the Earth's surface and atmosphere. The initial LSMs were used to prescribe the lower boundary of climate models in an oversimplified way (Pitman, 2003), but have since evolved substantially and are used both in general circulation models (GCMs) and in standalone configuration. LSM are now used to study the dynamics of Earths hydrological, energy and biogeochemical cycle, especially under changing climatic conditions.

The explicit representation of snow cover within LSMs is required due to its strong modulation of terrestrial fluxes, its spatial extent, and its transient nature. Armstrong & Brun (2008) classify snow schemes into three categories: Single-layer schemes, Intermediate complexity schemes, and detailed snow schemes. Single-layer schemes represent the snow as a soil layer with specific reflective and thermal properties, and are typically used in numerical weather prediction (NWP) and GCMs. These schemes are computationally inexpensive, but are limited to resolving the first-order processes induced by the snow cover. Snow schemes of intermediate complexity are used in applications requiring representation of some internal processes. Typically, they feature a prescribed number of vertical layers, and resolve processes such as water percolation, compaction and refreezing. Detailed snow schemes provide the most comprehensive description of snow properties and processes. They account explicitly for the dynamic buildup of the snowpacks layered structure, and the vertical and temporal evolution of snow microstructure. Detailed snow schemes are computationally expensive, and are seldom run within NWP models or GCMs (Brun et al., 1997).

Many physical processes occur at horizontal scales not captured by LSMs, including the local redistribution of snow (Aas et al., 2017). This scaling gap between land surface processes and the grid of GCMs or NWP schemes, can be addressed through a further division of the grid into *tiles* (Koster & Suarez, 1992). Each tile can be assigned a set of properties, and thus represent a distinct element of the sub-grid distribution. Individual tiles can represent different surface covers or elevation bands (Zhao & Li, 2015), or distinct landscape units (Nitzbon et al., 2019). Attempts have been made to capture the sub-grid variability of melt out dates and ground thermal regime at barren sites using a tiling approach, scaling the snowfall for the individual tiles according to an observed coefficient of variance (Aas et al., 2017). While most tiling approaches divide the landscape into a mosaic of 1D realizations to represent spatial heterogeneity, recent approaches calculate fluxes among tiles, e.g. (Nitzbon et al., 2019).

2.3 Parallel computing

Parallel computing entails distribution of computational tasks among available processors/cores, and is currently the dominant paradigm in computer architecture (Asanovic et al., 2006). Tiled representation in LSM is in line with the increasing standardization of multi-core processors, as individual tiles can be simulated on their own cores. The implementation of several, parallel 1D realizations is straight forward in such a computing environment, while the exchange of information among tiles requires dedicated protocols. Using the message passing interface (MPI) communication protocol, cores can communicate directly or commonly with each other.

Matlab by MathWorks features a “Parallel Computing Toolbox”, which amongst other allows for distribution of work to different cores, and communication amongst them. The user can create a “parallel pool” consisting of a defined number of *workers*, which are available for parallel computation. Using the *spmd* (single program, multiple data) functionality, the execution of a segment of code is distributed among the workers. By assigning a worker to each simulated tile, the tiles can be integrated forward in time simultaneously. At certain locations within the code, it is necessary to exchange information among the tiles. MatLab allows for data transfer between workers by the commands *labSend* and *labRecieve*. LabSend sends data to one or several other workers, and labRecieve will halt the current worker until the corresponding information is received from the other workers.

3 Methods and data

3.1 Study area

3.1.1 Geography

The area of study for this thesis is Svalbard, an archipelago located in the European Arctic between 74-81°N and 10-30°E (Figure 3). It lies ca. 650 km north of mainland Norway, while Greenland and Franz Josef Land (Russia) neighbor the islands to the west and east, respectively. More than 60 % of the archipelagos land area is covered by glaciers, while low vegetation covers 6-7 % (Thuesen & Barr, 2020). The rest is ice and vegetation free, constituting the polar barrens that are typical for the high Arctic (Klein, 2016). These latitudes are subject to large differences in insolation, and areas as far south as 74°N experience polar darkness and midnight sun for more than half the year.

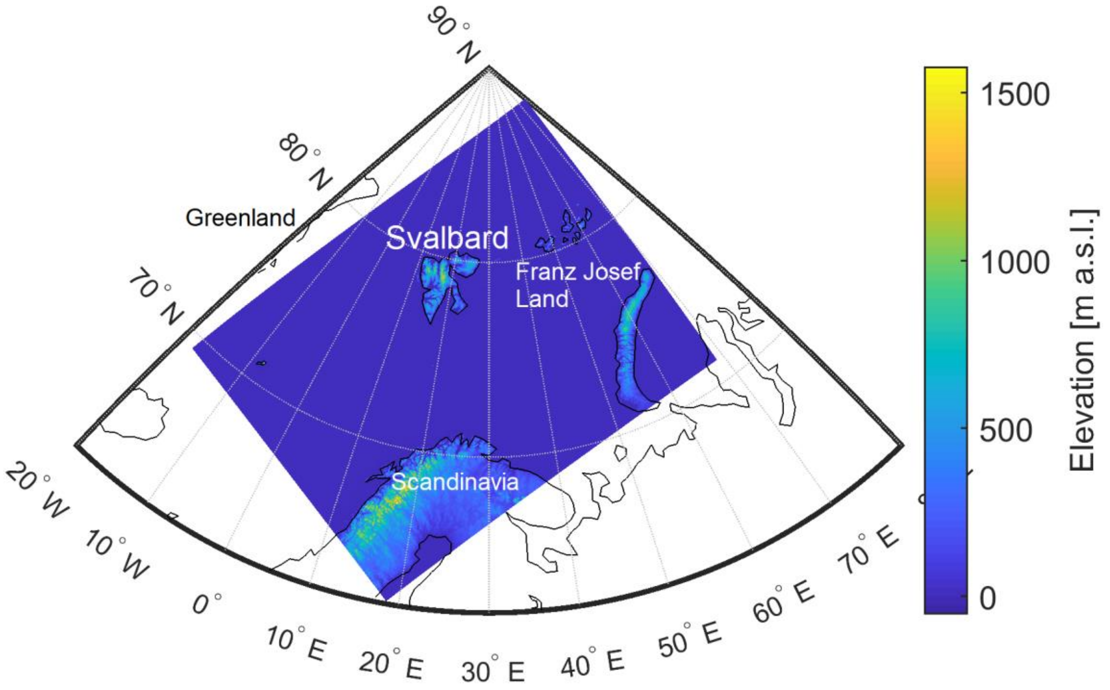

Figure 3: The location of the Svalbard archipelago within the North Atlantic. The colored area shows the extent of the AROME-Arctic model (sect. 3.2.2), with the shading indicating the surface elevation used in the model.

3.1.2 Climate

Climate in Svalbard 2100 (Hanssen-Bauer et al., 2019) provides a comprehensive compilation of the established knowledge on the state of, and the processes governing, current and future climate in Svalbard. In general, the climate is characterized by little precipitation and year round low temperatures, falling in the classification *Tundra Climate* in the Köppen climate classification scheme (Thuesen & Barr, 2020). The region is considerably warmer and wetter than the average for the latitudes, which is attributed to atmospheric heat and moisture transport. The region is situated at the end of the Atlantic cyclone track (Humlum, 2002), and experiences frequent cyclone activity in winter and fall. This has associated effects on wintertime temperatures, which exhibit large variability. In addition, the West Spitsbergen current, a branch of the North Atlantic Current, flows West of Spitsbergen, and modulates the climate through its release of heat.

The bulk of meteorological and climatological observations in Svalbard are recorded at low elevations along the West coast of Spitsbergen (Hanssen-Bauer et al., 2019). For the standard reference period for long-term climate change assessments, 1961 – 1990, annual air temperatures for Svalbard were well below zero, with positive seasonal values only for the summer months (JJA). Annual precipitation during the same period was between 200-500 mm, with lower values in central parts (e.g. Svalbard Airport; 189 mm) than at the west coast (e.g. Ny-Ålesund; 385 mm) (Hanssen-Bauer et al., 2019).

The snow climate of central Svalbard was classified as *high Arctic maritime* by Eckerstorfer & Christiansen (2011). They define this class by having a thin, cold snowpack typically present for 8-10 months at low elevations, and perennial snow cover at higher elevations. The snowpack is characterized by a slow onset and reworking by local meteorological conditions, having a frequent presence of ice layers and wind slabs, and being underlain by depth hoar. While many of the traits likely are valid for the snowpack across Svalbard, the higher precipitation at coastal sites will produce a somewhat different snow climate here compared to the study region of Eckerstorfer & Christiansen (2011).

Svalbard, as well as the whole Arctic, is currently experiencing pronounced climate change. Hanssen-Bauer et al. (2019) reports statistical significant warming of both modelled and observed air temperatures over the period 1971 – 2017. On average, Svalbard has experienced warming of 0.87°C/decade, with winter temperatures experiencing the strongest increase. The warming is largely attributed to the decrease in sea ice in the surrounding waters, especially to the North and in the Barents Sea (Isaksen et al., 2016). The decrease of fjord-ice in Spitsbergen can also give local temperature increases in winter (Hanssen-Bauer et al., 2019). In addition, a positive trend in wintertime cyclone activity is identified around Svalbard (Wickström et al., 2020).

Observed annual precipitation is reported to increase in recent years, while models show a small decrease (Førland et al., 2011, 2020). It is debated whether the increase is actual, or if it is an artefact of the temperature increase (Førland et al., 2020). Under warmer conditions a larger fraction of the precipitation falls as rain, a state in which under-catch at precipitation gauges is smaller. Future climate change on Svalbard is subject to how humankind manages its emission, but under all representative concentration pathways, Svalbard is projected to warm 2-3 times the global average (Hanssen-Bauer et al., 2019).

3.1.3 Permafrost history

Permafrost is widespread in Svalbard, displaying numerous permafrost landforms such as rock glaciers, ice-wedge polygons and pingos (Liestøl, 1975). The age of the permafrost is variable across the archipelago, being a product of the regions Quaternary history. Climatic conditions during this period were substantially cooler than present, yet variable, facilitating the buildup and collapse of several glaciations. During the most recent glaciation the ice reached the pressure melting point in the large valleys on Spitsbergen, leading to permafrost degradation in these areas. Isostatic rebound has also exposed new land to the atmosphere, resulting in recent permafrost aggregation in these areas. Observations (Humlum, 2005) and modelling approaches (Hornum et al., 2020) suggest permafrost thicknesses of 100-150 m in these low laying areas, while higher areas that were ice-free (Nunataqs) or covered by cold-based ice might be underlain by 4-500 m of permafrost.

A comprehensive overview of permafrost research in Svalbard is provided by Humlum et al. (2003). The presence of permafrost has been known since the *First International Polar Year* in 1882, and most of the 20th century it was studied primarily by geomorphological means and through data from existing mines. Dedicated permafrost monitoring commenced towards the end of that century, e.g. the Bayelva high Arctic permafrost research site (Boike et al., 2018), and the >100 m deep permafrost borehole in Janssonhaugen (Isaksen et al., 2000). At present, permafrost is monitored at specific locations in Svalbard through boreholes and selected landforms (Christiansen et al., 2016). Recent advances also facilitate spatial distributed permafrost modelling utilizing available remote (satellite) sensed products (e.g. Obu et al., 2019).

3.1.4 Study sites

The area surrounding the Bayelva high Arctic permafrost research site is the geographical focus of the study. Other areas from the Norwegian Arctic are included to explore the capacities of the presented model approach in other geographic and topographic settings.

Bayelva area

The Bayelva high Arctic permafrost research site comprises a unique record of atmosphere, snow and soil data in the Svalbard archipelago, spanning back to 1998. The site is situated on a small hill in the immediate vicinity of the Ny-Ålesund research settlement, and is described in detail in Boike et al. (2018), see Figure 4. The record consists of time series from automated loggers, snow- and soil profiles, vegetation and soil surface surveys, and aerial scans. The area around the site mostly consists of a floodplain interrupted by low ridges, and is bordered by the Bayelva river to the south and east. The terrain profiles in Figure 5 show the relief of the area and the typical ridge-depression-plain configuration, which is the basis for the lateral setup (Sect. 3.4.1).

Since 2012, this site is accompanied by a research campaign aiming to capture the spatial variability of snow and thermal regime around this location. Gisnås et al. (2014) details the original setup, which without mayor modification has been continued until present. The effort includes observations at >100 geospatially distributed locations around the Bayelva site (Figure 4a), providing a statistically sound dataset for further investigation. Due to the small spatial dimensions, the meteorological conditions can be assumed to be homogenous within the area covering these locations, which is referred to as the *Bayelva area* throughout this thesis. At each location, a small iButton temperature sensor (Maxim Integrated; precision 0.0625°C, accuracy ca. 0.2°C) is deployed immediately below the soil surface, logging GSTs every 4 hours throughout the year. The loggers are read out, and missing or broken loggers are exchanged, in the end of each summer, corresponding well with the end of the hydrological year, August 31st. Over the years, a few locations have had to be discontinued due to fluvial erosion or excess wetness. The GST time series are accompanied by a yearly snow survey around the time of peak snow accumulation, between mid-April and mid-May. The survey consist of measurements of snow depth and basal ice thickness at each logger location, and bulk snow density measurements for the whole area. Based on the transient record of GSTs and the snow soundings, Gisnås et al. (2014) showed how the thermal regime is highly variable and dependent on local snow depths in the Bayelva area.

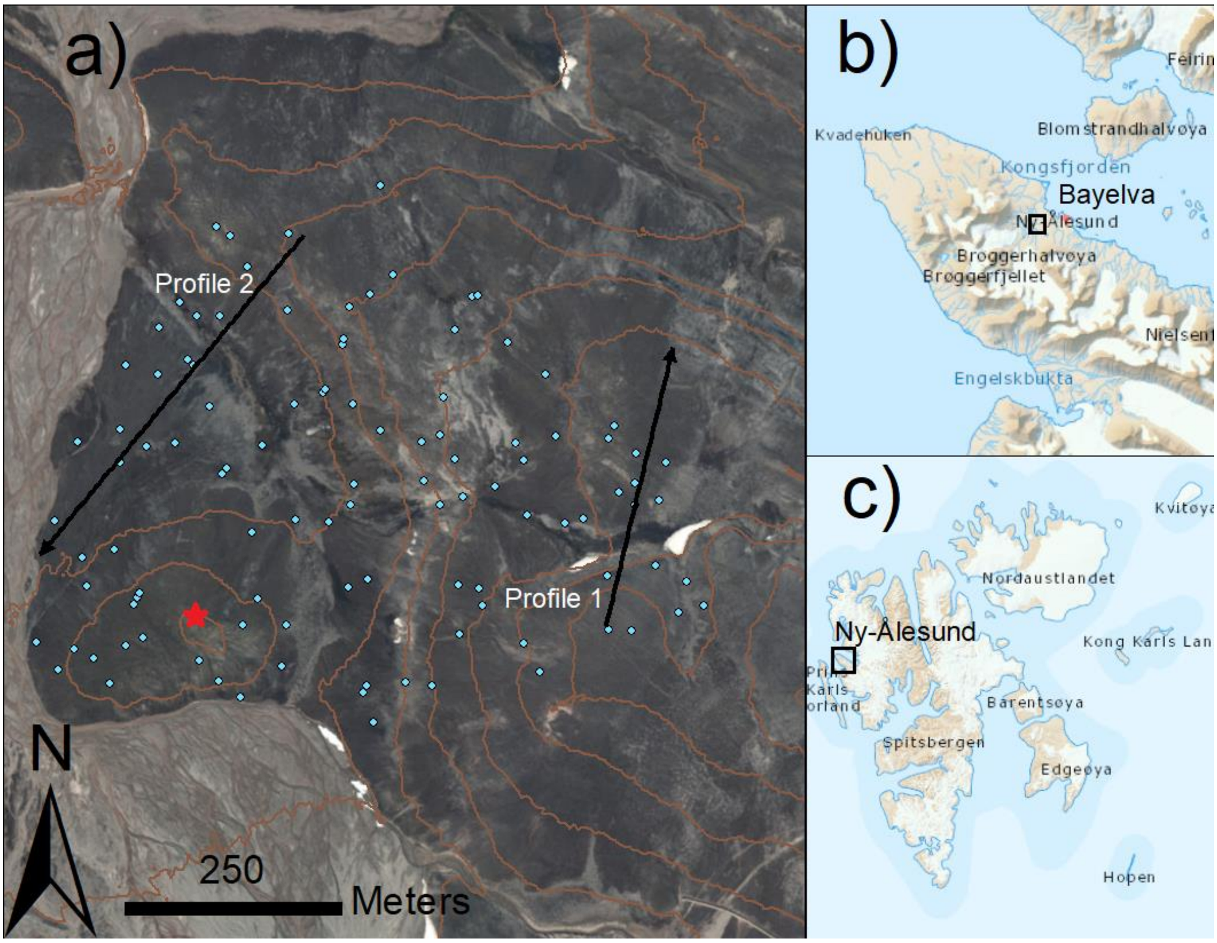

Figure 4: (a) Orthophoto of the Bayelva area; (b) its location on the Brøgger peninsula, and (c) within the Svalbard archipelago. The red star indicates the location of the Bayelva high Arctic permafrost research site. Blue dots show the location of the ground temperature measurements used in this study, while Profile 1 and Profile 2 refer to the terrain profiles presented in Figure 5. The contour lines in (a) have an equidistance of 5 m, maps and orthophoto are courtesy of the Norwegian Polar Institute (www.npolar.no).

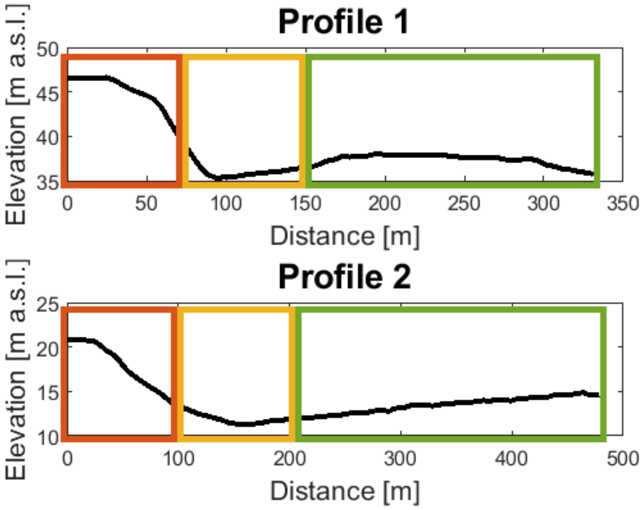

Figure 5: Terrain profiles 1 and 2 (see Figure 4) with the landscape units defined in Section 3.4.1: Red – Ridge; Yellow – Snowbed; Green – Ambient.

Nordenskiöld land

This thesis also includes a study area on Nordenskiöld land on Spitsbergen (Figure 6a). Since 2010, ground surface conditions have been recorded at a number of locations in the area, as a part of an effort by the Norwegian University of Life Sciences (NMBU) to monitor environmental variables which can impact the behavioral dynamics of the regions only large herbivore, the Svalbard reindeer (Loe, Hansen, Stien, Albon, et al., 2016). GSTs are recorded at a total of 144 locations in the area, following a hierarchical block design (see Peeters et al., 2019). The study area is divided into eight geographical subareas, within which measurements are done at “ridge” and “sub-ridge” exposures at an upper and lower elevation. Each of these “topographical settings” (subarea; elevation; exposure) is replicated at four locations within horizontal dimensions of 600 m. At each location, the GST is recorded using an iButton logger, which is placed on the ground surface. Note that the loggers in the Bayelva area and in Nordenskiöld land feature different precisions, being respectively 0.0625°C and 0.5°C.

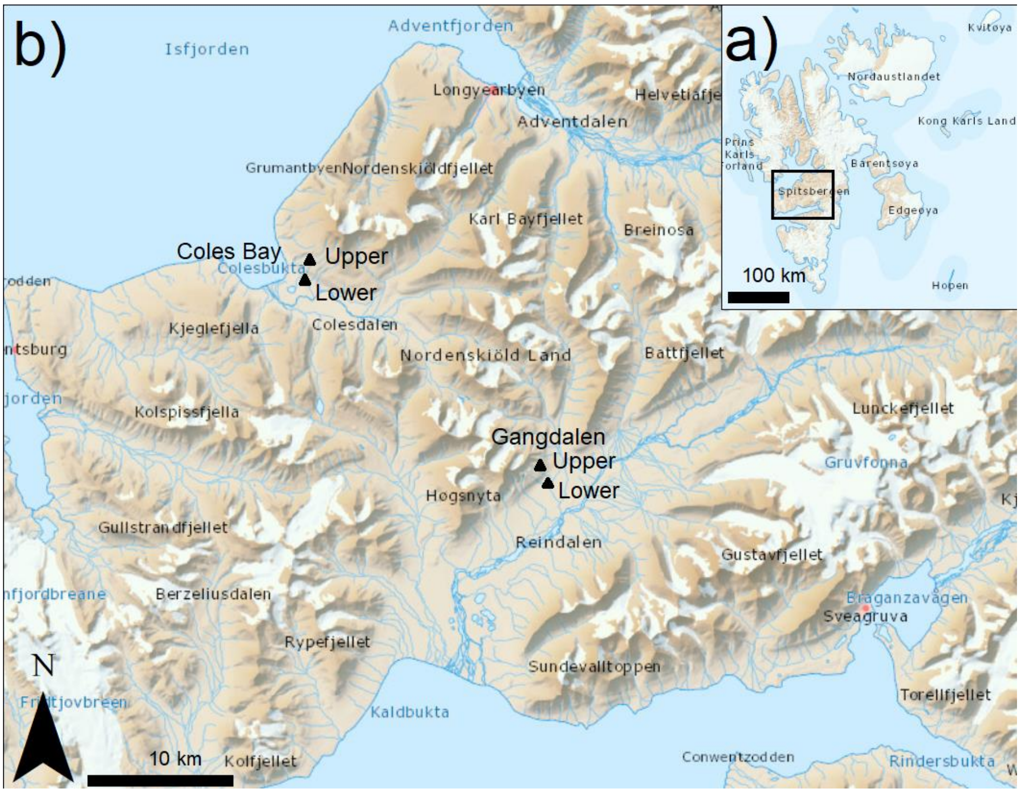

Figure 6: The location of Nordenskiöld land within Svalbard (a), and the location of the “topographical settings” included from in this area (b). Map data courtesy of the Norwegian polar institute (npolar.no).

For this thesis, only data from the most coastal and most inland subarea are used (Table 1 and Figure 6b). The data on the geographical position, exposure and GSTs for the individual sites are provided by Prof. L. E. Loe (NMBU), while the elevation is extracted from a terrain model (5m DEM; npolar.no). The rationale behind including this study area is to compare simulated and observe GST from sites spanning significant differences in elevations and distances. Contrary to the Bayelva study area, meteorological conditions cannot be assumed to be negligible within the dimensions of the Nordenskiöld land study area.

Subarea	Elevation	Exposure	No. loggers
Coles Bay	Upper	Ridge	4
	226 - 251 m a.s.l.	Sub-ridge	4
	Lower	Ridge	4
	45 - 64 m a.s.l.	Sub-ridge	4
Gangdalen	Upper	Ridge	4
	196 - 214 m a.s.l.	Sub-ridge	4
	Lower	Ridge	4
	62 - 87 m a.s.l.	Sub-ridge	4

Table 1: The topographical parameters defining measurement locations in the Nordenskiöld land study area.

Garwoodtoppen

Another landform for which lateral transport of snow likely plays a key role are nunataqs, which are frequent in the ice fields of Svalbard. A nunataq is an exposed peak or ridge that is surrounded by glacier ice, but is not itself covered in perennial snow or ice. To investigate if this can be reproduced within the CryoGrid model, the nunataq Garwoodtoppen is chosen as a study site. Garwoodtoppen is a rocky mountain surrounded by the glaciers Kronebreen to the north and Kongsvegen to the south (Figure 7). Garwoodtoppen is located approximately 20 km southeast of Ny-Ålesund, and can be seen from the research settlement. Its main peak measures 757 m a.s.l., with two minor peaks reaching 646 and 628 m a.s.l. These are all above the equilibrium line altitude (ELA) in the area (the altitude above which glaciers experience net accumulation), which observations show to be between 400 and 500 m a.s.l. (Hagen et al., 2003).

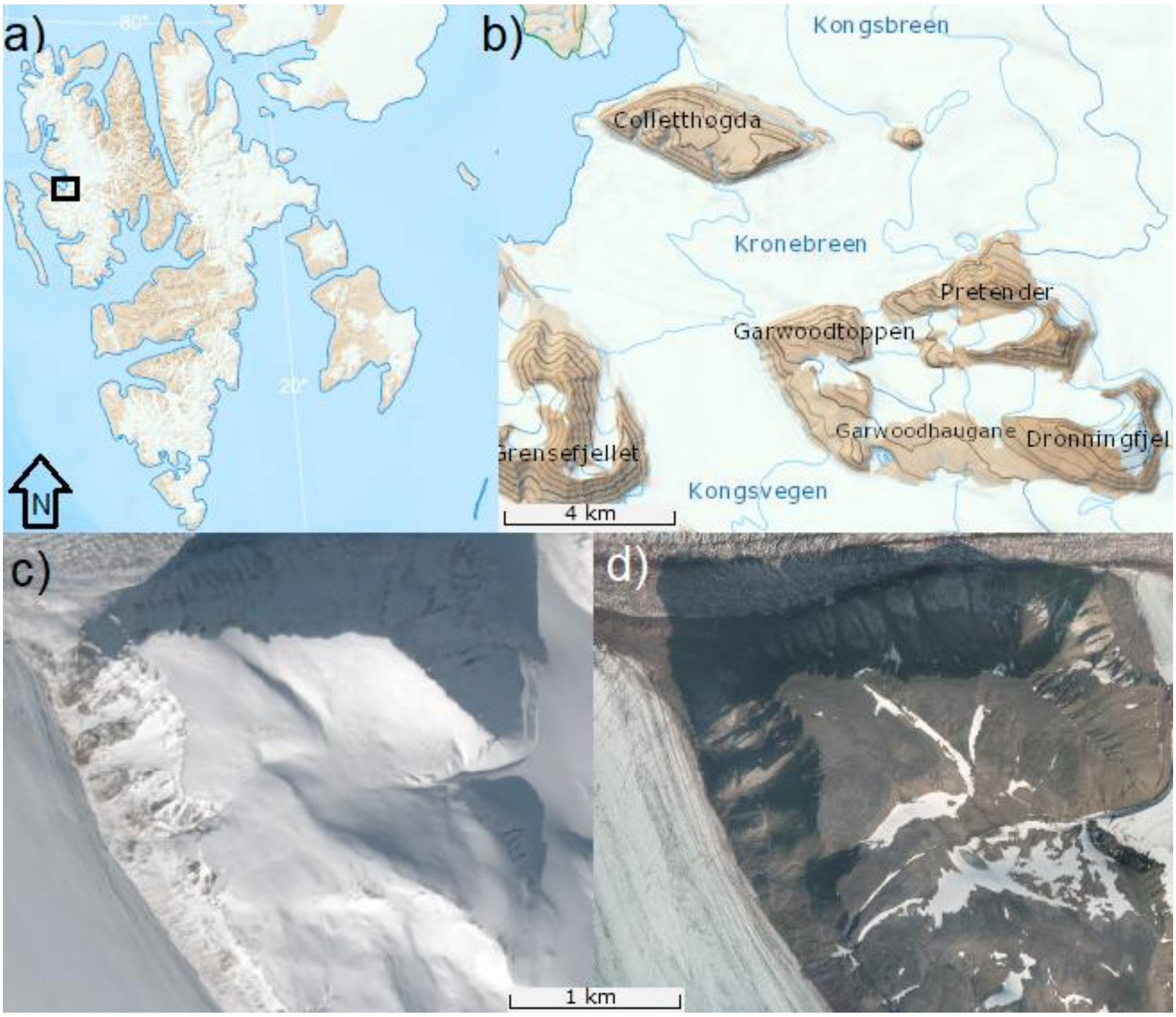

Figure 7: (a) Location of Garwoodtoppen within the Svalbard archipelago. (b) Topographic map showing Garwoodtoppen and the surrounding glaciers. (c) Sattelite image showing conditions in winter, and (d) Aerial photograph depicting summer conditions. All data courtesy of the Norwegian Polar Institute (npolar.no).

Suossjavri (Finnmark)

Palsas are permafrost landforms consisting of mounds of peat rising above the surrounding landscape, containing segregated perennial ice layers (Martin et al., 2019). The sustenance of this landform relies on snow and water being removed, so that the palsa experiences thin snow depths in winter, and dries in summer. In Norway, palsas can be found in mires in the sporadic permafrost zone, and a their extent has decreased substantially over the last half century (Borge et al., 2017). Tiling approaches have previously been used to successfully represent this landform in ESMs (Aas et al., 2019), while here it is explored whether the same setup can be transferred to the CryoGrid framework. The site selected for the palsa study is Suossjavri (ca. 335 m a.s.l.) in Northern Norway (Figure 8), where palsas elevated up to 2 m above the surrounding mire are found.

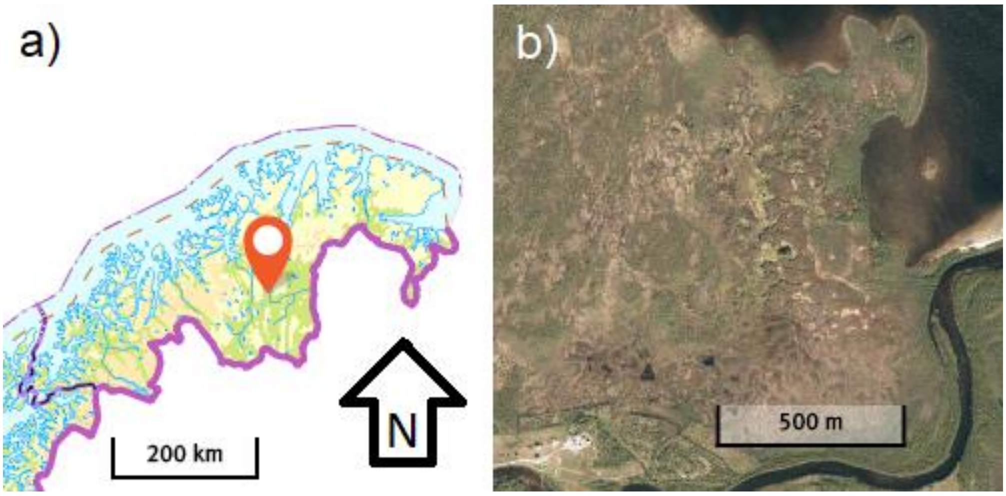

Figure 8: (a) The location of the Suossjavri study site within Troms and Finnmark County. (b) Aerial photograph of the palsa mire in Suossjavri. Map and orthophoto courtesy of the Norwegian mapping authority.

3.2 Data

3.2.1 Field observations

For this thesis, it was of paramount importance to obtain a sound dataset describing the spatial and temporal variation of snow cover and GSTs. A comprehensive survey of the snow and ice cover on the Brøgger peninsula around the time of peak snow accumulation thus constitutes the main field activity of the thesis. Over the period 23.04.19 - 02.05.19, snow surveys were conducted at different sites around Ny-Ålesund. To secure multiple years of data the effort was concentrated on continuation of established surveys of relevant snow properties. Thus, a special focus was on the previously described geospatial arrays of snow and temperature measurements around the Bayelva area.

Observations of snow properties were made following a predefined protocol. Snow depths were initially measured using a snow probe, and for sites with snow depths below 50-60 cm, a small hole was dug to assess ground conditions. If basal ice was present, this was measured using a 21cm long ice screw. Ice thicknesses exceeding this were recorded as “>21cm”, but are assigned the value 21cm in the SWE calculation (Eq. 1). After the initial survey, a number of locations for more detailed snow profiles were selected, representing the observed distribution of snow depths (Figure 9). The snow properties recorded for each profile include the thickness, grain type, grain size and hardness for all layers, as well as temperature every 10 cm and bulk density.

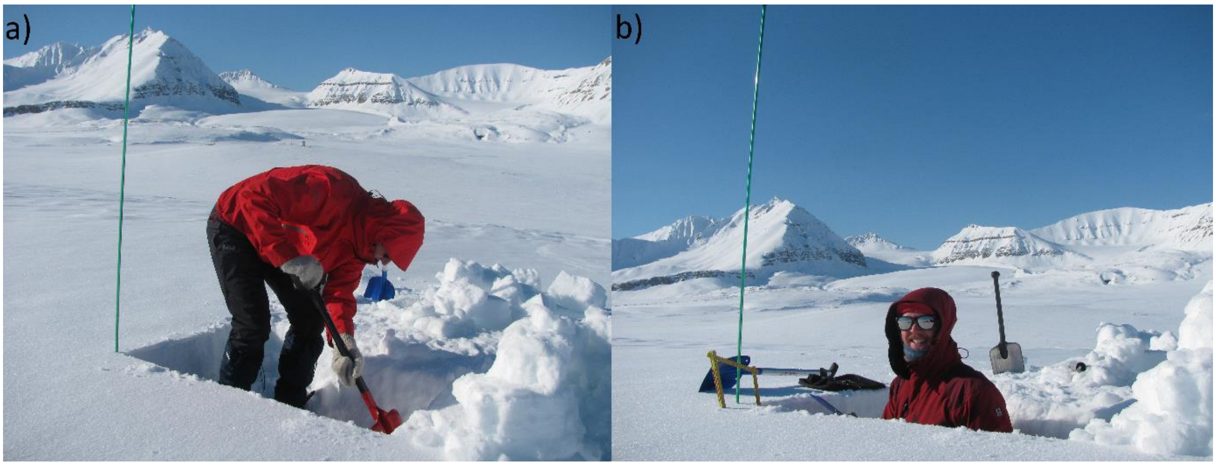

Figure 9: (a) Establishing a snowpit in the Bayelva area, and (b) observation of snow properties.

Snow surveys were done at several locations spanning the Brøgger peninsula, but only data from the Bayelva area is used in this thesis, as these snow surveys complement year-round GST measurements. Snow depths were recorded at all 109 points in the measurement array, even those where the GST measurement is discontinued. At a total of 88 of these locations the Basal ice thickness was measured, and 10 detailed snow profiles were obtained. Table 2 summarizes the observations from the field effort at the Bayelva area. Collectively, these observations comprise a basis for estimating the spatial distribution of snow depth and SWE in the Bayelva area.

	Unit	Observation
Mean snow density	kg/m^3	429
Mean snow depth	cm	33
Mean ice thickness	cm	13,5
Points with >21cm ice	No.	16

Table 2: Main findings of the snow survey at the Bayelva area in spring 2019.

The GST loggers around the Bayelva area were read out during another research stay in Ny-Ålesund 29.08.19 - 5.09.19. The iButton loggers were dug out, removed from their casing, and the data was downloaded onto a field computer. After readout, the loggers were put in a new waterproof casing and returned to their location ~2-3 cm below the surface. Malfunctioning loggers were replaced. Data from total of 95 loggers was extracted, while 5 were replaced. In total 6 sites were eroded or in other way made inaccessible by water processes.

3.2.2 Forcing data

About AROME-Arctic

The data used as forcing throughout this thesis originates from the AROME-Arctic NWP model. This model was chosen as it provides high-resolution (2.5 km) fields of meteorological variables for the European Arctic (See Figure 3), covering all of the study sites. The Norwegian Meteorological Institute (MET Norway) has had AROME-Arctic in operational use since November 2015, issuing forecasts with 66 hours lead-time four times a day. NWP in this regions is challenging due to scares observations, complex processes at the sea ice edge, and accelerated changes in climate. However AROME-Arctic is especially tailored for the area, and provides a more accurate description of near-surface meteorological conditions than comparable models for the European Arctic (Køltzow et al., 2019; Müller et al., 2017).

Data extraction routine

Data for the variables required to force the CryoGrid model are downloaded for the period 2. November 2015 – 3. November 2019 from MET Norway' THREDDS server (https://thredds.met.no/thredds/catalog/aromearcticarchive/catalog.html). To identify the grid point best fitting the study area, the geopotential of the lowest vertical level in AROME-Arctic (representing the surface) and the elevation of each study area are compared. As the surface elevations in AROME-Arctic are the average over ca. 2.5*2.5 km, using data from the closest grid point might give biased forcing data due to elevation differences, especially in areas with high relief. E.g. for the Bayelva area, the closest grid point had an altitude of 129 m a.s.l., so instead data from the neighboring point to the east (21 m a.s.l.) was used, as this is closer to the altitudes reported for this site (10 - 50 m a.s.l.; Gisnås et al., 2014).

Time series of data are only extracted for one selected grid point for each study area. Since AROME-Arctic is an operational product, gaps and errors in the time series occur and are not corrected. To ensure a continuous time series, a routine using forecasts issued at different times is used to bridge these gaps. For each date, if available, the forecast issued 06UTZ the day before is downloaded. If it is not, the latest preceding forecasts spanning the current date is download. This yields a continuous forcing data set consisting mostly of forecasts with 18 hours lead time. The extraction of data was done by further developing a Matlab script provided by T. V. Schuler (department of Geosciences, UiO).

Processing of forcing data

The data available from AROME-Arctic has to be processed to fit with the required format for CryoGrid. Table 3 summarize the variables and formats needed for CryoGrid, and the parameters in AROME-Arctic that are used to derive these.

CryoGrid	Unit	Available from AROME-Arctic	Unit(s)
Air temperature	°C	Air temperature	°C
Surface air pressure	Pa	Surface air pressure	Pa
Longwave incoming radiation	W/m^3	Accumulated incoming longwave radiation	W s/m^2
Shortwave incoming radiation	W/m^3	Accumulated incoming shortwave radiation	W s/m^2
Rainfall rate	mm/day	Accumulated precipitation; Accumulated snowfall	Kg/m^2
Snowfall rate	mm/day	Accumulated snowfall	Kg/m^2
Wind speed	m/s	Easterly wind; Northerly wind	m/s
Specific humidity	g/kg	Relative humidity; Surface air pressure; Air temperature	[-]; Pa; °C

Table 3: Forcing data required by the CryoGrid model, and the available data from AROME-Arctic

Air temperature and surface air pressure are the only variables that can be used directly. The wind speed (*U*) is derived from northerly wind (*u*) and easterly wind (*v*) by converting from Cartesian to polar coordinates:

$$U = \sqrt{u^2 + v^2}$$

(Eq. 2)

All the variables provided accumulatively by AROME-Arctic are converted to hourly rates by calculating their forward difference and dividing by 3600 [s/hr]. Precipitation and snowfall rates have to be converted from kg/s m^2 to mm/day by the following relationship:

$$^{mm}/_{day} = \frac{kg}{s * m^2} * \frac{1000\ ^{mm}/_{m}}{1000\ ^{kg}/_{m^3}} * (24 * 60 * 60)\ ^{s}/_{day}$$

(Eq. 3)

Rainfall rates are obtained by subtracting the snowfall rate from the total precipitation rate. Further, relative humidity, air temperature and surface air pressure are used to derive specific humidity. The saturation vapor pressure (e_s, in hPa) is approximated using the August–Roche–Magnus formula:

$$e_s = 6.1094 \exp\left(\frac{17.652 * T}{T + 243.04}\right)$$

(Eq. 4)

Where *T* is the air temperature in C. The actual vapor pressure (*e*) is then calculated using the relative humidity relationship:

$$e \; = e_s * RH$$

(Eq. 5)

Which is related to the water vapor mixing (*r*) ratio is calculated through the surface air pressure (*p*, in hPa):

$$r = \frac{0.622 * e}{p - e}$$

(Eq. 6)

From which the specific humidity of air (*q*, [-]) is calculated:

$$q = \frac{r}{1 + r}$$

(Eq. 7)

Further, unphysical (negative) values of rainfall, snowfall and incoming shortwave radiation are removed from the time series, and a lower threshold of 0.5m/s is set for the wind speed. Finally, 3-hour averages are calculated for each variable, providing a smoother forcing curve and allowing to bridge single erroneous values.

3.3 CryoGrid framework

The numerical fundament of this thesis is the CryoGrid model suite, which is a one-dimensional LSM designated to study permafrost processes. The physics of this model, parameterizing the SEB and subsurface heat transfer, are published in Westermann et al. (2016). It includes representation of processes of importance in many permafrost environments, most notably it allows for excess ice melt and associated ground subsidence. CryoGrid provides the users with a flexible platform for investigating the thermal regime of various landforms under changing climatic conditions, using the same forcing data as the LSMs. The model has been used in standalone (1D) configuration to simulate the formation of thermokarst lakes in Siberia (Westermann et al., 2016) and peat plateaus in Northern Norway (Martin et al., 2019). Recent modifications of CryoGrid include a parallelized version allowing for lateral soil water fluxes, which successfully has been used to investigate the dynamics of ice-wedge degradation in polygonal tundra (Nitzbon et al., 2019).

There currently exist several versions of CryoGrid, featuring capabilities relevant for specific landscapes, e.g. polygonal tundra (Nitzbon et al., 2019) and Arctic forest (Stünzi et al., 2019). To avoid confusion, “*CG Crocus*” is used to refer to the version presented in this thesis, which is structured in a modular setup, includes a detailed snow scheme (Sect. 3.4.2) and lateral exchange of snow and water (Sect. 3.4.3).

The physics of *CG Crocus* include available parameterizations to describe the land-atmosphere interaction and the thermal regime of the sub-surface. The surface energy balance follows Foken (2008), with latent and sensible heat fluxes as described by the Monin-Obukhov similarity theory (Monin & Obukhov, 1954). Fourier’s law detailing heat conduction for a given temperature, *T*, at a depth below the surface, *z*, gives the subsurface transfer of energy:

$$c_{eff}(z,T)\frac{\partial T}{\partial t}-\frac{\partial}{\partial z}\left(k(z,T)\frac{\partial T}{\partial z}\right)=0$$

(Eq. 8)

where $c_{eff}(z,T)$ denotes the effective volumetric heat transfer incorporating latent effects, and $k(z,T)$ is the thermal conductivity (Westermann et al., 2013). Water movement within the soil is handled according to the 1D-hydrology scheme presented in Nitzbon et al. (2019), with excess water being removed from the system (i.e. no formation of surface water). The lower boundary of the modelled domain is subject to a constant geothermal heat flux.

Recently, the code structure of CryoGrid was adapted to a modular setup, facilitating easier implementation of new parameterizations while keeping existing model physics the same. It is within this new structure that the model development part of this thesis is done, so an overview of its basics is provided in the following section.

3.3.1 Numerical structure

CryoGrid is scripted using the numerical computing environment Matlab by MathWorks. The code of the current version is provided on the source code host GitHub (https://github.com/CryoGrid/CryoGrid), where also development is published. For this thesis, a dedicated development branch to the master code, named *LATERAL_IA*, was used to manage the contributions. The contributions mainly constitute a more detailed snow scheme (section 3.4.2) and a scheme for lateral exchange between parallel realizations (section 3.4.3). Apart from this, also functionality to preprocess the data outputted was contributed.

The code structure of the current CryoGrid version is modular, based on object-oriented programming. The core of the code is a *main* file, which assembles the user defined stratigraphy and modular setup, and integrates the system through time. This script calls a number of *classes*, which provide the different functionalities to the numerical system. There are designated classes to provide the forcing data, describe the physics of soil and snow, prescribe interactions, and process output. The soil and snow classes handle internal processes, and are connected to each other by interaction classes conveying boundary fluxes to the bordering classes. The detail in which the physics are described within each class is arbitrary from a technical aspect, as long as they provide the necessary boundary fluxes. The next time step is set dynamically during each time step to assure numerical stability for all classes. The nature of this structure facilitates easy addition of new parameterizations.

To elaborate on how these classes interact an example of how a palsa mire can be described by three classes of varying complexity is provided. The mire can be simulated by a ground class that handles surface energy- and mass balance, heat conduction, water percolation and excess ice melt. For the bedrock below this, a ground class simulating only heat conduction can be attached with an interaction class prescribing a zero water flux boundary condition. Water will then pool up within the mire on top of the permafrost or the bedrock, whichever is higher. When snowfall occurs, a snow class is called and assembled on top of the mire with a designated interaction class. Before reaching a user defined threshold value of SWE, the snow is considered a *child* and its properties are only represented on a fraction of the ground surface. Several snow schemes with varying detail in their description of snow processes are available. This shows how the modular version of CryoGrid can be used to only represent the processes relevant for the system in question.

3.3.2 Snow scheme

As part of this thesis a new snow class is developed for CryoGrid, implementing parameterizations of snow microstructure from the detailed snow scheme CROCUS (Vionnet et al., 2012). CROCUS describes the physical processes governing the evolution of the snow cover at a specific location, with a special emphasis on processes relevant for avalanche formation. The new snow class is developed based on an existing CryoGrid snow class (referred to as "*simple snow scheme*"), and only parameterizations deemed relevant for permafrost applications are included from CROCUS. Table 4 provides an overview of the physical processes included in the new snow class, referred to as the *Crocus scheme*. To resolve several of the novel processes, a description of snow microstructure is required, which is achieved by introducing the parameters dendricity (unitless, range 0-1), d, sphericity (unitless, range 0-1), s, and grain size (mm), g_s.

Simple snow scheme	CROCUS
Heat conduction	Short-wave radiation transmission
Dynamic buildup	Transient albedo
Ablation due to melt	Transient density
Sublimation/deposition	Metamorphism
Water infiltration	Mechanical settling
Water refreezing	Wind compaction

Table 4: Process included in the new "Crocus scheme" that are continued from the "simple snow scheme" (left column) and where novel parameterizations from CROCUS (Vionnet et al., 2012) are introduced (right column).

Simple snow scheme

Here, a basic overview is provided of the functionality from the *simple snow scheme* that is continued in the *Crocus scheme*. A realistic build up and melt out of the snowpack is achieved by a dynamic upper boundary of the snowpack, with a SWE threshold controlling the addition and removal of snow layers. Whenever the uppermost snow layer exceeds 1.5 times the SWE threshold, it is split into two layers with identical properties, where the SWE of the lower is equal to the threshold value. The SWE of the uppermost layer can increase due to snowfall, rainfall and deposition, while melt and sublimation remove SWE. Internal snow layers can only experience increase in SWE due to refreezing of melt/rain water. In the case of rainfall, the energy associated with cooling the rainwater to 0°C is added to the uppermost snow cell. During ablation, a snow cell is merged with its lower neighbor when its SWE is lower than 0.5 times the threshold. For all applications in this thesis, a SWE threshold of 0.01 m is applied.

Heat conduction in snow is prescribed in a different way than for the soil domain (Eq. 8), handling temperature (T) and water content (ϑ_w) in a coupled manner (see Westermann et al. (2016) for details). This is to ensure that energy increase corresponding to a potential increase of T above the melting point is diverted to melting parts of the snow matrix, and increasing ϑ_w. The effective thermal conductivity of snow, k^*_{snow}, is derived from the parametrization by Yen (1981):

$$k^*_{snow} = k_{ice}\left(\frac{\rho_{snow}}{\rho_{water}}\right)^{1.88}$$

(Eq. 9)

However, the validity of this equation is extended for cold environments by using a temperature dependent expression of the thermal conductivity of ice (Choi & Okos, 1986, as cited in Fricke & Becker, 2001):

$$k_{ice} = 2.2196 - 6.2489 * 10^{-3} * T + 1.0154 * 10^{-4} * T^2$$

(Eq. 10)

Where *T* denotes the snow temperature. It should be noted that snow densities are not explicitly calculated in *CG Crocus*, but are diagnostically derived by the layer thickness, and the column of water and ice of each layer. For simplicity the density of both ice and water are set to 1000 kg/m^3, which entails that k^*_{snow} in Eq. 9 approaches k_{ice} for ice fractions nearing unity, in agreement with Yen (1981).

The hydrological scheme of the snowpack follows the *1D cold-hydrology* scheme presented in Westermann et al. (2011). Each snow layer has a field capacity of the amount of liquid water it can hold against the pull of gravity, defined to be to 5% of its pore space (Pahaut, 1976). Water in excess of the field capacity infiltrates downward, filling consecutive layers to their field capacity until reaching the base of the snowpack, from where water pools up. If there is no more available pore space in the uppermost grid cell, excess water is assumed to drain instantly from the system.

Crocus scheme: Snowfall

In the *Crocus scheme,* snowfall is added with properties as they are detailed in Vionnet et al. (2012). The density of fresh snow, ρ_{new}, is given as a function of the air temperature, T_{air}, and the current wind speed, *U*:

$$\rho_{new} = \min\left(\rho_{min}, a_\rho + b_\rho(T_{air} - T_m) + c_\rho U^{\frac{1}{2}}\right)$$

(Eq. 11)

Where $a_\rho = 109$ kg/m^3, $b_\rho = 6$ kg/(m^3*K) and $c_\rho = 26$kg/(m$^{7/2}$*s$^{1/2}$) are empirical constants, and T_m is the melting point of water. The minimum density of fresh snow, ρ_{min}, is set to 50 kg/m^3. The sphericity and dendricity of falling snow are given as:

$$s_{fall} = min[max(0.08U + 0.38, 0.5), 0.9]$$

$$d_{fall} = min[max(1.29 - 0.17U, 0.2), 1]$$

(Eqs. 12 and 13)

This gives increasing densities with increasing wind speed and air temperature, and rounder (lower sphericity) and less dendritic grains with increasing wind speed. The grain size of falling snow is derived from its sphericity and dendricity:

$$g_{s,fall} = 10^{-4} + (1 - d_{fall})(3 * 10^{-4} - 10^{-4} s_{fall})$$

(Eq. 14)

The energy associated with snowfall, E_{new}, is derived from air temperature:

$$E_{new} = P_s * \Delta t * \left(min(T_m, T_{air}) * c_i - L_f\right)$$

(Eq. 15)

Where P_s is the snowfall rate (in kg/s/m^2), Δt is the timestep, c_i is the specific heat capacity of ice, and L_f is the latent heat of fusion of water. This implies that dry snow at the melting point has energy E = 0. Fresh snow is added to the uppermost snow layer by summation of their extensive state variables (energy, mass etc.) and linear mixing of the snow properties weighted by ice mass.

Crocus scheme: Surface energy balance

The parameterizations employed in the calculation of the SEB in *the Crocus scheme* deviates from the *simple snow scheme* in two aspects: the albedo, and the transmission of solar radiation. The evolution of albedo in Westermann et al. (2016) is parameterized following ECMWF (2007), giving a rate of albedo decrease after a snowfall event by empiric relations depending on liquid water presence and time since last snowfall. In the *Crocus scheme* the reflection and transmission of incoming shortwave radiation, R_s, is handled on separate spectral bands. R_s is split into the ranges [0.3-0.08, 0.8-1.5, 1.5-2.8 µm], which are weighted with the coefficients 0.71, 0.21 and 0.08, respectively. This allows for incorporation of effects that mainly affect specific parts of the shortwave specter (e.g. light absorbing impurities have a pronounced impact on the visible and UV range). For each spectral band a spectral albedo, α, is calculated for the surface layer, and an absorption coefficient, β, is calculated for all layers (Table 5). These parameterizations rely on the optical diameter of snow, d_{opt}, which can be derived from the microstructure of each snow layer:

$$d_{opt} = \begin{cases} 10^{-4}[d + (1-d)(4-s)], & d > 0 \\ g_s * s + (1-s) * \max\left(4.1^{-4}, \frac{g_s}{2}\right), & d = 0 \end{cases}$$

(Eq. 16)

Shortwave radiation penetrating into the snowpack is assumed to decay exponentially with depth, and at a depth z below the snow surface, the solar flux, Q_s, is:

$$Q_s = \sum_{k=1}^{3} (1 - a_k) R_{s,k} e^{-\beta_k z}$$

(Eq. 17)

Where the subscript *k* denotes the different spectral bands. Any shortwave radiation penetrating to the base of the snowpack is added to the lowermost snow cell.

Spectral band	Albedo *α*	Absorption coefficient *β* (/m)
0.3 – 0.8 µm	$\max(0.6, \alpha_i - \Delta\alpha_{age})$ $where\colon \alpha_i = \min\left(0.92, 0.96 - 1.58\sqrt{d_{opt}}\right)$ $\Delta\alpha_{age} = min\left(1, \max(\frac{P}{P_{CDP}}, 0.5)\right) * \frac{0.2 * A}{60}$	$max\left(40, \frac{0.00192\rho}{\sqrt{d_{opt}}}\right)$
0.8 – 1.5 µm	$\max\left(0.3, 0.9 - 15.4\sqrt{d_{opt}}\right)$	$max\left(100, \frac{0.00192\rho}{\sqrt{d_{opt}}}\right)$
1.5 – 2.8 µm	$346.3d' - 32.31\sqrt{d_{opt}} + 0.88$	$+\infty$

Table 5: Evolution of snow albedo and absorption coefficient for the three spectral bands used in the Crocus scheme. A is the age of the snow surface in days, d_{opt} is in m (Eq. 16), and P is the mean pressure and P_{CDP} = 870, both in hPa. See Vionnet et al. (2012) and references therein. CDP presumably denotes their validation site – Cole de Porte, France.

Crocus scheme: Snow metamorphism

The metamorphism of snow grains once they are deposited on the ground can be described in a phenomenogical way by a comprehensive set of equations (Vionnet et al., 2012). A distinction is made between dry metamorphism, which depends primarily on the vertical temperature gradient *G*, and wet metamorphism, which pivots on whether the snow grains are round (s=1) or angular (s<1). Both dry and wet metamorphism discriminate between the metamorphism of dendritic (d>0) and non-dendritic (d=0) snow grains, and are compiled in Table 6 and Table 7, respectively. Some of the qualitative effects captured by this set of equations include:

- A decrease of dendricity with time
- The rounding of grains when the temperature gradient is small or water is present
- An increase in angularity (faceting) for grains subject to strong temperature gradients
- The growth of round grains under wet conditions

	Non-dendritic snow (d = 0)	Dendritic snow (d > 0)
G ≤ 5	$\frac{\delta s}{\delta t} = 10^9 e^{-\frac{6000}{T}}$ $\frac{\delta g_s}{\delta t} = 0$	$\frac{\delta d}{\delta t} = -2.10^8\, e^{-\frac{6000}{T}}$ $\frac{\delta s}{\delta t} = 10^9\, e^{-\frac{6000}{T}}$
5 < G ≤ 15	$\frac{\delta s}{\delta t} = -2.10^8 e^{-\frac{6000}{T}} * G^{0.4}$	$\frac{\delta d}{\delta t} = -2.10^8\, e^{-\frac{6000}{T}} * G^{0.4}$
G > 15	$if\ s > 0\!: \frac{\delta d}{\delta t} = -2.10^8\, e^{-\frac{6000}{T}} * G^{0.4}\ and\ \frac{\delta g_s}{\delta t} = 0$ $if\ s = 0\!: \frac{\delta s}{\delta t} = 0\ and\ \frac{\delta g_s}{\delta t} = f(T)h(\rho)g(G)\Phi$	$\frac{\delta s}{\delta t} = -2.10^8\, e^{-\frac{6000}{T}} * G^{0.4}$

Table 6: Empirical law detailing dry snow metamorphism. T and G are in K and K/m, respectively. F, g, h and Φ are functions detailing the growth of depth-hoar, see Vionnet et al. (2012) and references therein.

	Non-dendritic snow (d = 0)	Dendritic snow (d > 0)
0 ≤ s < 1	$\frac{\delta g_s}{\delta t} = 0\ and\ \frac{\delta s}{\delta t} = \frac{1}{16}\theta^3$	$\frac{\delta d}{\delta t} = -\frac{1}{16}\theta^3$
s = 1	$\frac{\delta s}{\delta t} = 0\ and\ \frac{\delta v}{\delta t} = v_0' + v_1'\theta^3$	$\frac{\delta s}{\delta t} = \frac{1}{16}\theta^3$

Table 7: Empirical laws detailing wet snow metamorphism. Θ is the mass liquid water content, t is time in days, and v_0' and v_1' are empirical constants – see Vionnet et al. (2012) and references therein.

Crocus scheme: Density evolution

The new parameterizations in the *Crocus scheme* include two mechanical effects that rise the density of snow layers: settling due to the pressure of overlying layers, and break up of snow grains during drift events. Note that densities also increase due to refreezing of liquid water. The former effect is expressed as a compaction rate for each snow layer given by the vertical stress of overlying layers, *σ*, and the viscosity of the compacted layer, *η*:

$$\frac{dD}{D} = \frac{-\sigma}{\eta} dt$$

(Eq. 18)

where *D* is the layer thickness. The snow layers above the current layer, *i*, exerts the vertical stress:

$$\sigma_i = \sum{}^{i-1}_{\ \,1}{}^{1} g * \cos(\Theta) * \rho_i\, D_i$$

(Eq. 19)

where g is the gravitational constant and Θ is the local slope. The uppermost layer experiences a vertical stress corresponding to half its weight. The viscosity of a layer is derived from empirical functions relating its temperature, density, water content, and grain size:

$$\eta = f_1 f_2 \eta_0 \frac{\rho}{c_\eta} exp\left(a_\eta\left(T_{fus} - T\right) + b_\eta \rho\right)$$

(Eq. 20)

where $\eta_0 = 7.62237*10^6$ kg/(m*s), $a_\eta = 0.1$ 1/K, $b_\eta = 0.023$ m^3/kg, $c_\eta = 250$ kg/m^3, and f_1 and f_2 are correctional functions to account for viscosity increase due to water presence and viscosity decrease with angular grains, respectively:

$$f_1 = \frac{1}{1 + 60\frac{W_{liq}}{\rho_w D}}$$

$$f_2 = \min[4.0, \exp(\frac{\min(g_1, g_s - g_2)}{g_3})]$$

(Eqs. 21 and 22)

where W_{liq} is the snow layer water content, ρ_w is the density of water, and g_1 = 0.4 mm, g_2 = 0.2 mm and g_3 = 0.1 mm.

The second mechanical effect accounted for is the impact on wind drift on surface layers, which also affects snow grains. The potential of a snow layer to be eroded depends on its microstructural properties, which is described by a mobility index:

$$M_O = \begin{cases} 0.34(0.75d - 0.5s + 0.6) + 0.66F(\rho), & d > 0 \\ 0.34(-0.583g_s - 0.833s + 0.833) + 0.66F(\rho), & d = 0 \end{cases}$$

(Eq. 23)

where $F(\rho) = 1.25 - 0.0042(max(\rho_{min}, \rho) - \rho_{min})$ and $\rho_{min} = 50$ kg/m^3. The first term describes the erodability of alpine snow, whereas the second term extends the applicability to polar snow ($\rho > 330$ kg/m^3). To determine whether a layer can be eroded under the current wind conditions, the mobility index is combined with the wind speed to compute a driftability index:

$$S_I = -2.868\exp(-0.085U) + 1 + M_O$$

(Eq. 24)

This index discriminates between events of drifting snow ($S_I > 0$) and when no wind drift occurs ($S_I \leq 0$). During snow drifting, the grains break when they collide with each other and the surface. This gives a fragmentation of snow grains, and a compaction of surface layers. To limit the effect of drift events to surface layers, a *time characteristic for snow grain change under wind transport* is computed for each layer:

$$\tau_i = \frac{\tau}{\max[0, S_{I,i}\exp({}^{-z_i}/_{0.1})]}$$

$$z_i = \sum_j (D_j * (3.25 - S_{I,j}))$$

(Eqs. 25 and 26)

Where τ is an empirical constant set to 48h. z_i is a pseudo-depth for each layer, which is parameterized to encompass the reduced driftability due to hardening of layers, *j*, overlying the current layer, *i*. The time characteristic thus exhibits an exponential decay with depth until a non-transportable layer is reached. For driftable surface layers, the denominator in Eq. 25 is equal to S_I. From this, compaction and fragmentation rates are derived following Table 8. τ_i is in effect a measure of the impact of snow drift on each snow layer, which is used in section 3.3.3 to derive snow erosion rates.

Parameters	Non-dendritic snow (d = 0)	Dendritic snow (d > 0)
Grain properties	$\frac{\delta s}{\delta t} = \frac{1-s}{\tau}\ and\ \frac{\delta g_s}{\delta t} = \frac{5.10^{-4}}{\tau}$	$\frac{\delta d}{\delta t} = \frac{d}{2\tau}\ and\ \frac{\delta s}{\delta t} = \frac{1-s}{\tau}$
Snow density	$\frac{\delta \rho}{\delta t} = \frac{\rho_{max} - \rho}{\tau}\ where\ \rho_{max} = 350\frac{kg}{m^3}$	

Table 8: Empirical laws detailing the evolution of snow grain properties caused by snow transport. t is the time in hours, and τ is the time characteristic of snow grain change (Eq. 25).

3.3.3 Lateral exchange of water and snow

Tiling approach

The core of this study is to resolve sub-grid variability induced by lateral mass fluxes during winter. To achieve this, the modular setup of CryoGrid is advanced to run parallel simulations. The way this is achieved is inspired by Nitzbon et al. (2019), where a previous (non-modular) version of CryoGrid is parallelized. Section 2.3 details the theoretical and technical basis on which the parallel computation is implemented.

The simulated landscape is divided into units representing distinct topographic elements. Each unit is represented by a *tile*, which is assigned a relative altitude, *A*, surface area, a_{rel}, and surface exposure, *e*. The relationships between tiles are defined by their distance, D^{hy}, and contact length, *L*, to another.

Lateral exchange is set to occur at specified times, governed by a user-defined lateral interaction time step, Δt_{lat}. This setup is chosen because lateral exchange after each model-time step is not feasible, as each tile runs with its own adaptive timestep. Upon reaching an interaction time, information about the tiles current state is exchanged, and the bulk fluxes going in and out of each tile are calculated and scale according to their respective area.

Lateral snow transport

To describe snow erosion and deposition in a process-based way, the wind drift parameterizations from Vionnet et al. (2012) are utilized. The potential for snow erosion is captured in the time characteristic for snow grain change under wind transport, $\tau_{i,}$ which combines the potential of a snow layer to be eroded under the current conditions (S_l), while limiting the effect to surface layers. Based on this, the fraction of a snow layer that potentially can be eroded within a lateral interaction timestep is quantified as:

$$\theta_{mobile,i} = \frac{N_{drift}}{\tau_i} * \Delta t_{lat}$$

(Eq. 27)

Where N_{drift} is an empirical drift factor, which together with the time characteristic constitutes a "potential erosion rate". The degree to which a tile is subject to snow erosion or deposition during drift events, depends on where its exposure ranks compared to the other tiles. The exposure e is a transient quasi-altitude given by

$$e(t) = e_{init} + d_{snow}(t)$$

(Eq. 28)

From this, a snow exchange index is calculated during each lateral interaction timestep, by normalized difference of the total area with a higher exposure, A_{above}, and lower exposure, A_{below}, than the current tile (i):

$$I_{drift}(e_i) = \frac{A_{above} - A_{below}}{A_{above} + A_{below}}$$

(Eq. 29)

A tile with a negative snow exchange index looses snow equal to $-\vartheta_{mobile} * I_{drift}$ for each mobile layer. Snow fluxes between tiles with negligible difference in exposure is prevented by introducing a threshold difference, δe, which needs to be exceeded for a tiles to be considered above or below each other. All snow which is eroded is added to a pool of drifting snow, where the extensive state variables (energy, mass) are summed and the snow properties (*d*, s, g_s, density) are linearly mixed based on the ice mass eroded from each layer. This pool is distributed among the receiving tiles ($I_{drift} > 0$) based on normalization of their snow exchange indexes. Lateral snow transport can only be included in CryoGrid when using the *Crocus scheme*, as the description of snow microphysics is required to derive the potential for erosion.

Lateral water percolation

The flow of water between neighboring tiles is given as bulk fluxes based on Darcy's law. Water exchange between unfrozen soil columns follows Nitzbon et al. (2019), whose code is transcribed to the modular code structure of *CG Crocus*. For the soil case, the lateral influx of water (q_α^{hy}) to a tile α from adjacent tiles is:

$$q_\alpha^{hy} = \sum_{\beta \in N(\alpha)} K_{\alpha\beta} \frac{w_\beta - max(w_\alpha, f_\alpha)}{D_{\alpha\beta}^{hy}} \frac{H_{\alpha\beta} L_{\alpha\beta}}{A_\alpha}$$

(Eq. 30)

Where N(α) denotes all tiles adjacent to tile α, which has the area A_α. $K_{\alpha\beta}$ is the saturated hydraulic conductivity between two tiles α and β, while *w* and *f* denote the water and frost table (base of active layer), respectively. $L_{\alpha\beta}$ is the contact length, while $D_{\alpha\beta}^{hy}$ is the distance between the tiles α and β. $H_{\alpha\beta}$ is the hydraulic contact length, which is calculated as:

$$H_{\alpha\beta} = \min[w_\beta - \max(w_\alpha, f_\alpha), w_\beta - f_\beta]$$

(Eq. 31)

The gravity driven flow of water within the snow cover is likely a key process to adequately reproduce the effects of ROS-events on local snow cover and ground thermal regime. Thus, water exchange among adjacent, snow covered tiles is prescribed by a modification of Eq. 30:

$$q_\alpha^{hy} = \sum\nolimits_{\beta \in N(\alpha)} K_{snow}^{hy} \frac{w_\beta - \max(w_\alpha, f_\alpha)}{D_{\alpha\beta}^{hy}} \frac{H_{\alpha\beta} L_{\alpha\beta}}{A_\alpha}$$

(Eq. 32)

Where K^{hy}_{snow} is the saturated hydraulic conductivity of snow. For snow, *f* is the depth below which no mobile water is present in the snowpack (base of the snowpack or top of basal ice).

For both the soil and snow case, the water fluxes are scaled so they do not exceed the available water at the draining tile. Water inflow to a soil column is added to the uppermost ground cell, and infiltration follows the same scheme as for rainfall. Water exchange between snow covered tiles is assumed to occur below the snow cover, and is thus added by pooling up from the base of the receiving tile. No water fluxes occur between adjacent tiles if they are not both either snow covered or snow-free, nor for tiles that are snow-free but feature a frozen surface cell.

3.3.4 Derivation of surface runoff

The surface runoff of the system is not explicitly calculated in *CG Crocus*, but it can be derived diagnostically from the water-balance equation (Dingman, 2015):

$$P + GW_{in} + ET - (Q + GW_{out}) = \Delta S$$

(Eq. 33)

where P is the precipitation, GW_{in} and GW_{out} is the groundwater inflow and outflow, respectively. Q is the streamflow (surface runoff), ET is the evapotranspiration and ΔS is the change in water storage (liquid and solid). For single-tile simulations, no groundwater exchange with the surroundings is included in *CG Crocus*, and Eq. 33 simplifies to:

$$Q = P + ET - \Delta S$$

(Eq. 34)

For all simulations presented in this thesis, the model state is outputted four times per day, and Eq. 34 is calculated over this time interval. The required variables are obtained by accumulating P and ET between two output times, and calculating the change in stored water over this time.

For multi-tile simulations, the contribution from each tile is scaled according to its area to get the total runoff from the system. For this case, lateral fluxes of water and snow need to be considered, and they are accumulated between output times and included as a combined groundwater term, GW:

$$Q = P + ET + GW - \Delta S$$

(Eq. 35)

Due to numerical inaccuracies in the calculation of lateral water fluxes over these time intervals, marginal negative runoff values may occur, but these are removed from the time series.

3.4 Model setup

3.4.1 Bayelva

For the Bayelva study area, the goal is to capture how the newly included processes of lateral redistribution of mass act on a simplistic representation terrain features. The landscape is divided into three units representing distinct elements of the local topography: exposed ridges (R), snowbeds (S) in depressions and adjacent to slopes, and ambient (A) flat surroundings. These units are represented by three tiles connected laterally in a two-dimensional fashion. The tiles are assigned relative elevations, distances and areas loosely based on the terrain profiles and the topography of the area (Figure 4 and Figure 5). In Figure 10, the hydraulic setup of the system is schematically presented, and the attributes of each tile summarized in Table 9. The setup is further simplified by setting the exposure, *e*, equal to the relative altitude, a_{rel}, of each tile, so that redistribution of snow only occurs from higher to lower elevations. This implies that the wind direction and the formation of snowdrifts at lee slopes are not taken into account. To assess the added insight of the three-tile simulations, a standalone simulation without lateral fluxes is run (referred to as *single-tile control simulation*), featuring the same configurations as the ambient tile.

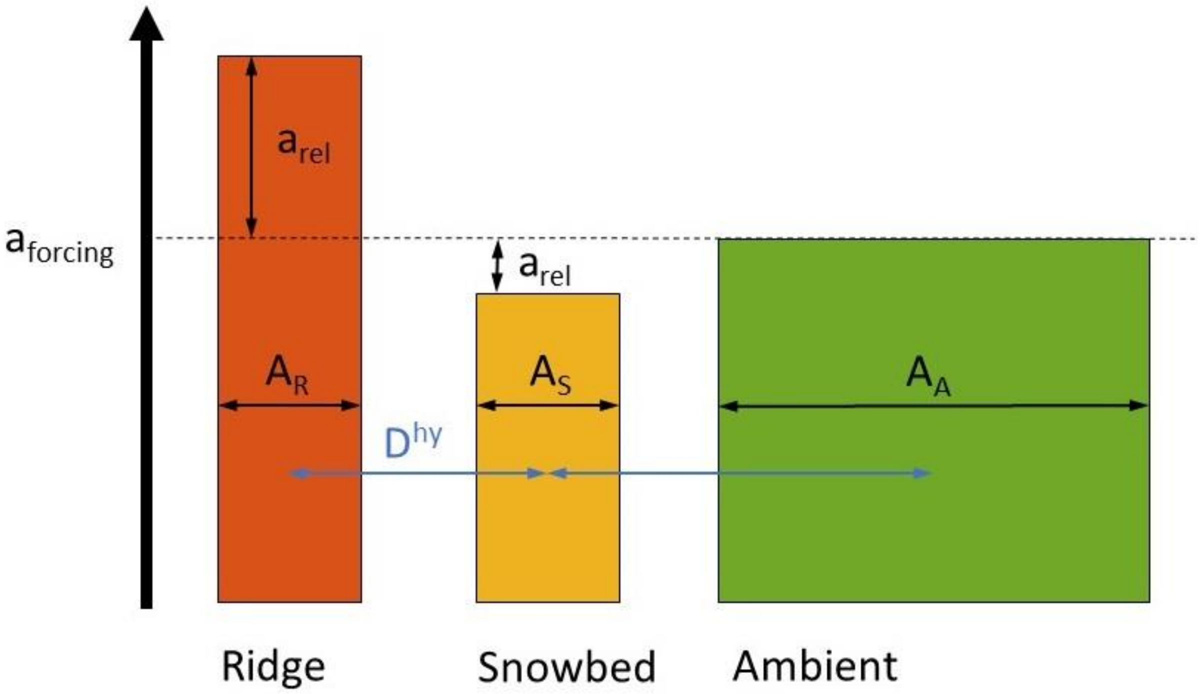

Figure 10: Schematic cross-section of the hydrological setup of the laterally connected three-tile system. Translational symmetry of this plane is assumed.

Parameter	Symbol	Unit	Ridge	Snowbed	Ambient
Area	A	m2	100	100	300
Relative altitude	a_{rel}	m	10	-1.5	0
exposure	e_{init}	m	10	-1.5	0
Hydraulic distance	D^{hy}	m	100	200	
Contact length	L	m	10	10	

Table 9: Parameters specifying the topography and hydraulic connections of the tiling scheme.

The modelled soil domain consists of 5 meters of sediments overlying bedrock, which extends down to 100 m below the surface. The ground stratigraphies (Table 10 & Table 11) of the tiles are deduced from the soil surveys in Boike et al. (2018). The ridge tiles differs somewhat from the snowbed and ambient tile by having a higher mineral fraction and no organic layer, in agreement with qualitative field observations. At the lower boundary of the simulated domain, a geothermal heat flux of 0.05 W/m^2 is applied. The tiles are initialized the with a temperature profile for late fall derived from measurements from the nearby, instrumented borehole (Boike et al., 2018): 0m, 5°C; -1.7m, 0°C; -10m, -2.5°C. The base of the permafrost is fixed to 100m depth, which is a typical value for coastal areas on Svalbard (Liestøl, 1975).

Depth (m)	Mineral fraction	Organic fraction	Field capacity	Soil type	Initial water fraction
0 – 0.1	0.5	0.05	0.2	sand	0.45
0.1 – 5	0.5	0	0.2	sand	0.5
5 – 100	0.97	0	0.03	sand	0.03

Table 10: Subsurface stratigraphy of the snowbed and ambient tile.

Depth (m)	Mineral fraction	Organic fraction	Field capacity	Soil type	Initial water fraction
0– 5	0.6	0	0.2	sand	0.4
5 – 100	0.97	0	0.03	sand	0.03

Table 11: Subsurface stratigraphy of the ridge tile.

Soil and snow parameters are equal for all tiles, and are presented in Table 13. To the extent possible they are taken from Boike et al. (2018), while snow parameters associated with the CROCUS scheme are set to the default value presented in Vionnet et al. (2012).

Parameter	Symbol	Value	Unit	Reference
		Soil		
Albedo	α_{soil}	0.15	[-]	Boike et al. (2018)
Emissivity	ε	0.99	[-]	
Roughness length	z_0	0.001	m	Boike et al. (2018)
Root depth	D_T	0.05	m	
Evaporation depth	D_E	0.05	m	
Hydraulic conductivity	K^{hy}	0.00001	m/s	Boike et al. (2018)

Table 12: Model parameters and settings for all simulations.

		Snow		
Emissivity	ε	0.99	[-]	
Roughness length	z_0	0.0001	m	Boike et al. (2018)
Field capacity	θ_{fc}	5	[%]	Pahaut (1976)
Hydraulic conductivity	K^{hy}	0.001	m/s	Boike et al. (2018)
Timescale winddrift	τ	48	hours	Vionnet et al. (2012)
		Lateral		
Lateral interaction time step	Δt_{lat}	1	hour	
Exposure threshold difference	δe	0.1	m	This study
Drift factor	N_{drift}	5	[-]	This study

Table 13: Model parameters and settings for all simulations. (Continuation from previous page)

3.4.2 Nordenskiöld land

Apart from what is described in Section 3.1.4, little site-specific information is available for the locations in Nordenskiöld land. This study area thus provides the opportunity to explore the applicability of *CG Crocus* for sites where no detailed survey has been done. The simulations are done for each of the combinations of subareas (Coles Bay and Gangdalen) and relative elevations (upper and lower). For each of these topographic settings, forcing data was downloaded for the grid point in AROME-Arctic with an elevation closest to those of the measurements (Table 1), but no further away than 5 km.

Within each setting, ground surface temperature measurements are done at two levels of exposure, named “ridge” and “subridge”. Each simulations is thus set to include two almost identical square tiles, apart from that one is somewhat higher and more exposed than the other (Table 14). The ridge and subridge tile are connected through a hydraulic distance and contact length, which both are 10 m. For simplicity, all simulations on Nordenskiöld land are assigned the same soil stratigraphy (Table 10), model parameters (Table 13) and temperature gradient as used for the Bayelva area.

Tile	Area	Relative elevation	exposure
Ridge	100 m^2	1 m	1 m
Subridge	100 m^2	0 m	0 m

Table 14: Topographical properties of the tiles in all simulations for Nordenskiöld land.

3.4.4 Garwoodtoppen

The simulations of *Garwoodtoppen* and the adjacent glacier *Kronebreen* feature the largest horizontal dimensions of the study sites. The tile representing *Garwoodtoppen* is assigned the dimensions 1*1 km and the tile representing the part of *Kronebreen* that receives snow has the dimensions 2.5*2.5 km. These two tiles are connected through a hydraulic distance and contact length of 1 km. Owning to these distances, a dedicated forcing time series are downloaded for each of the two tiles. In AROME-Arctic, the highest grid point in the area has an elevation of 669 m a.s.l., which is within the range of the peaks of *Garwoodtoppen*. The grid point chosen for *Kronebreen* features an elevation of 208 m a.s.l., which is representative for the parts of the glacier neighboring Garwoodtoppen. As these tiles already inherently features an elevation difference from the forcing data, the exposure and relative elevation do not need to be adjusted manually to allow for lateral fluxes. For both tiles, all parameters are set equal to those of the ridge tile in the three-tile simulations for the Bayelva area (Table 11 and Table 13), including the temperature profile. For comparison, a single-tile simulation without lateral fluxes is done for Garwoodtoppen.

3.4.3 Suossjavri

The model setup for the palsa mires at Suossjavri follow Aas et al. (2019) to the extent possible. The site is within the domain of AROME-Arctic (Figure 3), and forcing data for the site (335 m a.s.l.) is extracted. The modeled wind speeds for Suossjavri are low (95% below 6.5 m/s), so to produce snow redistribution during winter, all wind speeds for this site are doubled. The landform is simulated by two interacting tiles: a circular peat mound ("*palsa*") with 10 m diameter, within a 100*100 m mire ("*mire*"). The *palsa* has relative elevation and exposure elevated 0.75 m above those of the *mire,* and the tiles have a contact length of 31.4 m and a hydraulic distance of 10m. Both tiles feature a soil column of 14 m, which is set to be isothermal at zero degrees at the start of the simulations. The simulations by Aas et al. (2019) utilize NOAH-MP, and the manner in which soil properties are represented in this LSM, especially the water retaining properties, differs from *CG Crocus* (Niu et al. (2011) and references herein). Consequently, a direct transfer cannot be done, but the soil stratigraphies assigned for the Suossjavri site are kept as close to the implementation in Aas et al. (2019) and Niu et al. (2011) as possible, see Table 15.

Depth (m)	Mineral fraction	Organic fraction	Field capacity	Soil type	Initial water fraction
0 – 14	0.1	0.4	0.2	sand	0.5

Table 15: The soil stratigraphy of the "palsa" and "mire" tiles.

4 Results

This chapter includes examples of processes captured by *CG Crocus* (Section 4.1), the results from the validation study of the modelling approach (Section 4.2), and examples of potential applications (Section 4.3). Section 4.1 showcases events of lateral snow and water transport (Sect. 4.1.1), and elaborates on how this affects the hydrological regime of the area (Sect. 4.1.2). In Section 4.2, the results from a systematic comparison of the simulations and observations of snow depth and SWE (Sect. 4.2.1) and ground surface temperatures (Sect. 4.2.2), as well as a sensitivity study of the lateral snow transport parameterizations (Sect. 4.2.3). Section 4.3 compiles results outlining potential applications of *CG Crocus*, including over elevation gradients (Sect. 4.3.1) and specific landforms (Sect. 4.3.2 and 4.3.3). Preliminary results from *CG Crocus* including only snow redistribution by wind can be found in the Appendix.

4.1 Process-based lateral redistribution SWE

4.1.1 Example events of snow and water exchange

The newly implemented lateral transport processes in *CG Crocus* produce a spatially differential buildup of the snow cover. Most notably, this includes snow relocation among simulated tiles by wind drift, of which an example from 2019 is provided in Figure 11. A thin layer of low-density snow accumulates in all tiles during calm wind conditions around 20th of February (event 1 in Figure 11). When snowfall is accompanied by strong winds (event 2 in Figure 11), more snow accumulates in the snowbed, while only marginal amounts are deposited on the ridge. This preferential deposition is not explicitly handled in *CG Crocus*, but the lateral interaction timestep of one hour in the presented setup is able to reproduce this effect. The strong wind during event 2 also give a compaction of surface layers in all tiles, but parts of the low-density snow from event 1 are sufficiently shielded in the snowbed and only experience moderate density increase. Following the deposition during event 2, the thin snow cover on the ridge tile is subject to erosion during several windy events, and completely disappears by March 9 (event 3 in Figure 11).

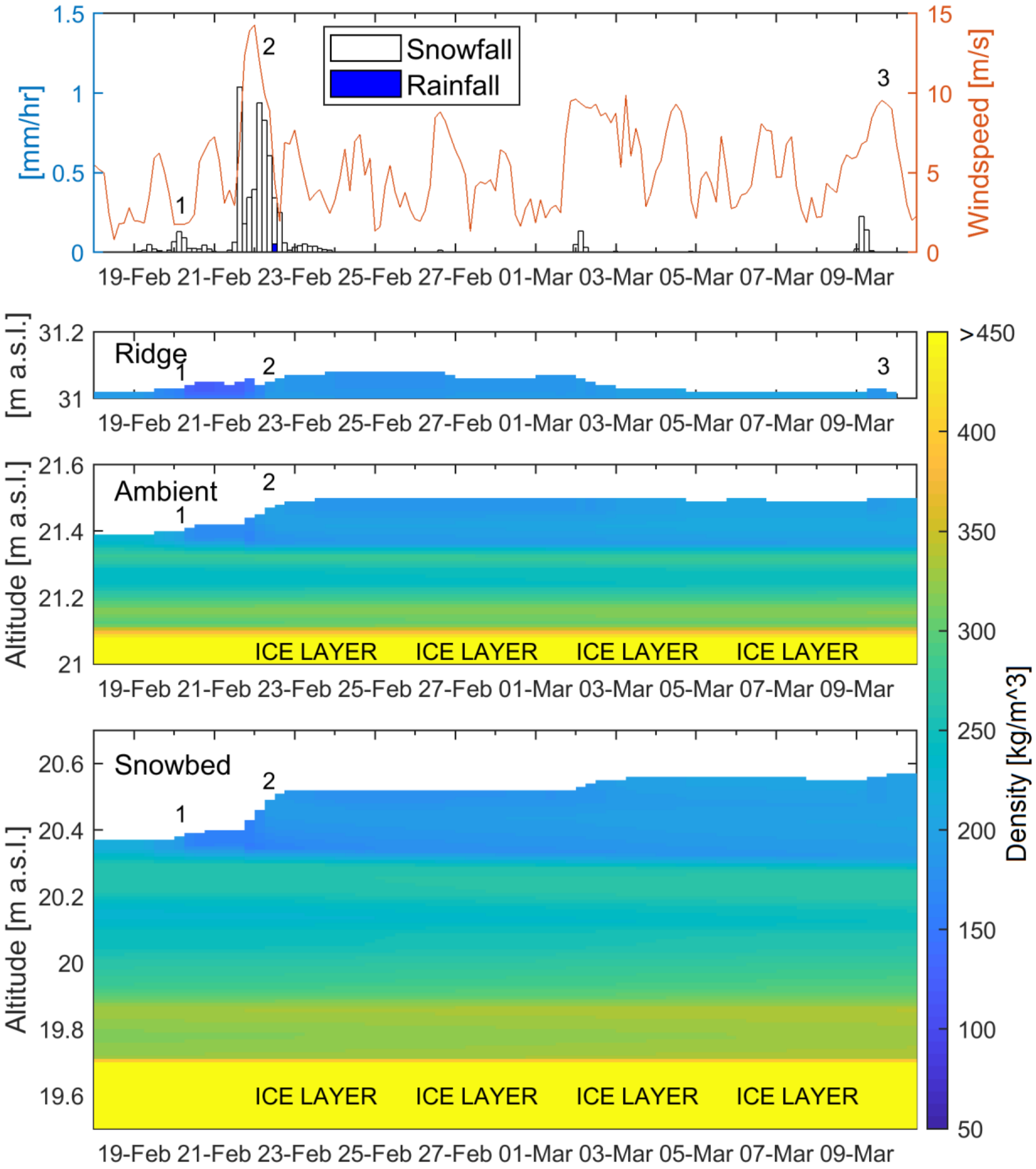

Figure 11: Example situation for meteorological conditions (3-hourly forcing data; year 2019; top panel) leading to different accumulation and erosion for the three-tile simulation (three lower panels). "ICE LAYER" indicates areas with densities > 900kg/m3.

Lateral exchange of water between snow-covered tiles is another novel feature of *CG Crocus*. Figure 12 displays an example of the different response among the tiles during and after a pronounced ROS-event in April 2019. During a smaller preceding ROS-event (event 1 in Figure 12), the liquid water is retained within the snowpack. When rainfall is heavier, the water percolates to the base of the snowpack where it pools up (event 2 in Figure 12), and the snowpack becomes isothermal. The water in the ridge tile quickly refreezes, while the liquid water in the ambient and snowbed tile is insulated from the lower surface temperatures by their snow cover, substantially slowing the refreezing. After the event, water exceeding the snowpacks field capacity gradually drains from the ambient to the snowbed tile, allowing the snow cover in the ambient tile to refreeze while the snowbed tile experiences long-lasting presence of liquid water at the base of the snowpack (event 3 in Figure 12). This is in agreement with field observations done the 23. – 25. April, was found at the base of some deeper snow pits. For this specific case, the snowbed tile did not completely refreeze again during the snow season (Figure 16). Note that prior to this ROS-event (Figure 11 and Figure 12), basal ice layers of different thickness are evident in the ambient and snowbed tiles (10 and 20 cm, respectively), which have been present since the last ROS-event in December 2018 (Figure 14).

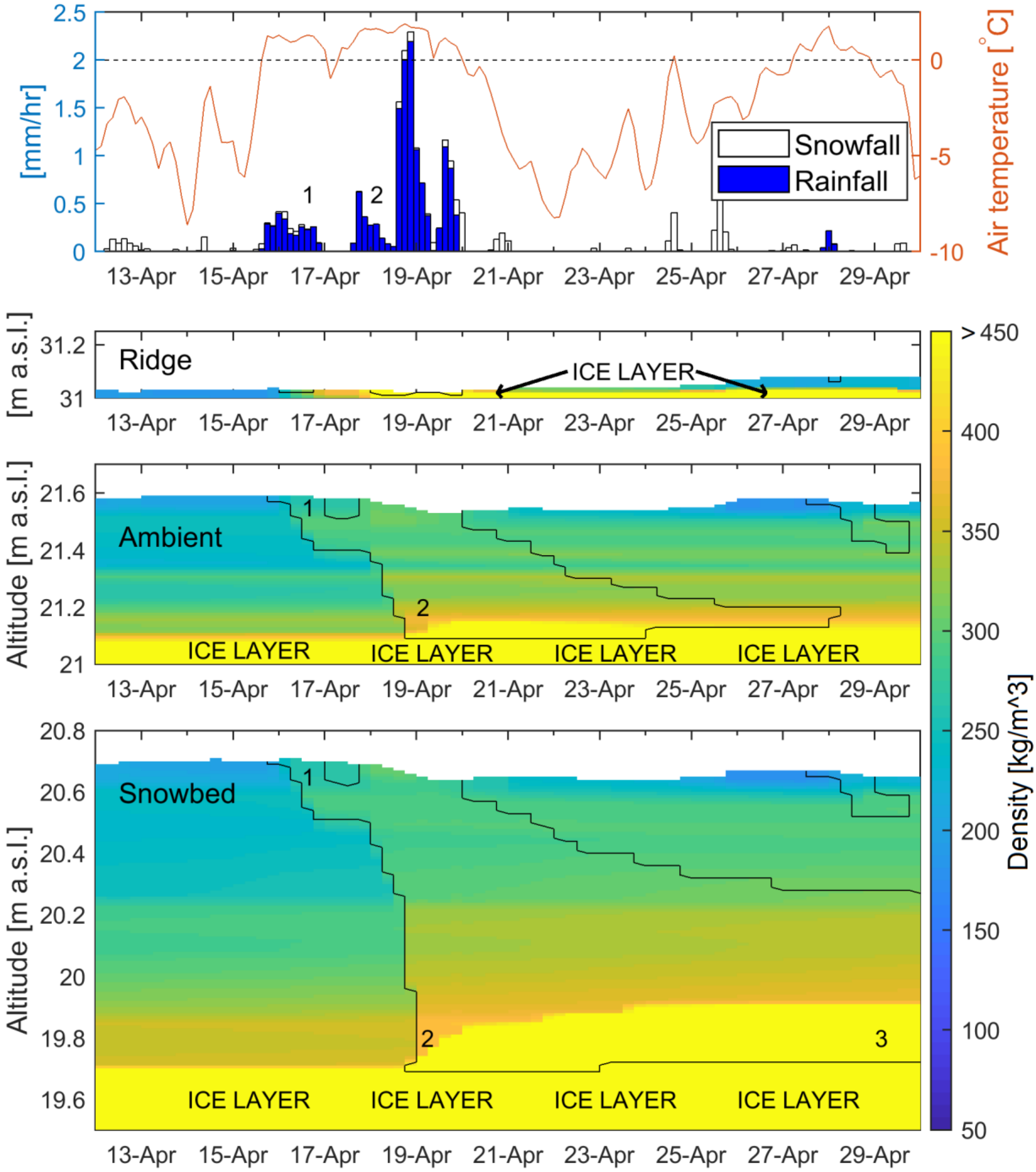

Figure 12: Example of meteorological conditions (top panel) and snow cover response in the three tiles (lower three panels) during and after a heavy ROS-event in 2019. The text "ICE LAYER" indicates areas with densities > 900kg/m3. The black line shows the 0°C isotherm, delineating the areas where liquid water is present.

4.1.2 Surface runoff

The differential buildup of the snow cover described in Section 4.1.1 will influence the hydrology of the study area through the routing of water and the spatial variability in snow ablation. Comparing the hydrographs from the *single-tile control simulation* and the three-tile simulations from Bayelva

(Figure 13) reveals some differences and similarities. As water in the tiled simulation drains to the lowest tile, smaller rainfall amounts are required to saturate this tile and generate runoff in summer. Both simulations show runoff in response to two ROS-events in November 2018, as the snow cover at that time is sufficiently thin to be saturated (Figure 14). Neither of the simulations produce runoff between these ROS-events and snowmelt in June 2019, because when a substantial snow cover is present, extraordinarily large rain amounts would be required to saturate the snow column (e.g. Figure 12). This is contrary to field observations on the 23. - 25. April 2019, where 2-5 cm of surface water above thick ice layers was observed in lower lying areas of the Bayelva area. This discrepancy is because lateral seepage of water occurs in reality, but this is not included in *CG Crocus*.

However, the three-tile simulation produces a different runoff pattern during snowmelt than the *single-tile control simulation* (Figure 13). While the timing and the magnitude of the peak runoff are comparable among the simulations, the tiled setup produces runoff over a longer time span. This is because the large amounts of snow present in the snowbed tile require substantially more energy, and consequently time, to melt. This is in qualitative agreement with field observations from low elevations at Svalbard, where snowdrifts persist and discharge water until mid-summer.

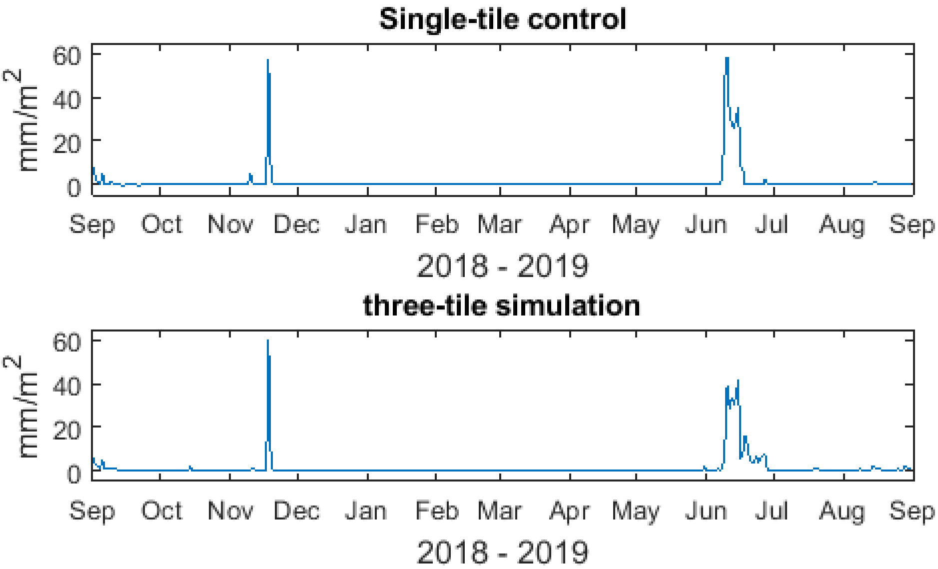

Figure 13: Daily surface runoff for the Bayelva area for the hydrological year 2019. Results from the single-tile control simulation (top pane) and for the three-tile simulation (lower pane).

4.2 Validation study

4.2.1 Sub-grid evolution of snow depth and SWE

In this section a comparison of the transient three-tile simulations against single-tile reference runs, and an evaluation of the simulated end-of-season snow properties versus field observations from the Bayelva area is presented. Figure 14 shows the snow depth evolution over the three simulated snow seasons, revealing clear differences in the amount and length of snow cover, both among the seasons and among the different simulations. The ambient tile displays an almost identical behavior as the *single-tile control simulation*, which is because its exposure is set to zero (Table 9), preventing redistribution of snow (Eq. 29). However, the ROS-events occurring in all of the simulated snow seasons, give higher viscosities and compaction rates (Eqs. 18-21) in the *single-tile control simulation*, resulting in a small difference in snow depth. On the ridge tile, no lasting snow cover establishes in any of the years. Rather, it is subject to repeated accumulation and subsequent erosion of a thin snow cover, typically between 0 and 15 cm. On the other hand, a substantial snow cover builds up in the snowbed tile, which persists for roughly a month longer than on the ridge for the simulated snow seasons. This is in agreement with Aalstad et al. (2018, 2020), who present satellite derived melt-out curves for the Bayelva area.

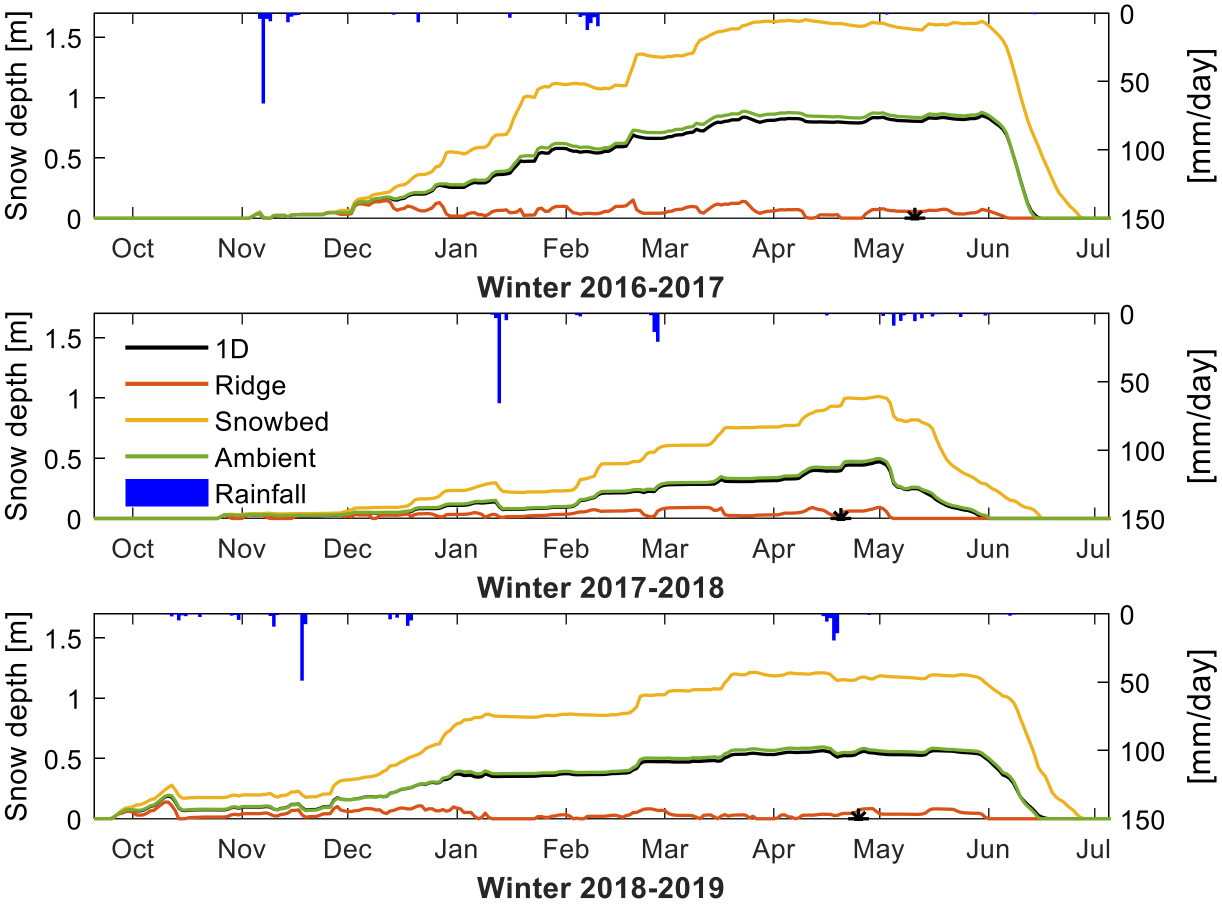

Figure 14: Modelled daily snow depth evolution (left axis) and ROS-events (right axis), revealing differences in duration and amount of snow cover for the three simulated winters. The colored lines are from the three-tile simulation, while the black line is from the single-tile control simulation. The black dots indicate the time of the annual snow survey.

In Figure 15, the simulated snow depth and SWE is compared to in-situ observations from the Bayelva area towards the end of the snow season. The shape of the observed distributions differ somewhat, as wind redistribution affects both SWE and snow depth, while lateral water percolation predominantly affects SWE. In general, the simulations are in good agreement with the observations, with the ridge and snowbed tile capturing the end-members on the snow depth and SWE distributions. The simulated snow depth and SWE for the ambient tile, which comprises 60% of the area (Table 9), follows the peak of the observed distributions for all years except 2017.

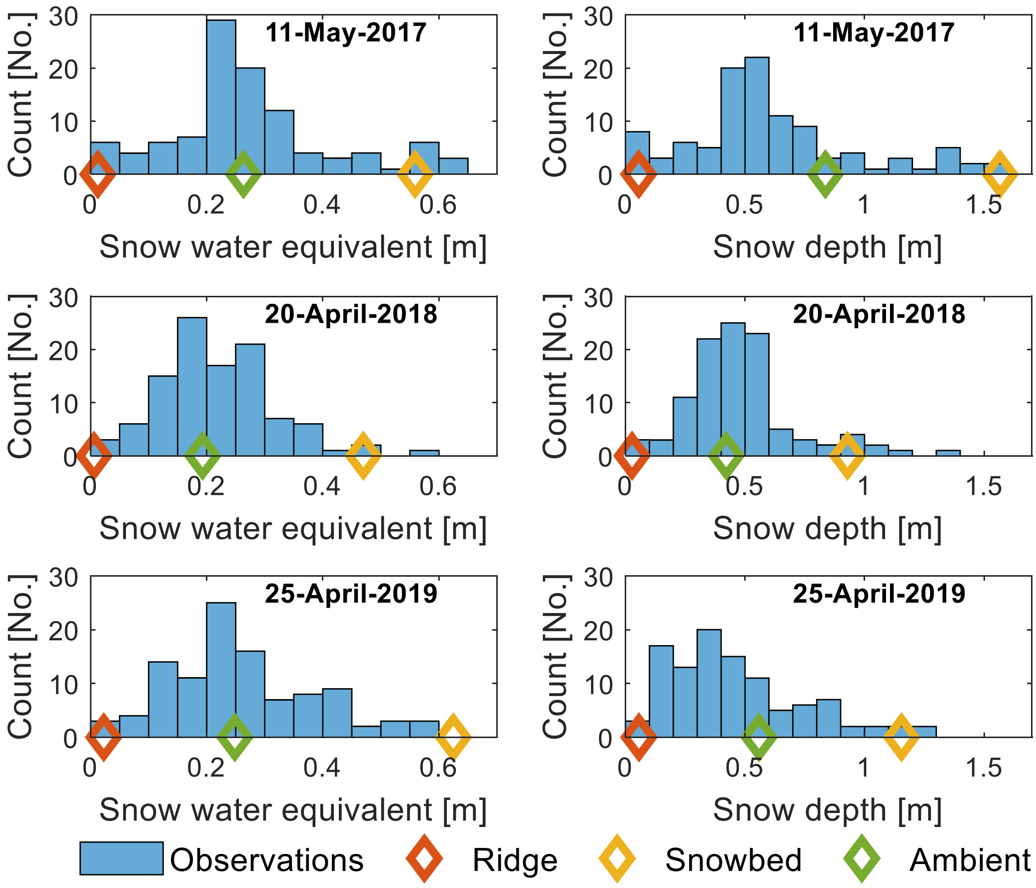

Figure 15: Histograms of observed SWE (left column) and snow depth (right column) for the hydrological years 2017 to 2019, based on 109 (2017 and 2019) and 108 (2018) measurements conducted around the time of peak snow accumulation. The colored diamonds indicate the corresponding values from the three-tile simulation.

4.2.2 Sub-grid evolution of ground surface temperatures

Results from the three-tile simulation are compared to transient in-situ records of GSTs from the Bayelva area for the hydrological years 2017, 2018 and 2019. At any date during this period, at least 90 of the randomly distributed loggers provide valid measurements, and these are aggregated into quantiles describing the spatial distribution of GSTs. From the simulations, the temperature for a depth of 2.5 cm below the soil surface is extracted, corresponding to the typical depth of the GST measurements. Figure 16 show how the simulated and observed temporal evolution of GSTs largely agree. The three-tile simulation is able to capture how the spread in GSTs is small during summer and early fall, and during ROS-events. In winter and early spring, the spread in GSTs is largest, and during this time the snowbed and ridge tile exhibit similar temperature evolutions as the maximum and minimum of the observed distribution. The three-tile simulation captures the spatial variability in melt out dates, which are indicated by the transition to positive GST values. Note that during spring melt, the ridge tile yields the highest GSTs while the snowbed tile represents the lowest GSTs, which is the inverse behavior than during winter.

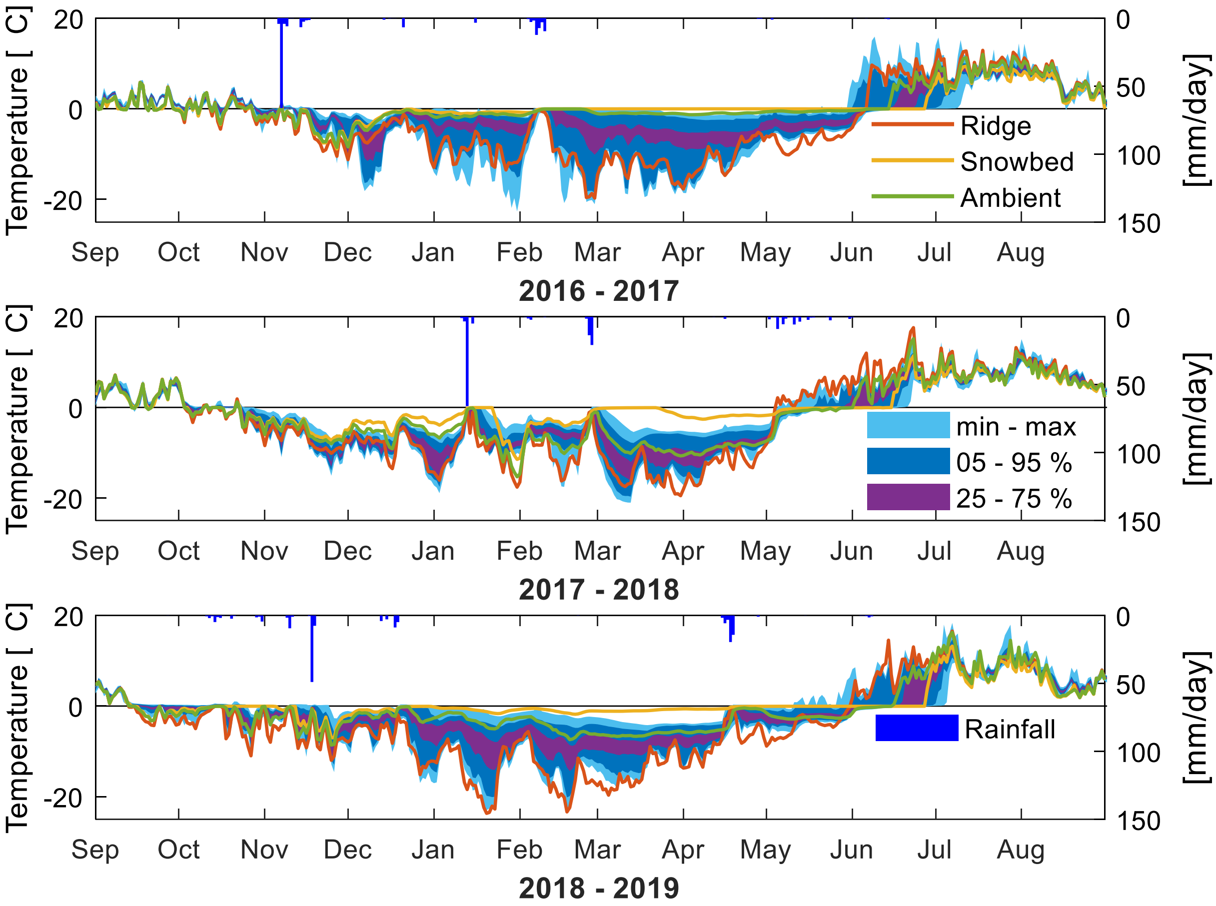

Figure 16: Simulated and observed GSTs for the hydrological years 2017 to 2019 (left axis), and ROS-events (right axis). The lines show the simulated daily GSTs, while colored areas respectively delineate the 25-75 and 5-95 quantiles, as well as the minima and maxima of observed daily average GSTs.

During the three simulated years, the GSTs in the ambient tile are somewhat above the center of the observed distribution. This is especially prominent after a mid-winter ROS-event in 2017, where the simulated GSTs of both the snowbed and ambient tile stay elevated compared to the observations until spring melt. During this period, there is likely a too thick snow cover in the simulations, which triggers a substantially different response to the ROS-event in the first week of February. The Ny-Ålesund observational site (MET.no, 2020) records total precipitation for January comparable to the output from AROME-Arctic (71 and 82 mm, respectively). However, the Ny-Ålesund record shows no net increase in snow depth during this period, while the ambient and snowbed tile experience an increase of 34 and 56 cm, respectively. Note also that the snow depth towards the end of the season for the ambient tile is above the observed peak for 2017 (Figure 15). Consequently liquid water persists below the snow cover in the simulations of the ambient and snowbed tile, in response to the ROS-event, whereas the station record from Ny-Ålesund shows a complete melting of the snow cover.

To elaborate further on the ability of the three-tile simulations to capture the spatial variability in daily GSTs, a systematic comparison of their spread is presented in Figure 17. This shows that the three-tile simulation reproduces the observed spread for the large majority of days. The simulation on average underestimates the spread for days with large spatial differences in GST (≥ 15°C), but this is only the case on a small fraction of days.

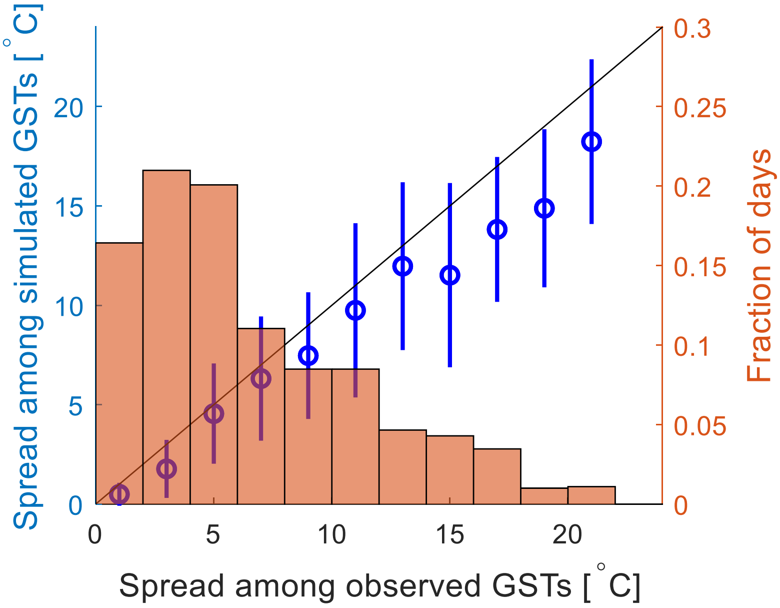

Figure 17: Simulated vs. observed spread (difference between highest and lowest temperature) of 1096 daily GSTs for bins of 2°C (left axis). The error bars indicate the standard deviation of the simulated values within a bin. The 1:1 line is indicated in black. Histogram: Fraction of days with observed spread in each bin (right axis).

The increased explanatory power of the tiling approach is evident when comparing the results to those from the *single-tile control simulation* (Table 16). The observed temporal averages of GST vary on the magnitude of several degrees within the study area, which is generally well captured by the three-tile simulation. The *single-tile control simulation* only delivers one value, which results in substantial under- and overestimation of the extremes of the GST distribution. This is especially important for the warm end of the distribution, as localized persistent positive values could indicate the onset of permafrost degradation. The three-tile simulation captures this, but the *single-tile control simulation* suggests warm, but thermally stable permafrost (Table 16).

Observations		Simulations, three-tile			Simulations, single-tile	
Quantile	average GST	tile	average GST	difference	average GST	difference
5%	-3.90 °C	Ridge	-3.23 °C	-0.67 °C	-0.87 °C	-3.03 °C
50%	-1.56 °C	Ambient	-0.51 °C	-1.05 °C		-0.69 °C
95%	0.63 °C	Snowbed	0.49 °C	0.14 °C		1.50 °C

Table 16: Comparison of simulated (three-tile and single-tile control simulations) and observed average GST for the entire study period (2017-2019) for selected quantiles of the observed distribution.

A comparison of simulated and observed mean annual ground surface temperature (MAGST), freezing degree-days (FDD) and thawing degree-days (TDD) is shown in Figure 18. The three-tile simulation is largely able to reproduce the annual spatial range, and year-to-year variations of these metrics. During all winters, but most notably in 2017, the ambient tile is warmer than the average of the measured distribution. The spread in summer temperatures is small (Figure 16), and TDDs are primarily controlled by the timing of the melt-out in spring, which is represented in the three-tile simulation.

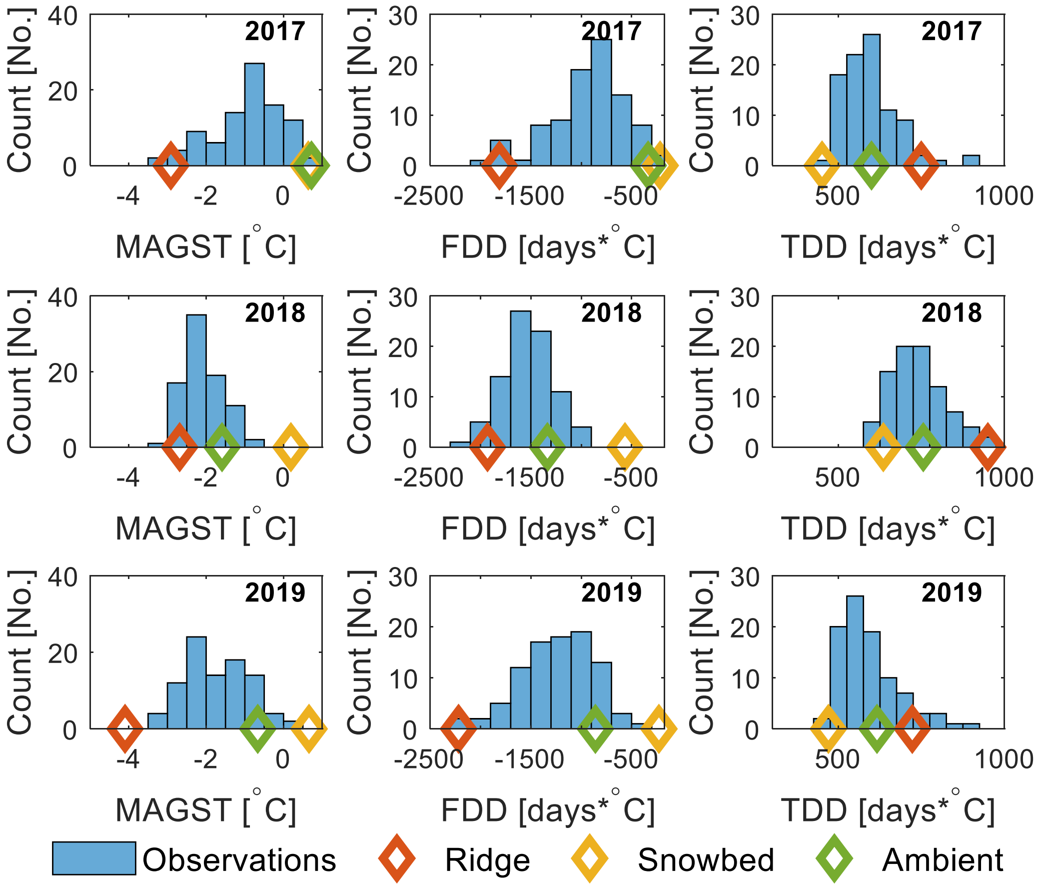

Figure 18: Results from the three-tile simulation (colored diamonds) and histograms of observed MAGST, FDD and TDD for the hydrological years 2017 to 2019. Only observations from loggers which provide valid measurements for at least 360 days of each of the year are included, yielding 92 GST loggers in 2017, 85 in 2018 and 92 in 2019.

4.2.3 Sensitivity of CG Crocus to drift factor

The key to capture the spatial variability in ground thermal regime is the inclusion of local snow redistribution, which in *CG Crocus* is controlled by the drift factor (N_{drift}). Thus, it is of relevance to investigate how it affects the efficiency of snow erosion, and to assess the sensitivity of the model output to the value of N_{drift}. The erosion rates for snow are also dependent on the microphysical snow properties and the wind speed, so a representative selection of these are chosen. The snow types are: 1. Fresh snow deposited during calm weather, 2. Fresh snow deposited during windy conditions, 3. A developed layer of wind packed snow, and 4. A melt crust. The properties of these snow layers are provided in Table 16, while the selected wind speeds are 8 and 15 m/s.

Property	Unit	1. Fresh calm	2. Fresh windy	3. Wind packed	4. Melt crust
Density (ρ)	kg/m^3	100	180	300	500
Dendricity (d)	-	1	0.2	0	0
Sphericity (s)	-	0.5	0.9	1	1
Grain size (g_s)	mm	-	-	0.5	10

Table 17: Properties of typical snow types. As snow type 1 and 2 are dendritic (d > 0), no grain size needs to be assigned to derive the mobility index.

The mobility index is derived for each snow type based on the microphysical properties (Eq. 23), which allows calculation of the driftability index, S_I, for the different wind speeds (Eq. 24). Equation 24 is also used to derive the threshold wind speed required for wind drifting to occur for the selected snow types (Table 18). For the surface layer the depth z_i in Eq. 27 is zero, and for positive driftability indices, this equation reduces to:

$$\theta_{mobile} = \frac{S_I * N_{drift}}{\tau} * \Delta t_{lat}$$

(Eq. 34)

where τ is an empirical constants set to 48 hours (Table 13). As a SWE threshold of 0.01m governs the size of snow layers, ϑ_{mobile} can be used to derive typical erosional rates for surface layers of the selected snow types under specific wind conditions. These are potential erosion rates which only occur for the most exposed tile in the lateral configuration.

	Unit	1. Fresh calm	2. Fresh windy	3. Wind packed	4. Melt crust
Threshold wind speed	m/s	3.3	4.9	6.0	No erosion*
Erosional rates:					
N_{drift} = 2.5; 8 m/s	mm/hr	3.71	1.27	0.47	No erosion
N_{drift} = 2.5; 15 m/s	mm/hr	7.10	3.16	1.61	No erosion
N_{drift} = 5; 8 m/s	mm/hr	7.42	2.55	0.95	No erosion
N_{drift} = 5; 15 m/s	mm/hr	14.2	6.32	3.21	No erosion
N_{drift} = 10; 8 m/s	mm/hr	14.9	5.09	1.90	No erosion
N_{drift} = 10; 15 m/s	mm/hr	28.4	12.6	6.42	No erosion

Table 18: Example of wind erosion for the different snow types for selected wind speeds and drift factors. The melt crust is not erodable for wind speeds under 50 m/s.*

Table 18 shows how the rate of snow erosion exhibits the expected dependency on snow microstructure and wind speed. Fresh low-density snow is highly transportable at moderate wind speeds, while higher wind speeds are required to move denser, more spherical snow (types 2 and 3). The melt crust (type 4) efficiently inhibits wind erosion.

From Table 18, it is also clear that the choice of N_{drift} has a pronounced effect on the erosion rates of the snow layers. To elaborate on the impact this has on the ground thermal regime, the three-tile simulation for the Bayelva area is compared to two complementary simulations featuring a halving and a doubling of the drift factors to 2.5 and 10, respectively (Figure 19). The drift factor primarily controls the efficiency at which snow is transported from the tiles that have a positive snow exchange index to those having a negative snow exchange index (Eq. 29). In the three-tile simulation, this entails that only the ridge and snowbed tiles are subject to wind redistribution of snow, and the ambient tile is only indirectly affected by changes in N_{drift}. For the case where the drift factor is increased to 10, the tiles MAGSTs are negligibly influenced, as the availability of erodable snow is already the limiting factor on snow exchange for N_{drift} = 5. Reducing N_{drift} to 2.5 has a more pronounced impact, increasing (decreasing) the MAGST of the ridge (snowbed) tile by up to 1°C (0.5°C) for sole years (Figure 19). The choice of a drift factor equal to 5 is thus suitable for sites where wind induces snow redistribution is a prominent feature of the snow climate, as is the case on Svalbard.

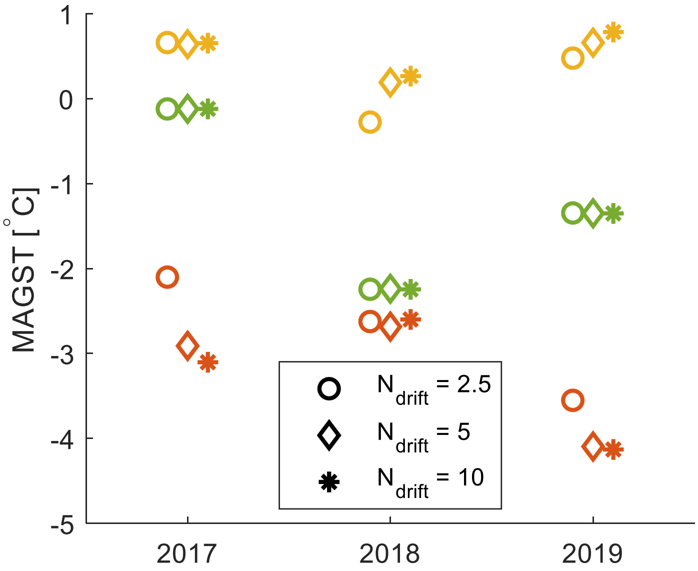

Figure 19: MAGST for the three tiles (Red – Ridge; Yellow – Snowbed; Green – Ambient) for the years covered by the simulations, for different choices of drift factor.

4.3 Further results – exploring applications

4.3.1 Elevation gradients, Nordenskiöld land

For the Nordenskiöld site, the ability of *CG Crocus* to reproduce GSTs across gradients of elevation and maritime influence is evaluated. As four temperature records are available for each topographic setting, the daily average minimum and maximum GST can be derived. Figure 20 and Figure 21 show how the simulated and observed GSTs compare, for Coles Bay and Gangdalen, respectively. While temperatures on the ridge are well captured, the simulations grossly overestimate the temperatures at the subridge. Indeed, the subridge tiles are subject to substantial snow accumulation during drift events, and exhibit a similar temperature evolution as the snowbed tile in the three-tile simulation for Bayelva (Figure 16). This, combined with the realistic temperature evolution in the ridge tile, indicates that the assumption of snow being conserved within the ridge - subridge setup is not valid. To successfully apply *CG Crocus* for new landscapes, it is necessary with basic knowledge of the range of topographic elements amongst which snow is exchanged.

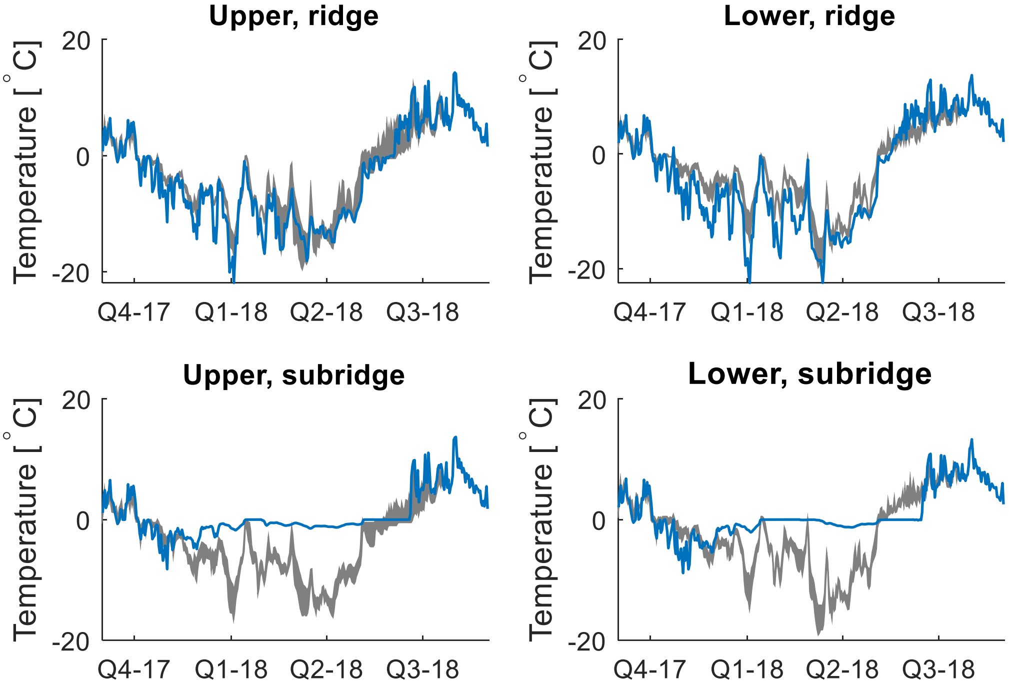

Figure 20: Simulated daily GSTs (blue line) and observed daily average GST spread (gray-shaded area) in the Coles Bay subarea for the hydrological year 2018. Note that the observed temperatures end in mid-summer due to limitations in storage capacity.

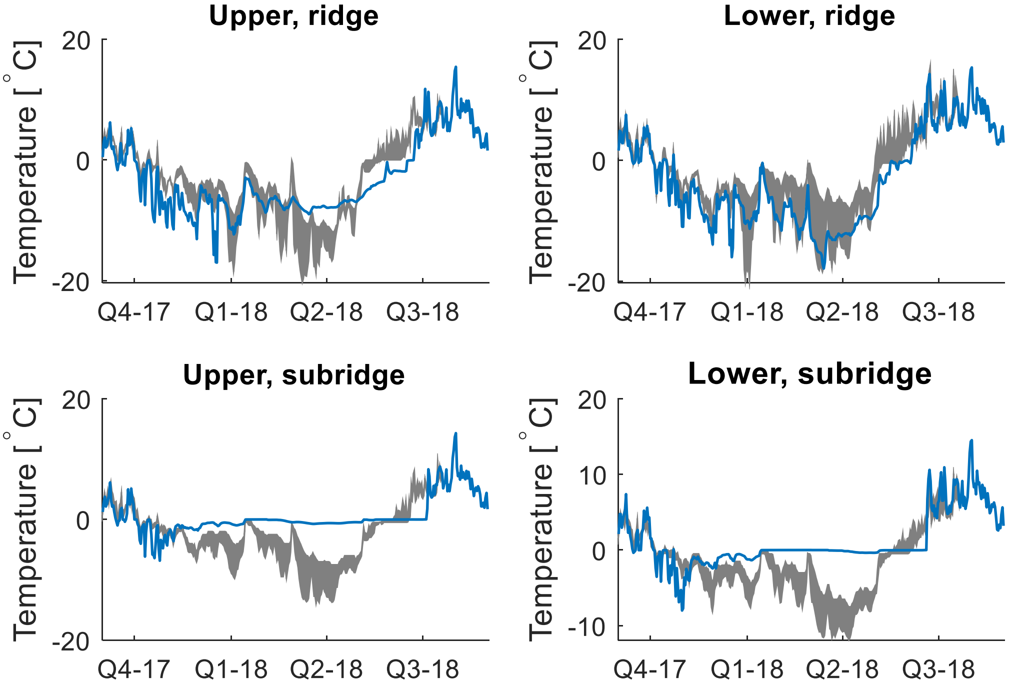

Figure 21: Simulated daily GSTs (blue line) and observed daily average GST spread (gray-shaded area) in the Gangdalen subarea for the hydrological year 2018. Note that the observed temperatures end in mid-summer due to limitations in storage capacity.

4.3.2 Observed landforms: Nunataqs

Here, *CG Crocus'* ability to represent snow redistribution on the km scale is assessed. Figure 22 shows snow depths from a singe-tile simulation of Garwoodtoppen as well as from a two-tile simulation of Garwoodtoppen and Kronebreen. In the single-tile simulation, ca. 2 meters of snow accumulate over the winter, and the snow cover is only interrupted for a short time span in late summer. Indeed, the single-tile simulation indicates that no net accumulation of snow occurs, though its elevation (669 m a.s.l.) is above the ELA of the area. Recent modelling approaches indicate that the ELA of the area is increasing (Pramanik et al., 2018), but the simulation is still above the most recent estimate of the ELA (517 ± 74 m a.s.l.; 2010-2016). However, the elevation where snow survives summer (the *snowline*), should not be confused with the ELA. Hagen et al. (2003) state that the snowline on Svalbard is located higher than the ELA due to internal refreezing and the formation of superimposed ice. The former is accounted for in *CG Crocus*, but the latter can form due to lateral input of water, which is not included in single-time simulations in *CG Crocus*.

Compared to the single-tile simulation, the snow cover on Garwoodtoppen is substantially thinner in the two-tile simulation (Figure 22). As soon as a snow cover establishes itself on Kronebreen in fall, snow can drift among the tiles, which keeps a thick snow cover from establishing on Garwoodtoppen, while at least 1 m of snow accumulates on Kronebreen each winter. Still, Garwoodtoppen is snow-free for a shorter period during summer than Kronebreen, which reflects their elevation difference of 450 m.

As a way to qualitatively assess the performance of the two simulations (1D and tiled) of Garwoodtoppen, melt dates are estimated from satellite imagery. For this the L1C natural color product of Sentinel-2 (ESA, 2015), which consists of orthorectified measurements of top of atmosphere reflectance, is evaluated. As the snow cover diminished gradually, and frequent cloud cover gives substantial gaps in data coverage, a “melt-out period” is defined for each year. This period stretches from the last scene where Garwoodtoppen has a well-connected snow covered, until the first scene where only individual snow patches are present, see Figure 23. It is evident that the tiled simulation better captures the timing of melt out in all years. However, there are small snow patches that persist substantially longer, sometimes even until the first snowfall.

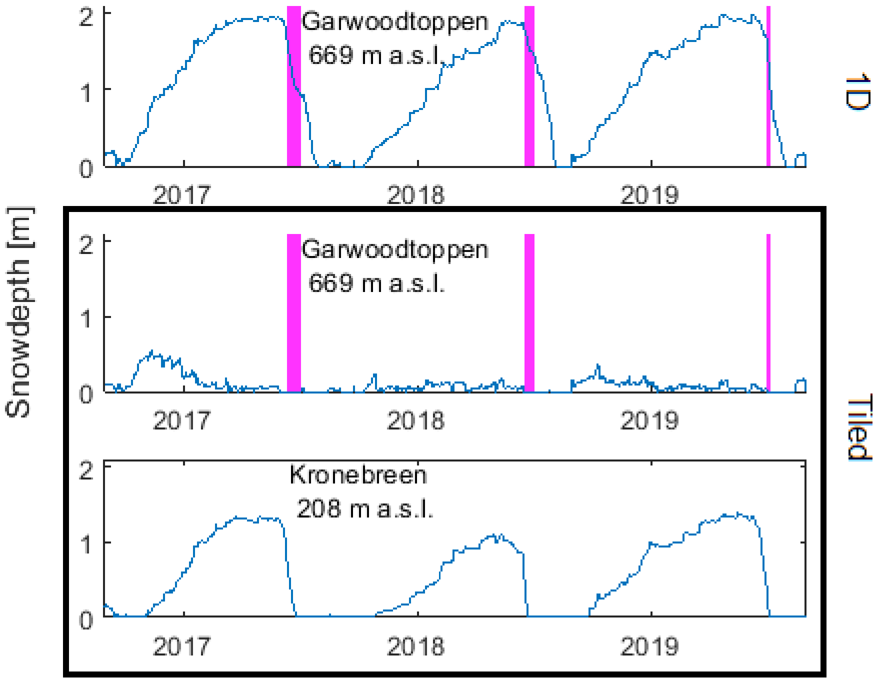

Figure 22: Simulated snow depth evolution for the last three snow seasons. The top pane show the results from a single-tile simulation of Garwoodtoppen, while the two lower panes show the results of a two- tile simulation of Garwoodtoppen and the neighboring Kronebreen. The pink shading shows the period within most of Garwoodtoppen is observed to melt out, see example for 2019 in Figure 23.

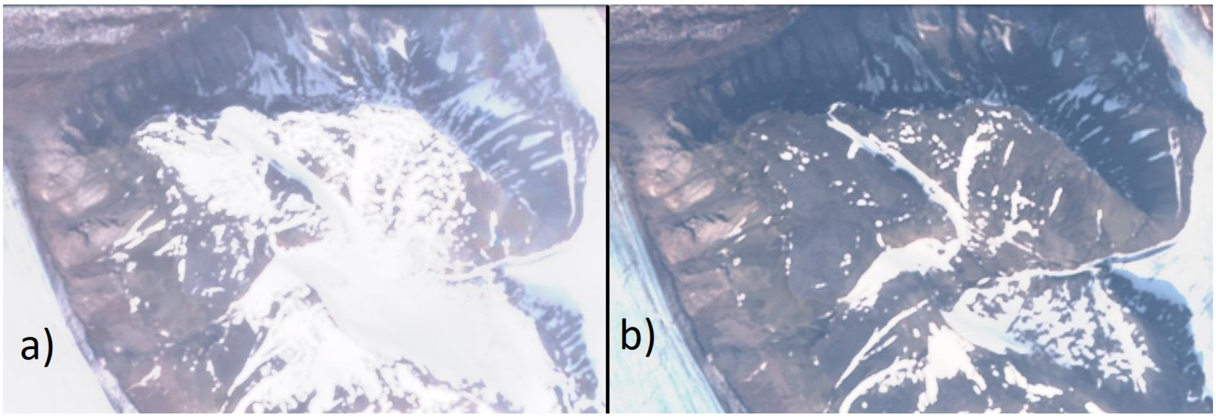

Figure 23: Example scenes from Sentinel-2, showing (a) that Garwoodtoppen is mostly snow covered on 1.6.2019, while (b) the ground surface is mostly bare on 7.6.2019.

4.3.3 Observed landforms: Palsa mire

The ability of *CG Crocus* to reproduce the thermal regime of palsa mires is evaluated at the Suossjavri site. Figure 24 shows the temperature and snow depth evolution of the *palsa* and the *mire.* Snow depths are thin on the *palsa*, allowing the ground to be cooled during winter. During summer, water drains from the *palsa*, efficiently insulating the frozen subsurface soil layers from the high air temperatures. The opposite is the case for the mire; it is insulated from the cold air by the snow in winter, and experiencing efficient heat conduction through wet surface layers in summer. Both tiles were initialized with a zero-degree temperature profile in November 2011, but the stark contrast in thermal dynamics allows for permafrost to form quickly in the *palsa*. The AL in the *palsa* is simulated to be around 70 cm in September, which is at the upper end of the reported depths for Suossjavri (Aas et al., 2019; Martin et al., 2019). The simulated snow depths on the *palsa* are between 5 and 25 cm in late winter, which is in agreement with reported observations. Note that the wind speeds in this simulation are artificially raised, and that transient records of wind and snow depth would be required to evaluate if this is realistic.

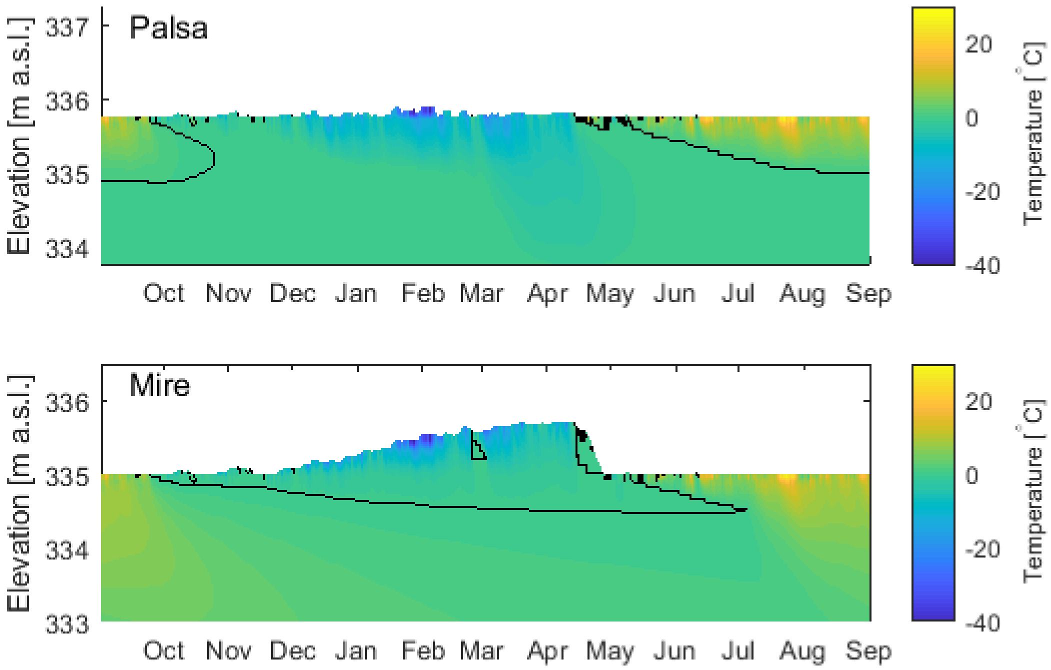

Figure 24: Temperatures for the palsa (top pane) and the mire (lower pane) for the hydrological year 2019. The black line indicates the zero-degree isotherm.

5 Discussion

This chapter contains discussion of *CG Crocus'* newly included capabilities, including the new *crocus snow scheme* (Sect. 5.1), and the lateral exchange processes (Sect. 5.2). In Section 5.3 the limitations in model physics and input data are addressed. Section 5.4 presents future processes which future improvement should target, and discusses potential applications of *CG Crocus*.

5.1 Representation of snow processes in CG Crocus

The dynamic buildup and evolution of snow cover and snow properties in *CG Crocus* is realized by improving the *simple snow scheme* with parameterizations from the CROCUS snow microphysics scheme. The rationale behind this is that a more detailed description of the snow cover will enhance *CG Crocus'* ability to simulate the ground thermal regime. CROCUS has proven to perform well under a wide range of climatic conditions (e.g. Brun et al., 2013), which suggests that the applicability of *CG Crocus* should not be restrained geographically. However, CROCUS is primarily developed as a tool for avalanche forecasting in mid-latitude Alpine regions (Vionnet et al., 2012), and necessarily does not resolve the relevant processes for a permafrost modelling at in high latitudes at an appropriate detail or scale.

The SEB parameterizations from CROCUS include dependencies on grain characteristics, as well as empirical relationships to age and altitude (Table 5). While the former reflects how snow microstructure affects radiative transfer, the latter two are used to estimate the impact of light absorbing impurities (Vionnet et al., 2012). The use of snow age as a proxy for dust concentration is also known from other snow schemes, including the *simple snow scheme* (ECMWF, 2007; Westermann et al., 2016), while the elevation dependency is a parameter strictly tuned to the validation site of CROCUS in the French Alps. In reality, the deposition of light absorbing impurities is variable both geographically and temporally, depending on both dust sources and meteorological conditions. In Ny-Ålesund and Svalbard, local and regional sources for both natural and anthropogenic dust are identified (Moroni et al., 2018), and these likely differ from the sources in the French alps. An explicit scheme for the accumulation of light absorbing impurities would be required to allow for geographical differences in dust deposition. Actually, Lafaysse et al. (2017) implemented parameterizations in CROCUS where a dry deposition term is used to calculate the amount of light absorbing impurities for each snow layer. In theory, field observations of dust concentrations in the air and snow column could be used derive regional parameters for this parameterization.

Heat transport through snow occurs in a number of modes, including conduction through air and ice, convection, water vapor transport and radiation. Explicit representation of all of these energy fluxes is not possible for most snow schemes, and simplifications are made. Both CROCUS and CryoGrid use the formulation by Yen (1981) (Eq. 9) to express heat transport by an effective thermal conductivity of snow, k^*_{snow}. In *CG Crocus*, this parameterization is further improved to include a temperature dependency (Eq. 10). Several, more recent density-dependent regression formulas capturing the first-order behavior of k^*_{snow} have been published, e.g. Sturm et al. (1997) and Calonne et al. (2011) (Figure 25). However, there is substantial scatter of observed thermal conductivities around these curves, which is linked to the microstructure of snow (Calonne et al., 2011). While this is still a topic subject to current research (e.g. Calonne et al., 2019), parameterizations of k^*_{snow} taking into account the anisotropy of snow might soon be feasible. As CROCUS' description of snow properties already includes relevant parameters defining grain characteristics (d, s and g_s), implementation of a heat transport scheme based on snow microstructure should be readily implementable.

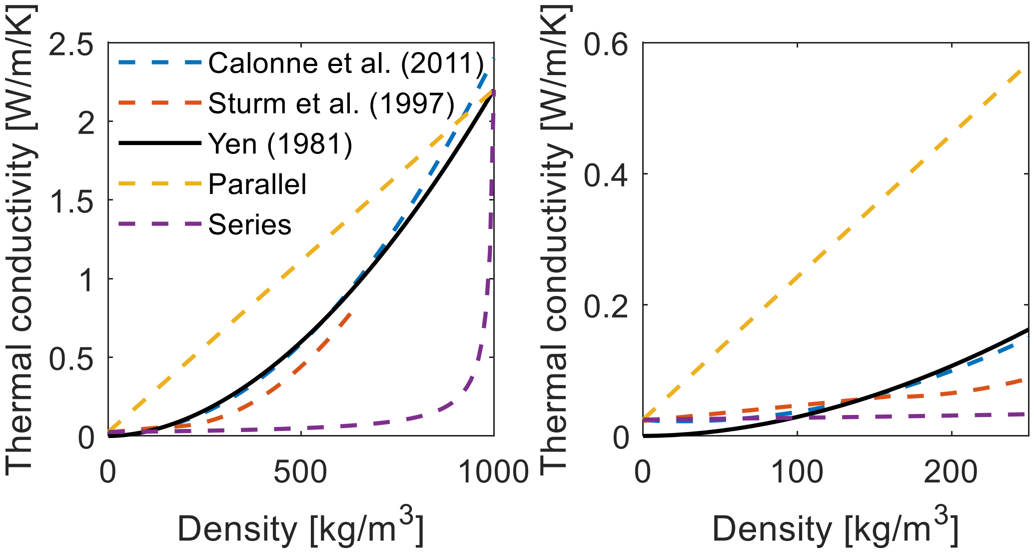

Figure 25: Different parameterizations of the effective thermal conductivity of a matrix of ice and air (both at 0 °C), as a function of its density. "Parallel" and "series" indicate the physical limits on conduction through a mixture of ice and air. "Parallel" assumes each material is well connected and that conduction through them occurs in parallel, while "series" assumes they are layered and that conduction is limited to occur sequential. Sturm et al. (1997) state their formula to be valid only for densities below 600kg/m^3.

The presence of liquid water within the snowpack is essential to processes such as metamorphism, latent heat exchange, and compaction, but is only rudimentary represented in *CG Crocus*. Water percolates according to a bucket scheme, and the retention capacity of each snow layer is given by Pahaut (1976), i.e. linearly decreasing with snow density. More recent parameterizations include Coléou & Lesaffre (1998), who propose a similar, but substantially higher density-depended water-holding capacity, and Boone (2002), who present an inverse relationship between retention capacity and snow density. This spread in parameterizations reflects the difficulties in measuring the water content and retention capacity of snow (Lafaysse et al., 2017). Further, bucket schemes are limited in their representation of how variations in snow permeability give rise to internal ice layers and preferential flow paths. A more physically correct way to simulate water percolation would be to solve the Richards equation, which includes the effects of capillary suction and saturation on snows hydraulic conductivity (e.g. Wever et al., 2014, 2015). Indeed, the Richards equation has recently been tested for CROCUS (D'amboise et al., 2017), yielding higher water contents than with the original bucket scheme. While the results were promising, there is a feedback of increased water content on the empirical metamorphism and compaction relationships of CROCUS (Table 7), which gives a misrepresentation of snow microstructure for wet snow (D'amboise et al., 2017).

5.2 Representation of spatial variability in CG Crocus

CG Crocus in tiled configurations enables a process-based representation of local variations of snow depth, basal ice layers and GSTs, which cannot be achieved by one-dimensional schemes. Terrain induced spatial variability is simulated by segmenting the landscape into idealized terrain units, amongst which lateral fluxes of snow and water occur. This allows for a transient representation of the sub-grid variability of snow and wetness. For the Bayelva area, the landscape is simplified to a ridge-depression-plain system, which yields valuable information about the local distribution of snow depths compared to the single-tile control simulation (Figure 14). It is noteworthy that the three-tile simulation produces realistic estimates of the end-members of the observed snow depth and SWE distribution (Figure 15). This simple three-tile setup is also able to capture the spatial variability in GSTs at the Bayelva area, with small spread in summer and greater spread in late winter (Figure 16 and Figure 17). In particular, the ability to simulate how the preceding snow cover dictates the local GST evolution following ROS-events is of relevance.

The parameterization of lateral snow fluxes in *CG Crocus* prescribe wind redistribution in a rudimentary way. The flux of removed snow is assumed to be inversely proportional to the *time characteristic for snow grains undergoing wind induced density and grain change* (Eq. 25). This relationship is not confirmed by field or laboratory experiments. The drifting snow is then distributed from tiles with higher exposure to those with a lower exposure, which gives a leveling of the exposures in the simulated domain. The distribution of snow among the tiles is thus ultimately defined by the choice of exposures. Further, the calculation of snow exchange as bulk lateral snow fluxes disregards the different modes of snow transport (creep, saltation and turbulent suspension), and how transport distance and efficiency varies among these modes is not accounted for. However, the presented parameterizations allow snow fluxes to be derived in a physically-based fashion in qualitative agreement with Vionnet et al. (2012), and reproduce the observed smoothing of local topography.

In the three-tile simulations, the Bayelva area is divided into three landscape units, which cannot represent the true spatial variability of the area. Most notably, the exposure e_{init} of each tile is set equal to its relative elevation, which assumes that both the transport of water and snow occur solely from higher to lower elevations. This entails that the snowbed tile is both the received of snow and water, which is in agreement with observations of large snow and thick basal ice layers in topographical depressions. On the other hand, large snow depths are also observed on the lee-side of slopes, which cannot be simulated using this altitude-dependent exposure formulation, and this has consequences for the ability to reproduce a realistic response to ROS-events. E.g. during events where lateral percolation of water within the snowpack occurs, a snowbed located on a lee-side will experience a throughput of water, while water will accumulate within a snowpack located in a depression. As latent heat is released by freezing water, a snowbed in a topographical depression will be subject to a prolonged zero-degree curtain effect compared to a snowbed on a lee-side. This could partly explain why the snowbed tile experiences GSTs above the observed maxima of GSTs following pronounced ROS events (Figure 16).

There are clear shortcomings in the application of *CG Crocus* for the different terrain configurations in Nordenskiöld land (Figure 20 and Figure 21). Observations and simulations agree that the ridge is coldest, and experiences the greatest variability in wintertime GSTs. However, the simulated GSTs of around zero degrees during winter are not observed in the subridge. Though the ridge is more exposed than the subridge, the observed GSTs indicate that neither of them likely experience substantial snow cover, and that they both loose snow to the surroundings. This is evidence of a clear mismatch between the simulated domain, and the terrain features amongst which snow redistribution occurs in reality. In *CG Crocus*, the mass of snow is conserved among the simulated tiles, and if these do not represent the full spectrum of locations experiencing snow erosion and deposition, erroneous results are inevitable. Landscapes adjacent to open water or steeps cliffs would experience similar issue, as they also “loose” snow from the system. For the Bayelva area, the ability of the three-tile simulations to capture the end-of-season snow distribution (Figure 15), indicate that the net snow exchange with the surroundings averaged over each snow season is negligible for this area. However, this might not be the case for single drift events, which might be a contributing factor to the previously described discrepancies between simulated and observed snow depths in January 2017. An approach to simulate loss of snow from the system could be to include a “ghost” tile, which is assigned a negative exposure and whose sole purpose is to remove snow. A ghost tile would have similar function as the Kronebreen tile in the simulation of Garwoodtoppen, but would not have to be explicitly simulated. However, whether snow is lost from the system also depends on wind direction. For Garwoodtoppen, it is reasonable to assume that winds from the east, south and west would relocate snow to the lower lying glaciers (i.e. remove it from the system), while winds from the north would feed the ice patches and snowbeds south of the peak (Figure 7). It would be interesting if these features could be captured by adding a tile for this area (ca. 500 m a.s.l.), onto which drifting snow during northerly wind is redistributed. Actually, a tributary to the glacier Fatumbreen was located in this area in 1936 (Figure 26), and such a setup could be used to study which climatic conditions are required to form and sustain this perennial ice mass.

Figure 26: Oblique aerial photography of Garwoodtoppen in the summer of 1936, showing that a tributary glacier is located south of the peak. The image is taken from the SW at 3000 m altitude (ID: S36_0811), courtesy of the Norwegian Polar Institute (npolar.no).

The sub-grid snow distribution in *CG Crocus* could be resolved more accurately by simulating the lateral processes on a meter-scale three-dimensional grid. For the Bayelva area, this would entail drastically increasing the number of tiles to ensure that the end-members of the distribution are included. Further, such approaches already exist (e.g. ALPINE3D; Lehning et al., 2006), but the computational expense is great, and applications over large areas are challenging. In *CG Crocus*, the computational expense is only increased by a factor roughly equal to the number of tiles, compared to one-dimensional simulations. On the other hand, gridded simulations including snow redistribution have successfully been applied over large areas and time series using SnowModel (Liston & Elder, 2006). However, the snow transport in SnowModel is calculated purely based on the meteorological data and vegetation parameters (Liston & Sturm, 1998), disregarding the spatiotemporal variability of snow erodability (i.e. fresh powder and dense wind packed snow would be eroded with the same efficiency).

The physical representation of erodability and its effects on the transient evolution of sub-grid snow distribution distinguishes *CG Crocus*. Previous attempts to account for the effects of sub-grid snow variability require knowledge of the snow distribution as input (e.g. Gisnås et al., 2014), or use a predefined distribution function to scale snowfall (e.g. Aas et al., 2017; Obu et al., 2019). Such statistical approaches are often based on the end-of-season snow distribution, and are subject to an underlying assumption that this distribution does not change over the course of the snow season. In reality, the snow distribution evolves through the aggregate of events of snowfall and wind drift. This is included in *CG Crocus*, where snowfall is added equally to all tiles, and redistributed when the combination of meteorological conditions and snow microstructure permit drifting. Instead of requiring knowledge of the snow distribution, *CG Crocus* produces realistic estimates of the end-of-season snow distribution based on forcing and topography.

The representation of lateral water exchange in *CG Crocus* includes some shortcomings. Water fluxes only occur between adjacent tiles which both feature the same surface cover (ground or snow), and not among snow-covered and snow-free tiles. In spring, the snow cover necessarily disappears first at the most exposed tile, and water pools up within its soil column until its neighbor(s) melt out. For the simulations of the Bayelva area, this means that the ridge tile does not drain during the roughly one month in melt out difference between it and the snowbed tile. However, this does not seem to have a strong effect on the near-surface thermal regime, as the ridge tile still captures earliest positive GSTs for most years (Figure 16). The remaining difference in early summer GSTs is likely a trait of the assumption of flat and horizontal surfaces for all simulated tiles, while the true terrain exhibits variations in slope and aspect. While the three-tile simulation of Bayelva accounts for the primary processes defining sub-grid snow and GST distribution, representation of variations in surface roughness and exposition is not feasible, as it would entail drastically increasing the number of simulated tiles.

The parameterization of snow erosion in *CG Crocus* rely on an empirical drift factor, N_{drift}, to derive erosional rates from the original CROCUS parameterizations. For the presented simulations spanning the Norwegian Arctic, N_{drift} has been set to 5 to reproduce observed spatial variations in snow depth. This value is purely empirical, but in principle, it could be determined by field or laboratory experiments relating observations of wind speed and snow erosion to preceding surveys of snow properties. While the sensitivity study (Sect. 4.2.3) shows that N_{drift} has a strong control on instantaneous erosional rates, the snow distribution in Bayelva is ultimately controlled by the amount of snow that is driftable. Consequently, the impact variations in N_{drift} have on ground thermal regime in Bayelva are limited (Figure 19). For the palsa mire at Suossjavri, *CG Crocus* was not able to reproduce the redistribution of snow from the *palsa* to the *mire*, and the wind speeds were thus artificially increased. An increase in snow erosion could not be achieved by elevating the drift factor, as the amount of driftable snow (S_I; Eq. 24) is the limiting factor. In this situation, shortcomings in the forcing data or parameterization of S_I are likely responsible for the discrepancy.

5.3 Practical limitations

The capability of *CG Crocus* is subject to the quality and representativeness of the data used to derive soil and atmospheric variables. For all the presented simulations, forcing data from the AROME-Arctic NWP model is used, and its uncertainties will inevitably affect performance. The presented setup is especially sensitive to snowfall rates and wind speed, which together control the simulated snow distribution. However, weather prediction in the Arctic is subject to large challenges, amongst other a limited observational network for initialization and validation of models. Indeed, the station network within AROME-Arctic' domain (Figure 3) is densest on the Norwegian mainland, and the previously discussed problems in Suossjavri are surprising. Still, several validation studies have shown that AROME-Arctic performs well in the high latitudes (Køltzow et al., 2019; Müller et al., 2017), and it is unlikely that better updated fields of near surface meteorological variables for Svalbard are currently available. This is supported by the three-tile simulation of Bayelva, which suggest that averaged over the snow season, the precipitation and wind speeds from AROME-Arctic are able to reproduce the observed snow amount and distribution in Bayelva.

Alternative sources of forcing data include observations from weather/climate stations and reanalysis data sets. Hanssen-Bauer et al. (2019) note that the observational station network on Svalbard is strongly biased towards the west coast and low elevations, and thus does not represent the meteorological conditions across the archipelago well. Further, *CG Crocus* requires fields of radiative fluxes, which are not routinely measured at weather stations. For these reasons, station observations are not considered a suitable source of forcing data for this study. However, time series of the required variables are available for Ny-Ålesund/Bayelva area (Boike et al., 2018; Maturilli et al., 2013), and a comparison of *CG Crocus* simulations forced with NWP and observational data would be interesting. Another potential data source for applications in Svalbard is the Sval-IMP dataset (Østby et al., 2017), which provides consistent time series (1957-2014) of spatially distributed meteorological variables. Sval-IMP is a statistical downscaling of the ERA-40 and ERA-Interim reanalysis' to 1km resolution. Regrettably, this dataset does not cover the most recent years, which are of interest for this study. In ERA-40 and ERA-Interim, the station and radio sounding observations from Ny-Ålesund are assimilated into the reanalysis (Østby et al., 2017). This poses an issue for using Sval-IMP to force *CG Crocus*, as the Bayelva area is ca. 3km from Ny-Ålesund, and a good fit here would not necessary be transferable to the rest of Svalbard. Indeed, the same issue might be valid for the AROME-Arctic data, which also assimilates station observations to define the initial model state (Müller et al., 2017). However, the data extracted in this study has a lead time of at least 18 hours (Sect. 3.2.2), and should thus be a product of the physics and topography of AROME-Arctic, rather than the assimilated observations.

For all study sites except Suossjavri, soil properties are roughly based on observations by Boike et al. (2018). These observations come from three soil profiles at different location around the Bayelva site (Figure 27), extending .80 – 1.25 m below the surface. No soil data is available below this depth, and the chosen soil-bedrock interface at 5 m is arbitrary. This might have an impact on the thermal regime at depth, as the thermal conductivity of bedrock (primarily minerals) and soil (mixture of minerals, organics and water) differ. This should however not strongly affect the results in this study, as only temperature data from the surface (ca. 2.5 cm) are evaluated. Further, the AL thickness in this area is between 1 and 2 meters (Boike et al., 2018), so the infiltration depth for water is already limited by the presence of permafrost throughout the area. At the study area in Nordenskiöld land, the measurement locations are chosen to represent reindeer forage localities. This entails that they exhibit some form of vegetation and soil cover, and are not located on i.e. bedrock, block fields or ice fields, and it is thus not unreasonable to assign the soil stratigraphy from Bayelva. For Garwoodtoppen, no soil information is known, but only snow depths are evaluated for this site.

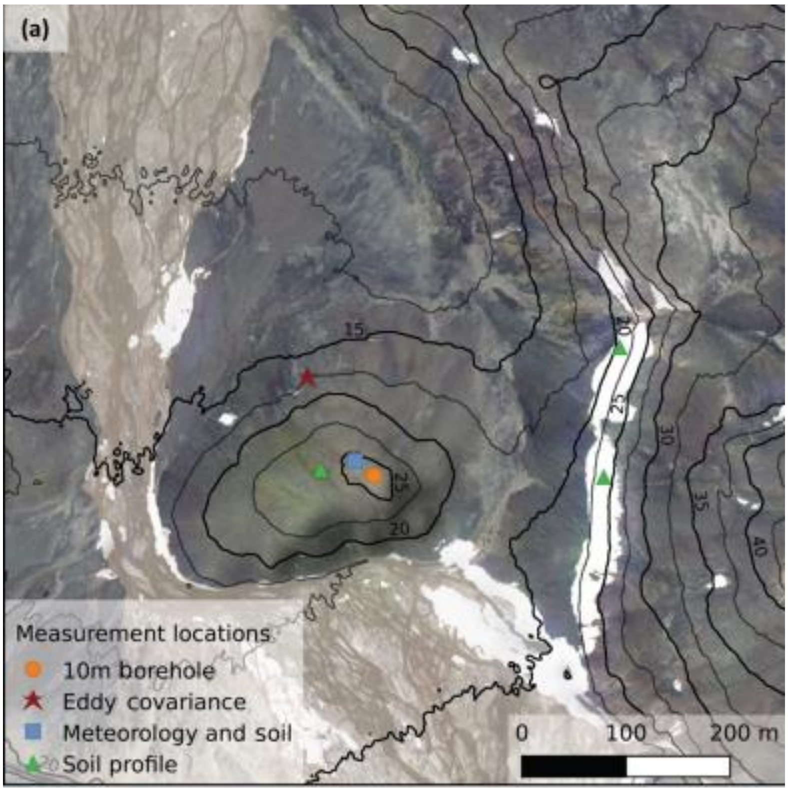

Figure 27: Figure 2a in Boike et al. (2018), showing the location of the soil profiles (green triangles) around the Bayelva high Arctic permafrost research site. North is towards the top of the image.

The choice of surface properties might impact the simulated GSTs in Bayelva and Nordenskiöld land. Boike et al. (2018) mention that the surface cover in the Bayelva area is variable, which is confirmed by field observations in fall 2019. Around half the area is covered with vascular plants or mosses, while the rest consists of mud boils and stones (Boike et al., 2018). Similar surface variability is reported for Nordenskiöld land, with thinner soil and vegetation cover at the ridge compared to the sub-ridge. These differences are not taken into account in the simulation of these areas. Only the ridge tile in the three-tile simulation of Bayelva is assigned no organic layer (Table 11), while all surface characteristics (root-depth, albedo, roughness length etc.) are kept the same (Table 13). However, the simulations do well reproduce the GSTs in summer, when the ground surface is exposed (Figure 16, Figure 20 and Figure 21). The variability of surface properties among the observed locations is thus assumed to have only minor impact on the thermal regime. Currently, a snow cover is only initialized in *CG Crocus* in response to snowfall, which is inadequate to reproduce some specific, observed cases. For example, snow transport only occurs between snow covered tiles, which means that drifting snow cannot be deposited on bare ground. This is generally not an issue if the tiles are assigned the same forcing data, but is evident in the simulations of Garwoodtoppen and Kronebreen (Figure 22).

Further, the range and detail of the included processes also poses a limitation for *CG Crocus*. E.g. the buildup of basal ice through refreezing of rain- and meltwater within the snowpack is included, while aggradation of ice directly on the bare ground surfaces is not. Such ice layers can form in response to freezing rain (rainfall at subzero temperatures) or rainfall onto frozen ground. Peeters et al. (2019) hypothesize that the former might be relevant for coastal sites on Svalbard, while the latter is observed to occur at exposed ridges. Practically, this could be implemented by adding a “snow” layer with the density of ice, with mass corresponding to what could be frozen by elevating the temperature of both ground and rain to the melting point.

Currently, *CG Crocus* does not include a scheme for heat conduction among tiles. Such a scheme was included in the setup of Nitzbon et al. (2019), but was not continued in *CG Crocus* as it was designed for spatial scales where heat conduction is assumed to be negligible. However, the simulations in Suossjavri indicate rapid formation of permafrost in the palsa, which might be slowed by exchange of heat energy with the surrounding mire. Aas et al. (2019) show that heat conduction does play a role in the degradation of palsas for future climate scenarios. Thus, inclusion of lateral exchange of heat energy would likely improve *CG Crocus*’ representation of this site.

The previously discussed conservation of the mass of drifting snow in *CG Crocus* also disregards sublimation of snow during drifting events. Tabler (1994) published curves of fractional sublimation loss for different transport distances of drifting snow, which indicate that half of the drifting snow sublimated over fetches of 3km. While most the sites in this study are well below these distances, this needs to be considered before applying *CG Crocus* on systems with greater transport distances. The exception is Garwoodtoppen, but for this site, the amount of drifting snow deposited on

Kronebreen is not of major relevance. A scheme for simulating sublimation loss during snow drifting, could be by calculating of the trajectories along which snow is redistributed during drift events, and removing snow based on the transport distances following Tabler (1994). This would however be challenging for cases where more than one tile receives or loses snow, as the determination of trajectories then would be arbitrary. Alternatively, sublimation rates of drifting snow could be prescribed following Gordon et al. (2006), which previously has been successfully implemented in CROCUS by Brun et al. (2013). For tiled simulations, this would require the creation of a "drifting snow pool" from which sublimated snow is subtracted.

The lack of explicit treatment of surface water is a limitation in the presented model setup. *CG Crocus* assumes effective drainage of excess water when the soil column is saturated, which inhibits the formation of surface water and overlooks associated effects on ground thermal regime. If surface water is present, it will slow the freezing, which would produce a prolonged zero-degree curtain effect. This likely explains why all tiles in the three-tile simulation of the Bayelva area feature negative temperatures in the period mid-September to mid-October 2018 (Figure 16), while some observations show zero degrees. Surface water could be implemented in the model implicitly by adding excess water to a "reservoir" for each tile, which drains at a constant rate while feeding water back to the surface if this is below saturation. An explicit representation of temporary surface water would require parameterizations on how this affects the SEB, and how it evolves during freezing and drainage. In addition, CG Crocus does not capture how GSTs at some observations are retained close to zero after melt out in spring. These locations are likely experiencing throughput of meltwater from still snow-covered sites, and inclusion of a scheme for lateral advection of heat could amend this.

A more explicit handling of surface water could make *CG Crocus* a useful tool for investigations of how sub-grid variability affects permafrost hydrology. Indeed, Walvoord & Kurylyk (2016) identified the spatial heterogeneity of permafrost landscapes as a limitation for applications of process-based hydrological models. The diagnostically derived hydrographs (Sect. 4.1.2) indicate that the three-tile simulation of Bayelva adds insight into how sub-grid variability affects the hydrology of the area. However, there are still obvious shortcomings. The hydrology of the Bayelva watershed has previously been studied by Nowak & Hodson (2013), who identify intense winter rainfall as a source for runoff outside the summer period. While this is captured for early-winter ROS-events (Figure 13), no runoff is produced in response to the heavy ROS-event in spring 2019 (Figure 12). This is contrary to field observations, which report liquid surface water at low-lying locations in the Bayelva area even a week after the ROS-event. To reproduce this, a scheme detailing lateral seepage of water within the snowpack could be included. Additionally, a similar scheme for seepage from water within the thawed part of the soil column could improve the representation of surface runoff in summer.

5.4 Outlook

A critical point in *CG Crocus* is the selection of landscape units into which the study area is segmented, and the choice of their topographical parameters. Throughout this study this is done manually, and for the smaller sites Bayelva and Suossjavri this has proven successful. However, it can be challenging to manually define the relevant terrain features for study areas with a more complex topography, and an automated routine would be desirable. Further, the configuration of tiles has been two-dimensional for all simulations in this study (assuming translational or rotational symmetry), which might be inadequate for larger or more complex areas. An objective way to determine the model tiles and their topological parameters (see Table 9), would be by applying the clustering techniques presented by Fiddes & Gruber (2012) for both forcing- and topographical data. For larger study areas, this could be used to define a triangular irregular network (TIN), comprising the relevant terrain feature and their relation to another. An advantage of such a TIN approach over regular gridded approaches, is that relevant small features can be captured (e.g. a stream incision), whereas the number of realizations for relatively homogeneous areas is limited. This would allow *CG Crocus* to be run with a greater detail and lower computational expense than regular gridded simulations.

Future improvements of *CG Crocus* should also target the previously discussed issues regarding the formation of snowbeds. The current formulation of the exposure of a tile, *e*, already allows for it to be decoupled from the altitude of the tile, which can be used to enable snowbeds to form on slopes. For the Bayelva area, the snowbed tile could e.g. be divided into two tiles to differentiate the two processes that give accumulation of SWE (lateral water percolation and snow redistribution). This would be in agreement with the snow surveys in spring 2019, where both sites with great snow depths and no basal ice, and sites with ice exceeding the coring equipment (but with no snow) where observed. However, manual selection of exposures for larger areas would be difficult, and development of an automatized procedure would be required. Especially, a formulation of exposure taking into account the wind direction and distance between tiles would be advisable before using *CG Crocus* in a three-dimensional configuration. High-resolution wind fields have previously been used to successfully determine areas of snow erosion and deposition during drift events in steep terrain (Dadic et al., 2010), and preferential deposition during snowfall (Lehning et al., 2008). Indeed, Jaedicke & Sandvik (2002) used a numerical mesoscale wind model to reasonably well simulate snow distribution in central Spitsbergen. The average wind velocity normal to the local surface over the snow season could for example be a suitable metric to define the exposures in *CG Crocus*. Dadic et al. (2010) also note that the areas experiencing increased and decreased deposition during drift events vary according to wind direction. This could be amended by introducing a dependency on wind direction, where exposure values are derived for the dominant or cardinal wind directions over the study area. However, there would still be a need for transient adjustment of the exposure (as in Eq. 28), e.g. to avoid topographical depression continuing receiving snow when their snow surface is level to the surroundings. Calculating the exposures at each timestep from the instantaneous wind field over the current snow surface is likely not feasible, as it is highly computationally demanding (Lehning et al., 2006).

Remotely sensed data of snow cover holds potential to improve the temporal evolution of snow distribution in CG Crocus. A major source for uncertainties in snow modelling is namely how errors in forcing data and model physics propagate as the simulation evolves (Raleigh et al., 2015). An example of this from the three-tile simulations of Bayelva, is how the inconsistency between simulated an observed snow depth around the ROS-event in February 2017 give deviations of GSTs for the rest of the season (Figure 16). A routine that could identify and correct such discrepancies from regularly available satellite products would be desirable. Actually, Aalstad et al. (2018) showed how the end-of-season snow distribution in the Bayelva area could be simulated using an ensemble of snow models in conjunction with remotely sensed products. The model ensemble, obtained by perturbing forcing data and the subgrid coefficient of SWE variability (Liston, 2004), was drastically improved by assimilating fractional snow covered area (fSCA) over the melt season. However, the approach by Aalstad et al. (2018) is not directly applicable for *CG Crocus*, as the snow model neglects most internal snow processes, and the ensemble uses an empirical coefficient to produce spatial variability. Retrieval of fSCA could nevertheless be used in *CG Crocus* to correct the melt out dates of e.g. the ridge and snowbed tile, but would not necessarily capture mid-winter melt out and re-establishment of the snow cover. An approach assimilating data over the whole snow season is presented by Cluzet et al. (2020), where satellite observations of snow reflectance are used to improve CROCUS simulations of microstructural snow properties in the French Alps. Regrettably, the retrieval of optical products over the snow season at Arctic sites is not possible due to polar night (24. Oct. – 17. Feb. in Bayelva), and Aalstad et al. (2018) also note cloud cover as a limitation outside this period. To improve the simulation of spatial variable snowpack evolution in *CG Crocus*, it would be preferable to use a remotely sensed data source that is reliable throughout the snow season. For example, satellite microwave retrievals are not hampered by illumination and weather. The spatial resolution of microwave observations is however too coarse for acquisition of subgrid snow distributions, and internal snow properties obscure the retrievals (Lemmetyinen et al., 2018). Still, some recent approaches improve the spatial resolution by using passive and active microwave sensors in tandem (Lemmetyinen et al., 2018), and an algorithm for fSCA retrieval has been hypothesized (Xiao et al., 2020). However, it is unclear how the thick layers of basal ice frequently observed in Bayelva will be manifested in both optical and microwave snow products.

The three-tile simulation of Bayelva show that *CG Crocus* can be used to process-based assessment of how extreme weather events impact local ecosystems. Indeed, satellite derived vegetation indices reveal that Arctic greening trend over the last decades has been superimposed by localized Arctic browning in recent years (Osborne et al., 2018). Phoenix & Bjerke (2016) link this die-off of plant communities to the increased frequency and magnitude of extreme weather events, especially during winter. The mechanisms of wilting are variable, and include mid-winter bud burst, plant ice encasement, and frost drought from high irradiance and removal of snow cover. Further, experiments by Treharne et al. (2019) reveal that Arctic browning negatively impacts the ecosystem CO_2 fluxes, reducing the carbon sink capacity considerably. To increase our predictive capabilities of Arctic greenness and carbon budget, tools that capture the transient nature of these extreme events are required (Phoenix & Bjerke, 2016). *CG Crocus* is highly relevant in this context, as the segmentation of sub-grid topography enables identification of the areas which experience melt out, basal ice formation and periods of elevated GSTs during and after ROS-events and wintertime warm spells.

Such extreme events also affect herbivores, whose access to winter forage is limited by the presence of ground ice, so called “ice-locked pastures”. For example, winters with heavy ROS-events negatively impacted population growth rates of Svalbard reindeers are (Hansen et al., 2011), and also lead to increased displacement of individual reindeers (Loe et al., 2016). During the spring field campaign, reindeers where observed to seek refuge at high elevations where basal ice presence was reduced, and to eat kelp that was washed up on the shorelines. The implications can also be more acute, e.g. Putkonen et al. (2009) report mass die-offs of muskoxen in Arctic Canada in response to a single ROS-event in 2003. While these studies establish the link between the extreme event and the herbivore populations, they rely on snow surveys towards the end of the snow season, and do not capture the transient nature of the phenomena. *CG Crocus* might be used as an instrument for physically based studies of forage accessibility through the winter season, seacross terrain features and elevation gradients.

A key capability of *CG Crocus* is its potential to capture the spatial heterogeneity of permafrost degradation. Indeed, the three-tile simulation of Bayelva show spatially localized thaw (Table 16), which would be obscured in traditional single-tile simulations. While the full spatial variability of ground thermal regimes is not captured by *CG Crocus* (e.g. Figure 19), the end-members of the distribution are captured, and localized permafrost thaw can be detected. The full temperature distribution could in principle be reproduced by drastically increasing the number of model tiles, but this would also increase the complexity and computation time of the simulation. The setup with three tiles seems to be a suitable balance between computational expense and the ability to capture the observed spread.

Through its physically based calculation of snow transport, *CG Crocus* can potentially improve our ability to forecast how climate change will impact cold environments. As previously discussed, the inclusion of how snow microphysics affect erodability, distinguishes *CG Crocus* from other model approaches incorporating sub-grid snow variability. This is likely of relevance for projections of future climate, as parts the Arctic are projected to experience an increase in winter rainfall (Bintanja & Andry, 2017) and more frequent warm spells (Vikhamar-Schuler et al., 2016). This will have implications for the erodability of the snow cover, and the spatial distribution of GSTs and snow depths might differ from the current state. The simple, yet process-based parameterizations of lateral snow and water exchange, give *CG Crocus* the potential to enhance our predictive capabilities on how snow-dominated systems will be impacted by climate change.

6 Conclusions

From the presented work, the following conclusions are drawn:

- The parameterizations of snow microphysics from CROCUS are well suited for application in permafrost modelling environments, specifically the CryoGrid model suite. Its implementation in CryoGrid allows for inclusion of relevant snow processes not previously included, such as grain metamorphism, compaction and spectral variations in radiative transfer.
- Using a tiling-approach, lateral mass fluxes occurring at scales not captured by the horizontal dimensions of available forcing data can be represented. This includes process-based redistribution of snow through wind drift from more exposed to more sheltered areas, and gravity-driven lateral percolation between adjacent tiles.
- By dividing the Bayelva area into three landscapes units, the sub-grid variability of ground conditions can be simulated. The observed distribution of snow depths and SWE in spring is well reproduced, and the spatial variations in the temporal evolution of GSTs in the area are captured.
- The approach is able to simulate how the preceding snow conditions modulate the thermal impact of ROS-events, and reproduces how the snow cover melts in some areas, while others experience prolonged periods of elevated GSTs and the buildup of basal ice layers.
- The tiling-approach allows for simulations of landforms sustained by lateral snow transport, such as nunataqs and palsas, which would not be possible with purely one-dimensional approaches.
- The division of the landscape into interacting units facilitates the representation of how topographic features modulate the effects of climate change, which allows for identification of i.e. localized permafrost thaw, and the spatial distribution of ice-locked pastures and Arctic browning.
- The presented model setup features capabilities of relevance for a number of scientific disciplines, and provides active users with a useful tool for assessing sub-grid ground conditions in cold climates.

Reference list

Aalstad, K., Westermann, S., & Bertino, L. (2020). Evaluating satellite retrieved fractional snow-covered area at a high-Arctic site using terrestrial photography. *Remote Sensing of Environment*, *239*. https://doi.org/10.1016/j.rse.2019.111618

Aalstad, K., Westermann, S., Schuler, T. V., Boike, J., & Bertino, L. (2018). Ensemble-based assimilation of fractional snow-covered area satellite retrievals to estimate the snow distribution at Arctic sites. *The Cryosphere*, *12*(1), 247–270. https://doi.org/10.5194/tc-12-247-2018

Aas, Kjetil S., Martin, L., Nitzbon, J., Langer, M., Boike, J., Lee, H., Berntsen, T. K., & Westermann, S. (2019). Thaw processes in ice-rich permafrost landscapes represented with laterally coupled tiles in a land surface model. *The Cryosphere*, *13*(2), 591–609. https://doi.org/10.5194/tc-13-591-2019

Aas, Kjetil Schanke, Gisnås, K., Westermann, S., & Berntsen, T. K. (2017). A Tiling Approach to Represent Subgrid Snow Variability in Coupled Land Surface–Atmosphere Models. *Journal of Hydrometeorology*, *18*(1), 49–63. https://doi.org/10.1175/JHM-D-16-0026.1

Armstrong, R. L., & Brun, E. (2008). *Snow and Climate: Physical Processes, Surface Energy Exchange and Modeling*. Cambridge University Press.

Asanovic, K., Bodik, R., Christopher, B., Joseph, C., Gebis, J., Husbands, P., Keutzer, K., Patterson, D. A., Lester, W., John, P., Samuel, S., Williams, W., & Yelick, K. A. (2006). *The Landscape of Parallel Computing Research: A View from Berkeley*. http://www.eecs.berkeley.edu/Pubs/TechRpts/2006/EECS-2006-183.html

Bintanja, R., & Andry, O. (2017). Towards a rain-dominated Arctic. *Nature Climate Change*, *7*(4), 263–267. https://doi.org/10.1038/nclimate3240

Blöschl, G. (1999). Scaling issues in snow hydrology. *Hydrological Processes*, *13*(14-15), 2149–2175. https://doi.org/10.1002/(SICI)1099-1085(199910)13:14/15<2149::AID-HYP847>3.0.CO;2-8

Boike, J., Juszak, I., Lange, S., Chadburn, S., Burke, E., Paul Overduin, P., Roth, K., Ippisch, O., Bornemann, N., Stern, L., Gouttevin, I., Hauber, E., & Westermann, S. (2018). A 20-year record (1998-2017) of permafrost, active layer and meteorological conditions at a high Arctic permafrost research site (Bayelva, Spitsbergen). *Earth System Science Data*, *10*(1), 355–390. https://doi.org/10.5194/essd-10-355-2018

Boone, A. (2002). *Description du Schema de Neige ISBA-ES (Explicit Snow)*.

Borge, A. F., Westermann, S., Solheim, I., & Etzelmüller, B. (2017). Strong degradation of palsas and peat plateaus in northern Norway during the last 60 years. *The Cryosphere*, *11*, 1–16. https://doi.org/10.5194/tc-11-1-2017

Brown, R., Vikhamar Schuler, D., Bulygina, O., Derksen, C., Luojus, K., Mudryk, L., Wang, L., & Yang, D. (2017). *Snow, Water, Ice and Permafrost in the Arctic (SWIPA)*.

Brun, E., Martin, E., & Spiridonov, V. (1997). Coupling a multi-layered snow model with a GCM. *Annals of Glaciology*, *25*, 66–72. https://doi.org/10.3189/s0260305500013811

Brun, Eric, Vionnet, V., Boone, A., Decharme, B., Peings, Y., Valette, R., Karbou, F., & Morin, S. (2013). Simulation of northern Eurasian local snow depth, mass, and density using a detailed snowpack model and meteorological reanalyses. *Journal of Hydrometeorology*, *14*(1), 203–219. https://doi.org/10.1175/JHM-D-12-012.1

Calonne, N., Flin, F., Morin, S., Lesaffre, B., du Roscoat, S. R., & Geindreau, C. (2011). Numerical and experimental investigations of the effective thermal conductivity of snow. *Geophysical Research Letters*, *38*(23), n/a-n/a. https://doi.org/10.1029/2011GL049234

Calonne, Neige, Milliancourt, L., Burr, A., Philip, A., Martin, C. L., Flin, F., & Geindreau, C. (2019). Thermal Conductivity of Snow, Firn, and Porous Ice From 3-D Image-Based Computations. *Geophysical Research Letters*, *46*(22), 13079–13089. https://doi.org/10.1029/2019GL085228

Choi, Y., & Okos, M. R. (1986). Effects of Temperature and Composition on the Thermal Properties of Foods. In *Food Engineering and Process Applications* (1st ed., pp. 93–101). Elsevier Applied Science Publishers.

Christiansen, H. H., Gilbert, G. L., Demidov, N., Guglielmin, M., Isaksen, K., Osuch, M., & Boike, J. (2016). *Permafrost thermal snapshot and active-layer thickness in Svalbard*.

Clark, M. P., Hendrikx, J., Slater, A. G., Kavetski, D., Anderson, B., Cullen, N. J., Kerr, T., Örn Hreinsson, E., & Woods, R. A. (2011). Representing spatial variability of snow water equivalent in hydrologic and land-surface models: A review. In *Water Resources Research* (Vol. 47, Issue 7). John Wiley & Sons, Ltd. https://doi.org/10.1029/2011WR010745

Cluzet, B., Revuelto, J., Lafaysse, M., Tuzet, F., Cosme, E., Picard, G., Arnaud, L., & Dumont, M. (2020). Towards the assimilation of satellite reflectance into semi-distributed ensemble snowpack simulations. *Cold Regions Science and Technology*, *170*, 102918. https://doi.org/10.1016/j.coldregions.2019.102918

Colbeck, S. C. (1972). A Theory of Water Percolation in Snow. *Journal of Glaciology*, *11*(63), 369–385. https://doi.org/10.3189/s0022143000022346

Colbeck, S. C. (1979). WATER FLOW THROUGH HETEROGENEOUS SNOW . *Cold Regions Science and Technology*, *1*, 37–45.

Coléou, C., & Lesaffre, B. (1998). Irreducible water saturation in snow: experimental results in a cold laboratory. *Annals of Glaciology*, *26*, 64–68. https://doi.org/10.3189/1998aog26-1-64-68

D’amboise, C. J. L., Müller, K., Oxarango, L., Morin, S., & Schuler, T. V. (2017). Implementation of a physically based water percolation routine in the Crocus/SURFEX (V7.3) snowpack model. *Geosci. Model Dev*, *10*, 3547–3566. https://doi.org/10.5194/gmd-10-3547-2017

Dadic, R., Mott, R., Lehning, M., & Burlando, P. (2010). Wind influence on snow depth distribution and accumulation over glaciers. *Journal of Geophysical Research: Earth Surface*, *115*(1), F01012. https://doi.org/10.1029/2009JF001261

Dingman, S. L. (2015). *Physical hydrology* (3rd ed.). Waveland Press, Long Grove, IL, USA.

Eckerstorfer, M., & Christiansen, H. (2011). The “high arctic maritime snow climate” in Central svalbard. *Arctic, Antarctic, and Alpine Research*, *43*(1), 11–21. https://doi.org/10.1657/1938-4246-43.1.11

ECMWF. (2007). Part IV: Physical Processes. In *IFS Documentation CY31R1*. ECMWF. https://www.ecmwf.int/node/9221

ESA. (2015). *SENTINEL-2 User Handbook*.

Fiddes, J., & Gruber, S. (2012). TopoSUB: a tool for efficient large area numerical modelling in complex topography at sub-grid scales. *Geoscientific Model Development*, *5*(5), 1245–1257. https://doi.org/10.5194/gmd-5-1245-2012

Foken, T. (2008). Micrometeorology. In *Micrometeorology*. Springer Berlin Heidelberg.

https://doi.org/10.1007/978-3-540-74666-9

Førland, E. J., Benestad, R., Hanssen-Bauer, I., Haugen, J. E., & Skaugen, T. E. (2011). Temperature and Precipitation Development at Svalbard 1900–2100. *Advances in Meteorology*, *2011*, 1–14. https://doi.org/10.1155/2011/893790

Førland, E. J., Isaksen, K., Lutz, J., Hanssen-Bauer, I., Schuler, T. V., Dobler, A., Gjelten, H. M., & Vikhamar-Schuler, D. (2020). Measured and modelled historical precipitation trends for Svalbard. *Journal of Hydrometeorology*, JHM-D-19-0252.1. https://doi.org/10.1175/JHM-D-19-0252.1

Fricke, B. A., & Becker, B. R. (2001). Evaluation of thermophysical property models for foods. *HVAC&R RESEARCH*, *7*(4), 311–330.

Gisnås, K., Westermann, S., Schuler, T. V., Litherland, T., Isaksen, K., Boike, J., & Etzelmüller, B. (2014). A statistical approach to represent small-scale variability of permafrost temperatures due to snow cover. *The Cryosphere*, *8*(6), 2063–2074. https://doi.org/10.5194/tc-8-2063-2014

Gordon, M., Simon, K., & Taylor, P. A. (2006). On snow depth predictions with the Canadian Land Surface Scheme including a parametrization of blowing snow sublimation. *Atmosphere - Ocean*, *44*(3), 239–255. https://doi.org/10.3137/ao.440303

Hachem, S., Duguay, C. R., & Allard, M. (2012). Comparison of MODIS-derived land surface temperatures with ground surface and air temperature measurements in continuous permafrost terrain. *Cryosphere*, *6*(1), 51–69. https://doi.org/10.5194/tc-6-51-2012

Hagen, J. O., Kohler, J., Melvold, K., & Winther, J. G. (2003). Glaciers in Svalbard: Mass balance, runoff and freshwater flux. *Polar Research*, *22*(2), 145–159. https://doi.org/10.3402/polar.v22i2.6452

Hansen, B. B., Aanes, R., Herfindal, I., Kohler, J., Sæther, B. E., & Oli, M. K. (2011). Climate, icing, and wild arctic reindeer: Past relationships and future prospects. *Ecology*, *92*(10), 1917–1923. https://doi.org/10.1890/11-0095.1

Hanssen-Bauer, I., Førland, E. J., Hisdal, H., Mayer, S., Sandø, A. B., & Sorteberg, A. (2019). *Climate in Svalbard 2100* (Issue 1).

Hornum, M. T., Hodson, A., Jessen, S., Bense, V., & Senger, K. (2020). Numerical modelling of permafrost spring discharge and open-system pingo formation induced by basal permafrost aggradation. *The Cryosphere Discussions*, *February*, 1–36.

Humlum, O. (2002). Modelling late 20th-century precipitation in Nordenskiöld Land, Svalbard, by geomorphic means. *Norsk Geografisk Tidsskrift*, *56*(2), 96–103. https://doi.org/10.1080/002919502760056413

Humlum, O. (2005). Holocene permafrost aggradation in Svalbard. *Geological Society Special Publication*, *242*(1), 119–130. https://doi.org/10.1144/GSL.SP.2005.242.01.11

Humlum, O., Instanes, A., & Sollid, J. L. (2003). Permafrost in Svalbard: A review of research history, climatic background and engineering challenges. *Polar Research*, *22*(2), 191–215. https://doi.org/10.3402/polar.v22i2.6455

IPCC. (2018). *Climate Change 2013: The Physical Science Basis. Contribution of Working Group I to the Fifth Assessment Report of the Intergovernmental Panel on Climate Change* (T. F. Stocker, D. Qin, G.-K. Plattner, M. Tignor, S. K. Allen, J. Boschung, A. Nauels, Y. Xia, B. V., & P. M. Midgley (Eds.)). Cambridge University Press, Cambridge, United Kingdom and New York, NY, USA.

Isaksen, K., Mühll, D. V., Gubler, H., Kohl, T., & Sollid, J. L. (2000). Ground surface temperature reconstruction based on data from a deep borehole in permafrost at Janssonhaugen Svalbard.

Annals of Glaciology, *31*, 287–294. https://doi.org/10.3189/172756400781820291

Isaksen, K., Nordli, Ø., Førland, E. J., Łupikasza, E., Eastwood, S., & Niedźwiedź, T. (2016). Recent warming on Spitsbergen-Influence of atmospheric circulation and sea ice cover. *Journal of Geophysical Research: Atmospheres*, *121*(20), 11,913-11,931. https://doi.org/10.1002/2016JD025606

Jaedicke, C., & Sandvik, A. D. (2002). High resolution snow distribution data from complex Arctic terrain: A tool for model validation. *Natural Hazards and Earth System Sciences*, *2*(3–4), 147–155. https://doi.org/10.5194/nhess-2-147-2002

Kochanski, K., Anderson, R. S., & Tucker, G. E. (2019). The evolution of snow bedforms in the Colorado Front Range and the processes that shape them. *The Cryosphere*, *13*(4), 1267–1281. https://doi.org/10.5194/tc-13-1267-2019

Køltzow, M., Casati, B., Bazile, E., Haiden, T., & Valkonen, T. (2019). An NWP Model Intercomparison of Surface Weather Parameters in the European Arctic during the Year of Polar Prediction Special Observing Period Northern Hemisphere 1. *Weather and Forecasting*, *34*(4), 959–983. https://doi.org/10.1175/WAF-D-19-0003.1

Koster, R. D., & Suarez, M. J. (1992). Modeling the land surface boundary in climate models as a composite of independent vegetation stands. *Journal of Geophysical Research*, *97*(D3), 2697. https://doi.org/10.1029/91JD01696

Kump, L. R., Kasting, J. F., & Crane, R. G. (2009). *The Earth System* (3rd ed.). Pearson.

Lafaysse, M., Cluzet, B., Dumont, M., Lejeune, Y., Vionnet, V., & Morin, S. (2017). A multiphysical ensemble system of numerical snow modelling. *The Cryosphere*, *11*, 1173–1198. https://doi.org/10.5194/tc-11-1173-2017

Lehning, M., Löwe, H., Ryser, M., & Raderschall, N. (2008). Inhomogeneous precipitation distribution and snow transport in steep terrain. *Water Resources Research*, *44*(7). https://doi.org/10.1029/2007WR006545

Lehning, Michael, Völksch Ingo, I., Gustafsson, D., Nguyen, T. A., Stähli, M., & Zappa, M. (2006). ALPINE3D: A detailed model of mountain surface processes and its application to snow hydrology. *Hydrological Processes*, *20*(10), 2111–2128. https://doi.org/10.1002/hyp.6204

Lemke, P., Ren, J., Alley, R. B., Allison, I., Carrasco, J., Flato, G., Fujii, Y., Kaser Austria, G., Mote, P., Thomas, R. H., & Zhang, T. (2007). Observations: Changes in Snow, Ice and Frozen Ground. In S. Solomon, D. Qin, M. Manning, Z. Chen, M. Marquis, K.B. Averyt, M. Tignor, & H.L. Miller (Eds.), *Climate Change 2007: The Physical Science Basis. Contribution of Working Group I to the Fourth Assessment Report of the Intergovernmental Panel on Climate Change*. Cambridge University Press.

Lemmetyinen, J., Derksen, C., Rott, H., Macelloni, G., King, J., Schneebeli, M., Wiesmann, A., Leppänen, L., Kontu, A., & Pulliainen, J. (2018). Retrieval of Effective Correlation Length and Snow Water Equivalent from Radar and Passive Microwave Measurements. *Remote Sensing*, *10*(2), 170. https://doi.org/10.3390/rs10020170

Liestøl, O. (1975). Pingos, springs, and permafrost in Spitsbergen. *Norsk Polarinstitutts Årbok*, 7–29.

Liston, G. E. (2004). Representing subgrid snow cover heterogeneities in regional and global models. *Journal of Climate*, *17*(6), 1381–1397. https://doi.org/10.1175/1520-0442(2004)017<1381:RSSCHI>2.0.CO;2

Liston, G. E., & Elder, K. (2006). A distributed snow-evolution modeling system (snowmodel). *Journal* *of Hydrometeorology*, *7*(6), 1259–1276. https://doi.org/10.1175/JHM548.1

Liston, G. E., & Sturm, M. (1998). A snow-transport model for complex terrain. *Journal of Glaciology*, *44*(148), 498–516. https://doi.org/10.3189/s0022143000002021

Loe, L. E., Hansen, B. B., Stien, A., Albon, S. D., Bischof, R., Carlsson, A., Irvine, R. J., Meland, M., Rivrud, I. M., Ropstad, E., Veiberg, V., & Mysterud, A. (2016). Behavioral buffering of extreme weather events in a high-Arctic herbivore. *Ecosphere*, *7*(6). https://doi.org/10.1002/ecs2.1374

Loe, L. E., Hansen, B. B., Stien, A., D. Albon, S., Bischof, R., Carlsson, A., Irvine, R. J., Meland, M., Rivrud, I. M., Ropstad, E., Veiberg, V., & Mysterud, A. (2016). Behavioral buffering of extreme weather events in a high-Arctic herbivore. *Ecosphere*, *7*(6). https://doi.org/10.1002/ecs2.1374

Martin, L. C. P., Nitzbon, J., Aas, K. S., Etzelmüller, B., Kristiansen, H., & Westermann, S. (2019). Stability Conditions of Peat Plateaus and Palsas in Northern Norway. *Journal of Geophysical Research: Earth Surface*, *124*(3), 705–719. https://doi.org/10.1029/2018JF004945

Maturilli, M., Herber, A., & König-Langlo, G. (2013). Climatology and time series of surface meteorology in Ny-Ålesund, Svalbard. *Earth System Science Data*, *5*(1), 155–163. https://doi.org/10.5194/essd-5-155-2013

MET.no. (2020). *Yr - "Ny-Ålesund" - historikk*. https://www.yr.no/nb/historikk/graf/1-2837778/Norge/Svalbard/Svalbard/Ny-Ålesund?q=2017

Monin, A. S., & Obukhov, A. M. (1954). "Basic laws of turbulent mixing in the surface layer of the atmosphere." *Tr. Akad. Nauk. SSSR Geophiz. Inst.*, *24*(151), 163-187W.

Moroni, B., Arnalds, O., Dagsson-Waldhauserová, P., Crocchianti, S., Vivani, R., & Cappelletti, D. (2018). Mineralogical and Chemical Records of Icelandic Dust Sources Upon Ny-Ålesund (Svalbard Islands). *Frontiers in Earth Science*, *6*, 187. https://doi.org/10.3389/feart.2018.00187

Mott, R., Schirmer, M., Bavay, M., Grünewald, T., & Lehning, M. (2010). Understanding snow-transport processes shaping the mountain snow-cover. *The Cryosphere*, *4*(4), 545–559. https://doi.org/10.5194/tc-4-545-2010

Müller, M., Batrak, Y., Kristiansen, J., Køltzow, M. A. Ø., Noer, G., & Korosov, A. (2017). Characteristics of a convective-scale weather forecasting system for the European Arctic. *Monthly Weather Review*, *145*(12), 4771–4787. https://doi.org/10.1175/MWR-D-17-0194.1

Nitzbon, J., Langer, M., Westermann, S., Martin, L., Aas, K. S., & Boike, J. (2019). Pathways of ice-wedge degradation in polygonal tundra under different hydrological conditions. *The Cryosphere*, *13*(4), 1089–1123. https://doi.org/10.5194/tc-13-1089-2019

Niu, G. Y., Yang, Z. L., Mitchell, K. E., Chen, F., Ek, M. B., Barlage, M., Kumar, A., Manning, K., Niyogi, D., Rosero, E., Tewari, M., & Xia, Y. (2011). The community Noah land surface model with multiparameterization options (Noah-MP): 1. Model description and evaluation with local-scale measurements. *Journal of Geophysical Research Atmospheres*, *116*(12). https://doi.org/10.1029/2010JD015139

Nowak, A., & Hodson, A. (2013). Hydrological response of a High-Arctic catchment to changing climate over the past 35 years: A case study of Bayelva watershed, Svalbard. *Polar Research*, *32*(SUPPL.), 1–16. https://doi.org/10.3402/polar.v32i0.19691

Obu, J., Westermann, S., Bartsch, A., Berdnikov, N., Christiansen, H. H., Dashtseren, A., Delaloye, R., Elberling, B., Etzelmüller, B., Kholodov, A., Khomutov, A., Kääb, A., Leibman, M. O., Lewkowicz, A. G., Panda, S. K., Romanovsky, V., Way, R. G., Westergaard-Nielsen, A., Wu, T., … Zou, D. (2019). Northern Hemisphere permafrost map based on TTOP modelling for 2000–2016 at 1 km2 scale. In *Earth-Science Reviews* (Vol. 193, pp. 299–316). Elsevier B.V. https://doi.org/10.1016/j.earscirev.2019.04.023

Osborne, E., Richter-Menge, J., & Jeffries, M. (2018). Arctic Report Card 2018. In *NOAA*.

Østby, T. I., Vikhamar Schuler, T., Ove Hagen, J., Hock, R., Kohler, J., & Reijmer, C. H. (2017). Diagnosing the decline in climatic mass balance of glaciers in Svalbard over 1957-2014. *Cryosphere*, *11*(1), 191–215. https://doi.org/10.5194/tc-11-191-2017

Pahaut, E. (1976). La métamorphose des cristaux de neige (Snow crystal metamorphosis). *Monographies de La Météorologie Nationale*, *96*.

Peeters, B., Pedersen, Å. Ø., Loe, L. E., Isaksen, K., Veiberg, V., Stien, A., Kohler, J., Gallet, J. C., Aanes, R., & Hansen, B. B. (2019). Spatiotemporal patterns of rain-on-snow and basal ice in high Arctic Svalbard: Detection of a climate-cryosphere regime shift. *Environmental Research Letters*, *14*(1). https://doi.org/10.1088/1748-9326/aaefb3

Phoenix, G. K., & Bjerke, J. W. (2016). Arctic browning: extreme events and trends reversing arctic greening. *Global Change Biology*, *22*(9), 2960–2962. https://doi.org/10.1111/gcb.13261

Pitman, A. J. (2003). The evolution of, and revolution in, land surface schemes designed for climate models. *International Journal of Climatology*, *23*(5), 479–510. https://doi.org/10.1002/joc.893

Pörtner, H.-O., Roberts, D. C., Masson-Delmotte, V., Zhai, P., Tignor, M., Poloczanska, E., Mintenbeck, K., Alegría, A., Nicolai, M., Okem, A., Petzold, J., Rama, B., & Weyer, N. M. (2019). *IPCC Special Report on the Ocean and Cryosphere in a Changing Climate*.

Pramanik, A., Van Pelt, W., Kohler, J., & Schuler, T. V. (2018). Simulating climatic mass balance, seasonal snow development and associated freshwater runoff in the Kongsfjord basin, Svalbard (1980-2016). *Journal of Glaciology*, *64*(248), 943–956. https://doi.org/10.1017/jog.2018.80

Putkonen, J., Grenfell, T. C., Rennert, K., Bitz, C., Jacobson, P., & Russell, D. (2009). Rain on Snow: Little Understood Killer in the North. *Eos, Transactions American Geophysical Union*, *90*(26), 221–222. https://doi.org/10.1029/2009EO260002

R. Klein, D. (2016). Polar ecosystem. In *Encyclopædia Britannica*. https://www.britannica.com/science/polar-ecosystem#ref589329

Raleigh, M. S., Lundquist, J. D., & Clark, M. P. (2015). Exploring the impact of forcing error characteristics on physically based snow simulations within a global sensitivity analysis framework. *Hydrology and Earth System Sciences*, *19*(7), 3153–3179. https://doi.org/10.5194/hess-19-3153-2015

Smith, M. W., & Riseborough, D. W. (2002). Climate and the limits of permafrost: a zonal analysis. *Permafrost and Periglacial Processes*, *13*(1), 1–15. https://doi.org/10.1002/ppp.410

Stünzi, S., Boike, J., Herzschuh, U., Kruse, S., Schneider von Deimling, T., & Langer, M. (2019). Modeling Permafrost Sensitivity in Arctic Forest. *AGU Fall Meeting 2019*.

Sturm, M., Holmgren, J., König, M., & Morris, K. (1997). The thermal conductivity of seasonal snow. *Journal of Glaciology*, *43*(143), 26–41. https://doi.org/10.1017/S0022143000002781

Tabler, R. D. (1994). *Design Guidelines for the Control of Blowing and Drifting Snow*.

Thuesen, N. P., & Barr, S. (2020). Svalbard. In *Store norske leksikon*. https://snl.no/Svalbard

Treharne, R., Bjerke, J. W., Tømmervik, H., Stendardi, L., & Phoenix, G. K. (2019). Arctic browning: Impacts of extreme climatic events on heathland ecosystem CO $_2$ fluxes. *Global Change Biology*, *25*(2), 489–503. https://doi.org/10.1111/gcb.14500

Trofaier, A. M., Westermann, S., & Bartsch, A. (2017). Progress in space-borne studies of permafrost for climate science: Towards a multi-ECV approach. *Remote Sensing of Environment*, *203*, 55–70. https://doi.org/10.1016/j.rse.2017.05.021

Vaughan, D. G., Comiso, J. C., Allison, I., Carrasco, J., Kaser, G., Kwok, R., Mote, P., Murray, T., Paul, F., Ren, J., Rignot, E., Solomina, O., Steffen, K., Zhang, T., Stocker, [, Qin, D., Plattner, G.-K., Tignor, M., Allen, S. K., … Kwok, R. (2013). Observations: Cryosphere. In T. F. Stocker, D. Qin, G.-K. Plattner, M. Tignor, S. K. Allen, J. Boschung, A. Nauels, Y. Xia, V. Bex, & P. M. Midgley (Eds.), *Climate Change 2013: The Physical Sci-ence Basis. Contribution of Working Group I to the Fifth Assessment Report of the Intergovernmental Panel on Climate Change*. Cambridge University Press, Cambridge, United Kingdom and New York, NY, USA.

Vikhamar-Schuler, D., Isaksen, K., Haugen, J. E., Tømmervik, H., Luks, B., Schuler, T. V., & Bjerke, J. W. (2016). Changes in winter warming events in the nordic arctic region. *Journal of Climate*, *29*(17), 6223–6244. https://doi.org/10.1175/JCLI-D-15-0763.1

Vionnet, V., Brun, E., Morin, S., Boone, A., Faroux, S., Le Moigne, P., Martin, E., & Willemet, J. M. (2012). The detailed snowpack scheme Crocus and its implementation in SURFEX v7.2. *Geoscientific Model Development*, *5*(3), 773–791. https://doi.org/10.5194/gmd-5-773-2012

Walker, D. A., Billings, W. D., & Molenaar, J. G. De. (2001). Snow-Vegetation Interactions in Tundra Environments. In *Snow Ecology* (pp. 266–324). Cambridge University Press. http://www.geobotany.org/library/pubs/WalkerDA2001_SnowEcol_ch6_266.pdf

Walvoord, M. A., & Kurylyk, B. L. (2016). Hydrologic Impacts of Thawing Permafrost-A Review. *Vadose Zone Journal*, *15*(6), vzj2016.01.0010. https://doi.org/10.2136/vzj2016.01.0010

Westermann, S., Boike, J., Guglielmin, M., Gisnås, K., & Etzelmüller, B. (2015). *Snow melt monitoring near Ny-Ålesund, Svalbard, using Automatic Camera Systems.* https://doi.org/10.1594/PANGAEA.846617

Westermann, S., Boike, J., Langer, M., Schuler, T. V., & Etzelmüller, B. (2011). Modeling the impact of wintertime rain events on the thermal regime of permafrost. *The Cryosphere*, *5*(4), 945–959. https://doi.org/10.5194/tc-5-945-2011

Westermann, S., Langer, M., Boike, J., Heikenfeld, M., Peter, M., Etzelmüller, B., & Krinner, G. (2016). Simulating the thermal regime and thaw processes of ice-rich permafrost ground with the land-surface model CryoGrid 3. *Geoscientific Model Development*, *9*(2), 523–546. https://doi.org/10.5194/gmd-9-523-2016

Westermann, S., Schuler, T. V., Gisnås, K., & Etzelmüller, B. (2013). Transient thermal modeling of permafrost conditions in Southern Norway. *The Cryosphere*, *7*(2), 719–739. https://doi.org/10.5194/tc-7-719-2013

Wever, N., Fierz, C., Mitterer, C., Hirashima, H., & Lehning, M. (2014). The Cryosphere Solving Richards Equation for snow improves snowpack meltwater runoff estimations in detailed multi-layer snowpack model. *The Cryosphere*, *8*, 257–274. https://doi.org/10.5194/tc-8-257-2014

Wever, N., Schmid, L., Heilig, A., Eisen, O., Fierz, C., & Lehning, M. (2015). Verification of the multi-layer SNOWPACK model with different water transport schemes. *The Cryosphere*, *9*(6), 2271–2293. https://doi.org/10.5194/tc-9-2271-2015

Wickström, S., Jonassen, M. O., Vihma, T., & Uotila, P. (2020). Trends in cyclones in the high-latitude North Atlantic during 1979–2016. *Quarterly Journal of the Royal Meteorological Society*, *146*(727), 762–779. https://doi.org/10.1002/qj.3707

Xiao, X., Liang, S., He, T., Wu, D., Pei, C., & Gong, J. (2020). Estimating fractional snow cover from passive microwave brightness temperature data using MODIS snow cover product over North America. *The Cryosphere Discussions*, 1–40. https://doi.org/10.5194/tc-2019-280

Yen, Y.-C. (1981). *REVIEW OF THERMAL PROPERTIES OF SNOW, ICE AND SEA ICE. REPORT 81-10*.

Zhang, T. (2005). Influence of the seasonal snow cover on the ground thermal regime: An overview. *Reviews of Geophysics*, *43*(4), RG4002. https://doi.org/10.1029/2004RG000157

Zhao, W., & Li, A. (2015). A Review on Land Surface Processes Modelling over Complex Terrain. *Advances in Meteorology*, 17 pages. https://doi.org/10.1155/2015/607181

Appendix

Other elements of the MSc work

Chronological list of contributions of the MSc work beyond the MSc thesis. The authors' role is declared within the brackets.

Zweigel, R. B., Westermann, S., Varpe, Ø., Hansen, B. B. and Isaksen, K. *Assessing sub-grid ground conditions during winter: A snow modelling approach*. Svalbard Science Conference, 5 .- 6. November 2019, Oslo. (**Poster**)

2nd International CryoGrid Hackathon, 18. – 20. November 2019, Kloster-Lehnin, Brandenburg, Germany. *Technical meeting on progressing CryoGrid to an operational state.* (**Participant**)

Zweigel, R. B.: *Hvordan kan en snøskred-modell bli brukt til å studere permafrost?* Oslo Geofysiske Forening - medlemsmøte, 12. Februar 2020, Oslo. (**Talk**)

Zweigel, R. B., Westermann, S., Nitzbon, J., Langer, M., Boike, J., Etzelmüller, B. and Schuler, T. V. (2020). *Simulating snow redistribution and its effect on the ground thermal regime at a high-Arctic site on Svalbard*. Manuscript in review for: Journal of Geophysical Research – Earth Surface. (**Corresponding author**)

Assessing sub-grid ground conditions during winter: A snow modelling approach

Robin Benjamin Zweigel1) 2), Sebastian Westermann1), Øystein Varpe2), Brage Bremset Hansen3) & Ketil Isaksen4)

1) University of Oslo, 2) University Centre in Svalbard, 3) Norwegian University of Science and Technology, 4) Norwegian Meteorological Institute

During Arctic winter the snow cover is a feature which governs most processes in both the living and non-living environment, and a transient representation of it is necessary for studies ranging from ecosystem dynamics to permafrost evolution. However, the snow cover is highly variable over scales which neither are captured by station observations, earth system models nor remote sensing.

Here, we use a dedicated numerical snow scheme based on the CryoGrid[1] framework to assess how **wind redistribution** and **wintertime warm events** shape the evolution of the snowpack. Our model implements parameterizations of snow physics and lateral snow fluxes from CROCUS[2], and is forced by readily available weather forecasting data[3]. Running several **parallel realizations** with the same input allows for redistribution of snow within one grid-cell of the forcing data. The number of realizations, each representing a fraction of the area, can be adjusted according to the present terrain complexity.

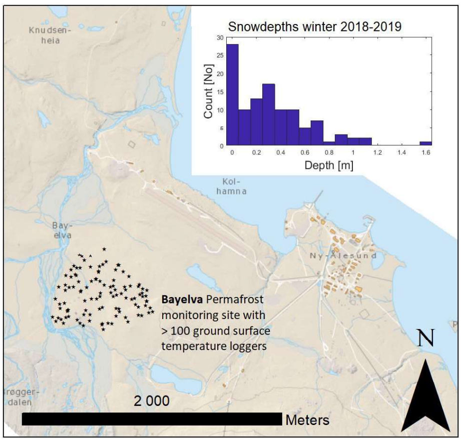

Figure 1: Location of the loggers within an area of about 0.5 km^2 at the Bayelva permafrost monitoring. The inset shows the measured snowdepths in April/May 2019.

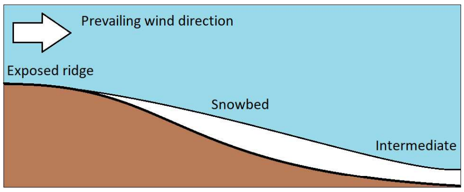

Figure 2: Schematic of the system we are attempting to model. The ridge is characterized by wind erosion, whereas the snowbed experiences substantial deposition. The three realizations are named after which location in this figure they represent.

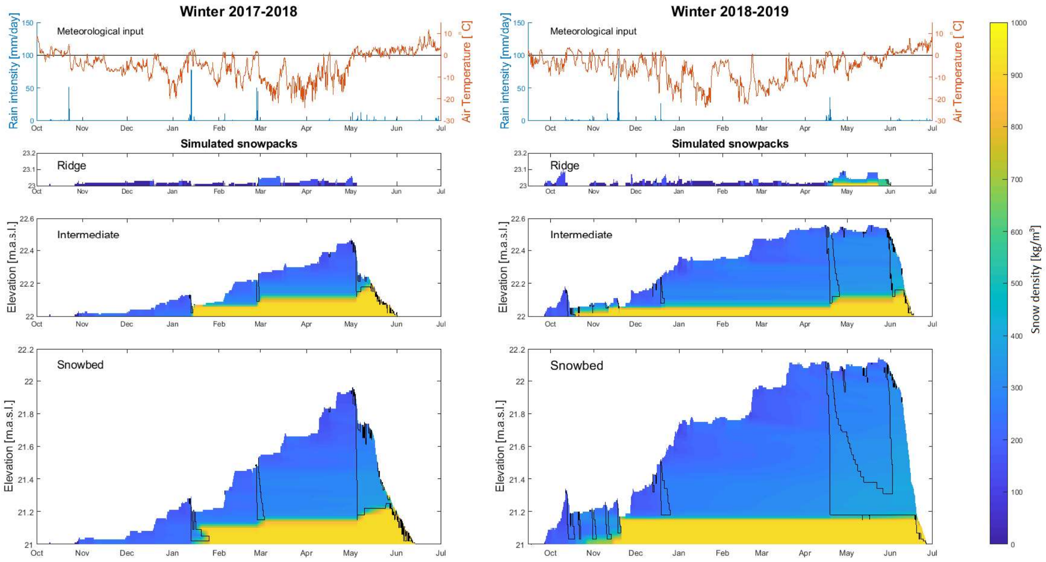

Figure 3: Meteorological data and simulated snowpacks from the last two winter seasons in the Bayelva catchment by Ny-Ålesund, showing amongst others the evolution of basal ice in response to rain-on-snow events. The black contour line indicates the 0°C isotherm and delineates the presence of liquid water.

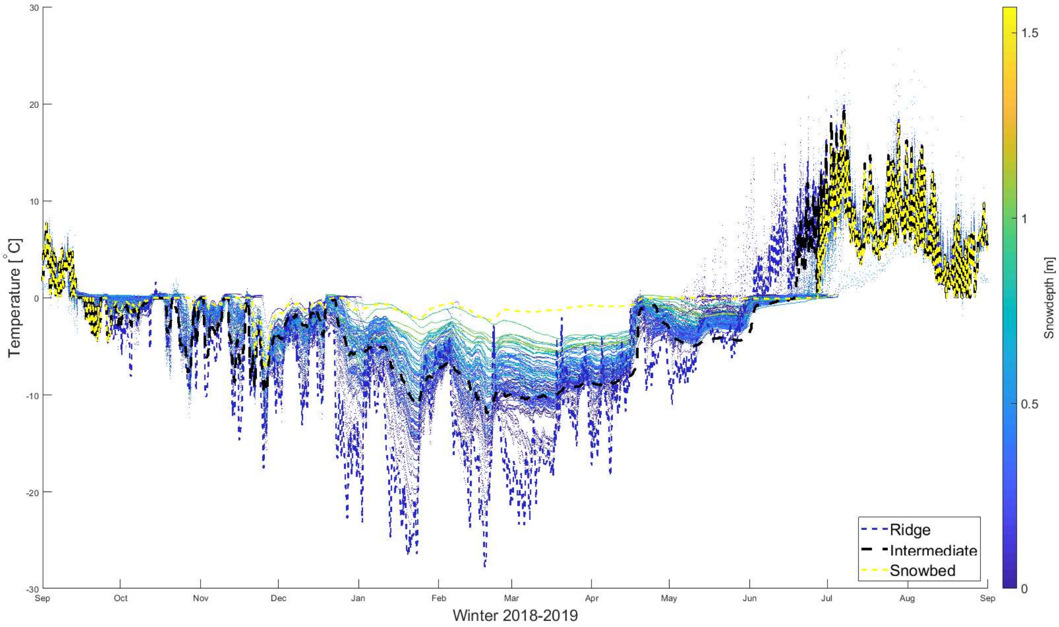

Figure 4: Comparison of modelled (dashed) and observed (dotted) ground surface temperatures for the Bayelva site shows that this approach captures the observed spread in the near-surface thermal regime (3-5cm depth) and meltout dates.

Compared to traditional 1-D approaches this scheme gives significant insight into the spread of ground and snow processes at a scale not captured by available meteorological data. Our scheme can both be used to capture the variations within a defined area, and to asses ground conditions across terrain features of interest (e.g. incised streams, ridge tops). Further work includes inclusion of lateral (liquid) water fluxes between realizations to more accurately represent the distribution of basal ice thicknesses, and establishment of a routine which determines the optimal number and constellation of realizations for an area based on available terrain data.

References

1. Westermann et al. (2016), *Simulating the thermal regime and thaw processes of ice-rich permafrost ground with the land-surface model CryoGrid 3.* Geosci. Model Dev., 9, 523–546
2. Vionnet et al. (2012), *The detailed snowpack scheme Crocus and its implementation in SURFEX v7.2.* Geosci. Model Dev., 5, 773–791
3. Müller et al. (2017), *Characteristics of a Convective-Scale Weather Forecasting System for the European Arctic.* Mon. Wea. Rev., 145, 4771–4787

Simulating snow redistribution and its effect on the ground thermal regime at a high-Arctic site on Svalbard

R. B. Zweigel[1,2], S. Westermann[1], J. Nitzbon[3,4], M. Langer[3,4], J. Boike[3,4], B. Etzelmüller[1], T. V. Schuler[1,2]

[1]Department of Geosciences, University of Oslo, Oslo, Norway

[2]The University Center in Svalbard, Longyearbyen, Norway

[3]Permafrost Research Section, Alfred Wegener Institute Helmholtz Centre for Polar and Marine Research, Potsdam, Germany

[4]Geography Department, Humboldt-Universität zu Berlin, Berlin, Germany

Corresponding author: Robin Benjamin Zweigel (robinbz@uio.no)

Key points

- In high-Arctic areas, wind redistribution of snow leads to a strong variability in snow depths and hence ground surface temperatures
- A parametrization for lateral transport of snow between three model tiles is implemented in the CryoGrid 3 permafrost model
- The three-tile setup reproduces the observed spatial variability of snow depths and ground surface temperatures in a process-based fashion

0 Abstract

In high-latitude and mountain regions, the seasonal snow cover exerts a strong control on the ground thermal regime. In addition to the spatial distribution of snowfall, local processes, such as redistribution by wind, snow metamorphism and percolation of water, contribute to the complex spatial distribution of snow depths and snow densities. This distribution has pronounced effects on ground temperatures during snow accumulation and ablation at small spatial scales which are typically not resolved by land surface models (LSMs). This limits our ability to simulate the local impacts of climate change on for example vegetation and permafrost. Here, we present a tiling approach combining the CryoGrid permafrost model with snow microphysics parametrizations from the CROCUS snow scheme to account for sub-grid lateral exchange of snow and water in a process-based way. We demonstrate that a simple setup with three coupled tiles, each representing a different snow accumulation class with a specific topographic setting, can reproduce the observed spread of winter-time ground surface temperatures and end-of-season snow distribution for a high-Arctic site on Svalbard.

Keywords

Snow redistribution; Rain on snow; permafrost modelling; Sub-grid processes; Svalbard; CryoGrid;

1 Introduction

The distribution of the seasonal snow cover plays a crucial role in the Earth's climate system due to its impact on the energy and water balance. Therefore, an accurate representation of the snow cover in process-based land surface models (LSMs) is a key to assess the effect of climate change on both local ecosystems and global atmospheric circulation (Pörtner et al., 2019). Climate change is most pronounced in the Arctic, warming at twice the global average rate (Osborne et al., 2018) and with rainfall projected to become the dominant form of precipitation in the future (Bintanja & Andry, 2017). Currently, parts of the Arctic are already experiencing an increase in rain-on-snow (ROS) events and wintertime warm spells (Hansen et al., 2014; Vikhamar-Schuler et al., 2016). Especially ROS events can have significant impacts on ecosystems due to basal ice formation, preventing herbivores from accessing pastures (e.g Putkonen & Roe, 2003; Vikhamar-Schuler et al., 2013) or accelerating warming and degradation of permafrost (Westermann et al., 2011).

The *s*now cover exhibits large variations in both spatial extent, duration and amount (measured as snow water equivalent, SWE). The spatial distribution of snow within a landscape is the product of different processes acting on a hierarchy of spatial scales (Clark et al., 2011). Variations in snowfall rates are usually controlled by the interplay between atmospheric circulation and topography and vary on spatial scales of kilometers and more. On the other hand, post-depositional redistribution of snow through wind transport acts on more local scales, often on the orders of tens to hundreds of meters. In many areas, this produces a complex pattern of snow depths that is difficult to reproduce by models. Weather models and climate reanalysis products can capture the regional distribution of snowfall, but their spatial resolution is far too coarse to implement local-scale processes like drifting snow. Dedicated snow models, such as Alpine3D (e.g. Lehning et al., 2006), are capable of resolving the local redistribution of snow by using a much finer grid, but such approaches are computationally expensive, making application over larger regions challenging.

The spatial distribution of snow is especially pronounced in Arctic and Alpine environments, where the sparse vegetation cover is insufficient to inhibit snow transport. Already snow depths of less than 1m have been shown to effectively decouple the ground temperature regime from the atmosphere (Hachem et al., 2012), keeping ground surface temperatures (GST) higher than near-surface air temperatures during winter (Trofaier et al., 2017). Therefore, the spatial pattern of snow depths in alpine and arctic environments results in pronounced small-scale variations of winter GST and snow cover duration (Gisnås et al. 2014) which give rise to significant local variations in vegetation cover, ground temperatures and active layer thickness in permafrost areas. Furthermore, the snow distribution modulates the thermal impact of ROS and winter melt events, with low snow areas potentially melting out completely, while basal ice layers form in locations with more snow. To adequately capture such processes, a transient representation of the spatial evolution of snow depths within a landscape is desirable. This highlights the importance of a physically based representation of the snow cover in LSMs, which can account for the governing processes at relevant spatial and temporal scales.

In this study, we extend the predictive capabilities of the CryoGrid 3 permafrost model (Westermann et al., 2016) with a process-based scheme that can simulate the lateral redistribution of snow due to wind drift. In particular, we aim for a scheme that can realistically reflect the observed sub-grid variability of snow pack evolution and ground surface temperatures. This is achieved by exploiting existing parameterizations for two critical processes governing sub-grid variability of SWE: wind redistribution of snow, and topography-driven lateral flow of liquid water within the snow cover. In this study, key parametrizations from the snow microphysics scheme CROCUS (Brun et al., 1989; Vionnet et al., 2012) have been implemented in the tiled version of CryoGrid 3 (Nitzbon et al. 2019), allowing for a physically based representation of wind erosion and deposition of snow. The model describes lateral exchange of snow and water between designated model realizations (denoted tiles) which represent the first-order topographic characteristics of the study site in a low relief permafrost environment on Svalbard.

2 Study site and measurements

Our study focuses on a ca. 500m x 500m area around the Bayelva high Arctic permafrost research site (78°55 N, 11°50 E) (Boike et al., 2018), close to the Ny-Ålesund research settlement on Svalbard (Fig. 1). The study area is bordered by the floodplain of the Bayelva river and is characterized by ridges and hills with low relief and elevations between 10 and 50 m a.s.l. (Figs. 1, 2). Around half of the soil surface is covered by low vascular plants, interrupted by mudboils and unvegetated patches and a high surface rock content (Boike et al., 2018). The climate is high Arctic with a maritime influence, featuring a mean annual air temperature of -5.2°C in Ny-Ålesund (1981-2010), with winter temperatures showing the largest variability (Førland et al., 2011). The precipitation in the area is variable: manual observations in Ny-Ålesund indicate a total precipitation between 350 and 450 mm/yr, while automated measurements of rainfall at the Bayelva site (Fig. 1) show between 150 and 350 mm/yr of liquid precipitation (Boike et al., 2018; Førland et al., 2011). The snow season in the Bayelva area typically extends from September until May.

The entire Svalbard region has been subject to accelerated climate change the last few decades. An increase of surface air temperature is observed at all monitoring sites on Svalbard over the last 4 decades, with the most pronounced change occurring in winter (Hanssen-Bauer et al., 2019). This includes Ny-Ålesund, where annual mean temperatures have increased by 0.71°C/decade over this period, with an even stronger increase in winter (Dec-Feb) temperatures (1.35°C/decade). Since 2006 the fjords in West Spitsbergen, including Kongsfjorden (Fig. 1), have been largely ice-free during winter, but also the sea ice cover in the East and North of Svalbard has declined (Hanssen-Bauer et al., 2019). This impacts local meteorological conditions through heat and moisture fluxes from ocean to the atmosphere, and is accompanied by an increase in days with rain during winter (ROS-events) (Hanssen-Bauer et al., 2019).

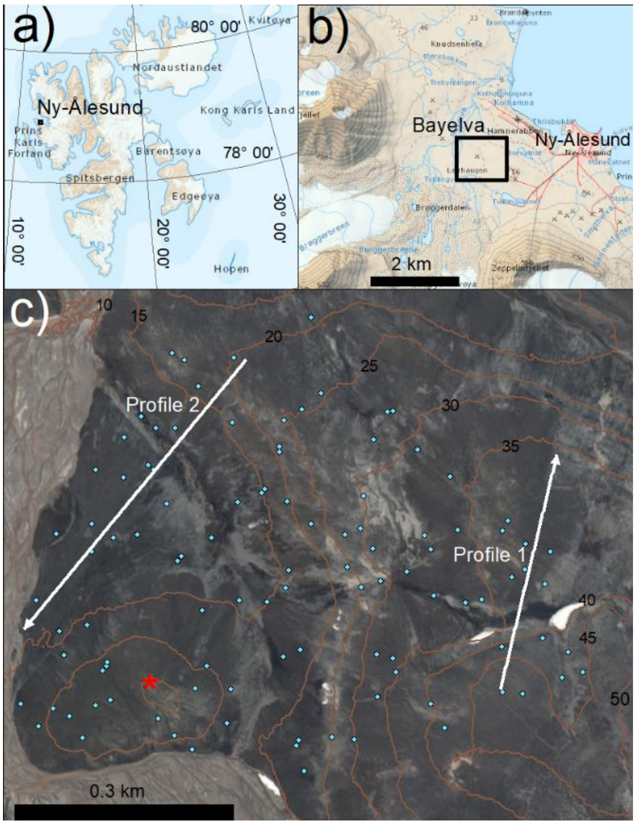

Fig. 1: (a) Overview of the Svalbard archipelago with the location of the Ny-Ålesund research settlement, and (b) the location of the Bayelva study area. (c) Orthophoto of the Bayelva study area with the red star indicating the location of the Bayelva high Arctic permafrost research site. Blue dots show the location of the ground temperature measurements used in this study, while Profile 1 and Profile 2 refer to the terrain profiles presented in Figure 2. The contour lines in (c) indicate the elevation in m a.s.l., maps and orthophoto courtesy of the Norwegian Polar Institute (www.npolar.no).

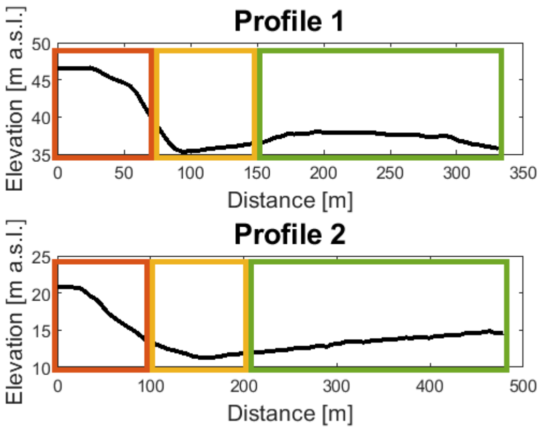

Fig. 2: Terrain profiles 1 and 2 (see Fig. 1c) with the conceptualization in landscape units as defined in Section 3.3: Red – Ridge; Yellow – Snow bed; Green – Ambient.

At the Bayelva research site, we utilize spatially distributed field measurements of snow depth and ground surface temperatures for the hydrological years 2017, 2018 and 2019 that can capture small-scale variations of the thermal regime in a statistically sound fashion. For this purpose, 109 iButton miniloggers (accuracy around 0.2°C) have been installed 2-3 cm below the ground surface at preselected, randomly distributed locations within the study area (Fig. 1) (Gisnås et al 2014). Temperatures are measured with 4 hours intervals, and at least 90 loggers were operational at any time in the study period. The ensemble of obtained records represents the transient evolution of the spatial variability in GST in the study area. The measurement array is described in more detail in Gisnås et al. (2014).

The GST measurements are complemented by annual snow surveys towards the end of the snow accumulation season (11 May 2017, 19 April 2018 and 25 April 2019). These surveys consisted of manual observations of the thickness of the snow cover at all 109 sites, as well as 3-10 detailed snow density profiles across the range of observed snow depths (throughout this study, we use the term "snow depth" to refer to the combined thickness of the snow column and the basal ice thickness). From the snow density profiles, the mean bulk snow density is derived for each year. At the majority of sites, the basal ice thickness was recorded manually, but this was not always possible especially for sites with deeper snow cover. The basal ice observations were limited to 0.21 m by the length of the available coring equipment. SWE is computed as the sum of the snow and the basal ice' water equivalent using a mean snow density determined from several snow pits within the study area and the density of pure ice. For sites without basal ice measurements, we use the average d_{ice} of the respective year as a first-order estimate.

3 Model implementation

Here, we describe the extended capabilities of the CryoGrid 3 model, originally presented by Westermann et al. (2016). In this study, we add a more advanced representation of internal snow processes and snow microphysics, based on the parametrizations of the CROCUS snow scheme (Vionnet et al. 2012). The snow scheme of the original CryoGrid 3 model is referred to as "*CG simple snow*", while the version with the new snow scheme is referred to as "*CG Crocus*". Further, we build on the multi-tile version of CryoGrid 3 described in Nitzbon et al. (2019), and implement lateral fluxes of snow due to wind drift and water percolation. Together, these amendments facilitate a process-based representation of internal and lateral snow processes.

3.1 *CG Crocus* snow scheme

In this study, we use a layered snow scheme tailored for the CryoGrid 3 modelling framework, introducing snow microphysics parameterizations from the CROCUS snow scheme (Vionnet et al. 2012) in *CG simple snow*. A comparison of the employed process parametrizations for both snow schemes is presented in Table 1. Following Vionnet et al. (2012), the snow microstructure is described by the snow variables dendricity, d (unitless, range 0-1), sphericity, s (unitless, range 0-1), and grain size, g_s (mm). A more detailed description of internal snow processes and snow microstructure is required to quantitatively determine the potential for wind erosion of the snow layers (Sect. 3.2).

Table 1: Overview of the snow processes for which this study (CG Crocus) differs from the parameterizations used in Nitzbon et al. (2019) (CG simple snow). *refreezing of melt-/rainwater is included in both snow schemes.

	CG simple snow	**CG Crocus**
Short-wave radiation transmission	Single band (Westermann et al., 2016)	Three spectral bands (Vionnet et al., 2012)
Transient albedo	(ECMWF, 2007)	(Vionnet et al., 2012)

Transient density*	Not included	(Vionnet et al., 2012)
Metamorphism	Not included	(Vionnet et al., 2012)
Mechanical settling	Not included	(Vionnet et al., 2012)
Wind compaction	Not included	(Vionnet et al., 2012)

In *CG Crocus*, fresh snow is added with temperature- and wind-speed dependent properties and densities following Vionnet et al. (2012). Once deposited, snow metamorphism is described by quantitative laws detailing the evolution of microstructure of each layer through time depending on temperature gradients and liquid water contents (Vionnet et al., 2012).

Incoming solar radiation in *CG Crocus* is split in three different spectral bands for which reflection and transmission are handled individually (Vionnet et al., 2012). For each band, a spectral albedo for the surface and an absorption coefficient for each layer is calculated from the snow properties, using the snow microstructure variables. Solar radiation that penetrates in the snowpack is gradually absorbed based on the layer-specific absorption coefficient as it passes through the snowpack (Vionnet et al., 2012). At the base of the snowpack, the energy from the remaining solar radiation is added to the lowest snow cell.

Following Vionnet et al. (2012), two mechanical processes that increase the density of snow are included in *CG Crocus*: 1) mechanical settling due to overburden pressure, and 2) modification of snow particles by wind drift. The former gives a compaction of each layer expressed by the vertical stress of overlying layers and the viscosity of the layers, while wind drift increases snow densities in the upper parts of the snowpack due to breakup and rounding of snow particles. For each time step, a mobility index (M_O) is calculated for all layers based on their microstructural properties, quantifying their potential for wind erosion:

$$M_O = \begin{cases} 0.34(0.75d - 0.5s + 0.5) + 0.66F(\rho), & d > 0 \\ 0.34\left(-\frac{0.583}{mm} g_s - 0.833s + 0.833\right) + 0.66F(\rho), & d = 0 \end{cases}$$

(Eq. 1)

where $F(\rho) = 1.25 - 0.0042\,m^3/kg * (\max(\rho_{min},\rho) - \rho_{min})$ and $\rho_{min} = 50\ kg/m^3$. From the mobility index and the wind speed (U), the driftability index (S_I) is computed for each layer:

$$S_I = -2.868 \exp(-0.085\ s/m * U) + 1 + M_O$$

(Eq. 2)

The driftability index discriminates between events of snow drifting ($S_I > 0$) and no snowdrift ($S_I <= 0$). In practice, the effect of snow drift is limited to the upper parts of the snow pack by introducing of a time characteristic of snow drift under wind transport (τ_i), for each layer i:

$$\tau_i = \frac{\tau}{\max\left[0, S_{I,i} \exp\left(-\frac{z_i}{0.1\ m}\right)\right]} \quad ,$$

(Eq. 3)

where τ is an empirically determined time constant and z_i is a pseudo depth that takes into account previous hardening of above lying snow layers. From τ_i the wind induced change of density and microstructure is calculated for each layer (Vionnet et al. 2012). τ_i is thus an indirect measure of the amount of snow that undergoes changes due wind drift, under the assumption that erosion and deposition are equal. We use this in the following section to derive erosion rates for lateral transport of snow.

The primary goal of *CG Crocus* is simulate the ground thermal regime. Other than in the original CROCUS implementation described by Vionnet et al. (2012), we employ a simpler regridding scheme and do not assign a specific snow layer to a snowfall event. Instead, new snow is added to the uppermost grid cell in each timestep, assigning the weighted average between old and new snow for all model variables (g, s, gs, density, etc.). As weighting factor, the amount of ice is employed. When a grid cell exceeds a certain target SWE (0.01 m), it is split in two cells, with resulting grid cell sizes on the order of a few centimeters. With this procedure, small features like weak layers in the snow pack cannot be resolved, but a forcing-dependent density structure develops (which remains consistent when reducing the grid cell size). Vertical water infiltration in the snow pack is handled with a bucket scheme as in *CG simple snow* (Nitzbon et al., 2019).

3.2 Lateral fluxes of snow and water

Building on the setup described in Nitzbon et al. (2019), the aim of the model modifications is to represent the sub-grid distribution of snow and wetness using several model realizations that are coupled by lateral fluxes of snow and water. The modelled overall area is divided in tiles representing distinct terrain units featuring an area A and an altitude a_{rel} relative to the forcing altitude, and a wind exposure e. Each tile is hydrologically connected to its neighbors by hydraulic distances, D^{hy}, and contact lengths, L. Based on this simple setup we calculate bulk lateral fluxes, which are applied after a lateral interaction timestep, Δt_{lat}, which facilitates coupling between different model realizations.

Lateral snow fluxes: In *Nitzbon et al. (2019)*, snow redistribution between tiles is prescribed purely based on differences in altitude and vegetation height between the tiles, disregarding the effect of different wind speeds and snow properties on the erodability of snow layers. This procedure necessarily leads to a spatially variable snow accumulation, even if the snow falls as slush, as typical during warm spells and ROS events on Svalbard (e.g. Eckerstorfer & Christiansen, 2011).

We therefore utilize the wind compaction parameterizations from to describe potential snow erosion in a more physically-based way. For each layer i the fraction of snow that is mobile within a lateral interaction timestep Δt_{lat} is quantified as

$$\theta_{mobile,i} = \frac{N_{drift}}{\tau_i} * \Delta t_{lat}$$

(Eq. 4)

where we introduce an empirical drift factor, N_{drift}, relating the depth dependent time characteristic of each layer (Eq. 4) to the amount of snow that can be removed per time interval. Example erosion rates resulting from this parameterization are provided in the Supporting information for typical snow types and wind speeds. The underlying assumption that the flux of removed snow is inversely proportional to the time characteristic of snow undergoing wind-induced grain and density change is not confirmed by experimental studies. However, it is a simple first-order approximation in qualitative agreement with the original 1D-version of CROCUS, in which wind drifting only occurs for positive driftability indices and increases with both driftability index and proximity to the snow surface.

Whether a tile loses or gains snow due to wind transport depends on its exposure, *e*, which is a quasi-altitude given by $e(t) = e_{init} + d_{snow}(t)$. During each interaction time step, a snow exchange index, I_{drift}, is calculated by the normalized difference of the total area with a higher exposure, A_{above}, and lower exposure, A_{below}, than the respective tile (*i*):

$$I_{drift}(e_i) = \frac{A_{above} - A_{below}}{A_{above} + A_{below}}$$

(Eq. 5)

Tiles with negative snow exchange index loose snow equal to $-\theta_{mobile} * I_{drift}$ for each mobile layer, i.e. the most exposed tile loses all snow that is mobile given the current wind speed. To prevent snow fluxes due to negligibly small differences in tile elevation, a tile is defined to be above (below) the current tile if its exposure is more (less) than a threshold exposure difference, δe, than the current tiles. All eroded snow is added to a pool of "drifting snow" within which the extensive state variables (energy, mass) are summed and the snow properties (d, s, g_s, snow density) are linearly mixed based on the ice mass eroded from each layer. The drifting snow is finally distributed among the receiving tiles based on normalization of their snow exchange index, which assumes that the horizontal dimensions of the modelled area are smaller than the transport distance for blowing snow. As tiles with lower exposure receive more snow, this redistribution results in a gradual leveling of the exposures within the different tiles.

Lateral water fluxes: Lateral flow of water between unfrozen soil columns of adjacent tiles is implemented as in Nitzbon et al. (2019). In an effort to capture the spread of basal ice thickness and GST to ROS events, a similar scheme for water exchange between snow-covered tiles is introduced, taking only the snow cover into account, as the ground is generally frozen when a snow cover is present. Therefore, we assume drainage of water in excess of the field capacity of the ground/soil. Lateral water fluxes occur only between tiles if both feature a snow cover, or both are snow-free and unfrozen (i.e. they feature an unfrozen surface grid cell).

When a water table is present within the snowpack, lateral water fluxes (q_α) to tile α are calculated from Darcy's law, as in Nitzbon et al. (2019):

$$q_\alpha^{hy} = \sum\nolimits_{\beta \in N(\alpha)} K_{snow}^{hy} \frac{w_\beta - \max(w_\alpha, f_\alpha)}{D_{\alpha\beta}^{hy}} \frac{H_{\alpha\beta} L_{\alpha\beta}}{A_\alpha}$$

$$H_{\alpha\beta} = \min[w_\beta - \max(w_\alpha, f_\alpha), w_\beta - f_\beta]$$

[Eqs. 6 and 7]

K_{snow}^{hy} denotes the saturated hydraulic conductivity of snow, *w* the water table, and *f* the elevation of the lowest snow cell with mobile water. $H_{\alpha\beta}$, $D^{hy}_{\alpha\beta}$ and $L_{\alpha\beta}$ are the contact height, hydraulic distance and contact length between two tiles α and β, respectively. The bulk fluxes are scaled to not exceed the available water at the tile that is drained. Water is added to the receiving tile by pooling it up from the base of the snowpack. Lateral advection of heat through water fluxes between tiles is not included.

3.3 Model setup

The goal of the model setup is to capture the end-members of the snow distribution by representing key features of the local topography of the Bayelva area. We divide the study area into three landscape units, exposed ridges (R), snowbeds (S) in depressions and adjacent to slopes, and the ambient (A) surrounding flat terrain. These units are connected to each other in a two-dimensional fashion (Fig. 2), and we assume translational symmetry in the third spatial dimension. Both areas, distances and contact lengths assigned to each tile are loosely based on the profiles in Figure 2, which is a two-dimensional setup that can represent the typical ridge-valley-plain topography of the study area, including typical elevation differences. This partitioning of the landscape does not capture the true distribution of the terrain in the Bayelva area, and processes occurring in the transition zone between the selected topographic features are naturally not included.

The hydrological setup is schematically presented in Figure 3, with the attributes of each tile summarized in Table 2. We further set the wind exposure to the relative altitude, so that redistribution of snow only occurs from higher to lower elevations. This implies that the wind direction and the formation of snow drifts at lee sides of slopes cannot be reproduced. The hydrological setup is adapted for an environment with elevation differences of tens of meters, so in contrast to the lowland setup of Nitzbon et al. (2019), we do not include an external water reservoir in our study and instead remove excess water from the system when the uppermost grid cell is saturated. To assess the added insight of the three-tile simulations we run a standalone control simulation without lateral fluxes (referred to as *single-tile control simulation*), featuring the same configurations as the ambient tile.

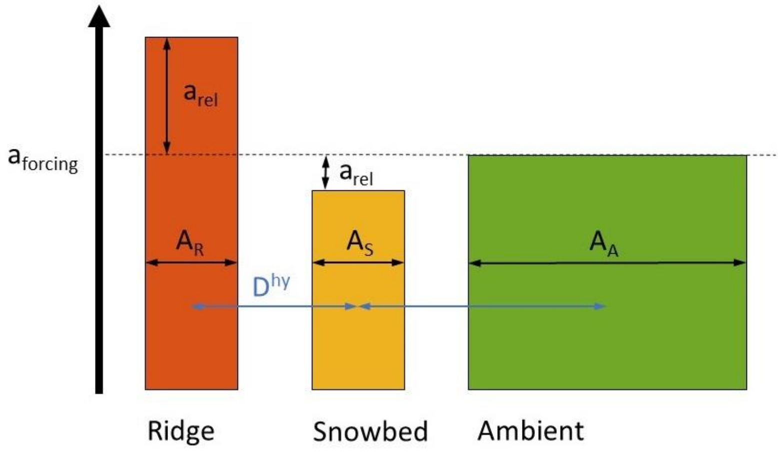

Fig. 3: Schematic cross-section of the setup of the laterally connected three-tile system. Translational symmetry in the second horizontal dimension is assumed.

Table 2: Parameters for topography and hydraulic connections of the tiling scheme.

Parameter	Symbol	Unit	Ridge	Snowbed	Ambient
Area	A	m2	100	100	300
Relative altitude	a_{rel}	m	10	-1.5	0
exposure	e	m	10	-1.5	0
Hydraulic distance	D^{hy}	m		100	200

The modelled soil domain consists of 5 meters of sediments overlying bedrock, which extends down to 100 m below the surface. The stratigraphies (Tables 3, 4) of the tiles are deduced from Boike et al. (2018), and differ only in one aspect, i.e. no organic layer is assigned to the ridge tile, in agreement with field observations. At the lower boundary condition of the model domain, a geothermal heat flux of 0.05 W/m^2 is applied.

Table 3: Subsurface stratigraphy of the snowbed and ambient tiles.

Depth (m)	Mineral fraction	Organic fraction	Field capacity	Soil type	Initial water fraction
0 – 0.1	0.5	0.05	0.2	sand	0.45
0.1 – 5	0.5	0	0.2	sand	0.5
5 – 100	0.97	0	0.03	sand	0.03

Depth (m)	Mineral fraction	Organic fraction	Field capacity	Soil type	Initial water fraction
0 – 5	0.4	0	0.2	sand	0.5
5 – 100	0.97	0	0.03	sand	0.03

Table 4: Subsurface stratigraphy of the ridge tile.

Soil and snow parameters are presented in Table 5, and are to the extent possible taken from Boike et al. (2018), while snow parameters associated with the CROCUS scheme are set to the default value of Vionnet et al. (2012).

Table 5: Model parameters and settings for all simulations.

Parameter	Symbol	Value	Unit	Reference
Soil				
Albedo	α_{soil}	0.15	[-]	Boike et al. (2018)
Emissivity	ε	0.99	[-]	
Roughness length	z_0	0.001	m	Boike et al. (2018)
Root depth	D_T	0.05	m	
Evaporation depth	D_E	0.05	m	
Hydraulic conductivity	K^{hy}	0.00001	m/s	Boike et al. (2018)
Snow				
Emissivity	ε	0.99	[-]	
Roughness length	z_0	0.0001	m	Boike et al. (2018)
Field capacity	θ_{fc}	0.05	[-]	Pahaut (1976)
Hydraulic conductivity	K_{snow}^{hy}	0.001	m/s	Boike et al. (2018)
Time-scale wind drift	τ	48	hours	Vionnet et al. (2012)
Lateral				
Lateral interaction time step	Δt_{lat}	1	hour	
Exposure threshold difference	δe	0.1	m	This study
Drift factor	N_{drift}	5	[-]	This study

3.4 Forcing data

For the Bayelva site, we used forcing data from the AROME-Arctic NWP model, which provides high-resolution (2.5 km) meteorological forecasts especially tailored for the Arctic (Müller et al., 2017). Although AROME-Arctic performs better than other comparable models (Køltzow et al., 2019), its forecast quality is challenged by the general sparsity of observations in the Arctic. This is especially true for precipitation, the evaluation of which is challenging due to shortcomings in measuring solid precipitation in wind-exposed areas as typical for Svalbard.

Our setup requires near-surface meteorological data as forcing at the upper boundary of the model domain, including shortwave radiation, longwave radiation, air temperature, humidity, wind speed, pressure, rain and snowfall. Time series of the required variables are extracted for the closest grid cell with a surface altitude ($a_{forcing}$ = 21 m a.s.l.) comparable to the study area (10 – 50 m. a.s.l) from https://thredds.met.no/thredds/catalog/aromearcticarchive/catalog.html. We duplicate this forcing data set to facilitate a spin up of the model, yielding eight years of forcing data. We initialize the simulations with a temperature profile for late fall derived from measurements from a nearby, instrumented borehole (Boike et al., 2018): 0m, 5°C; -1.7m, 0°C; -10m, -2.5°C. We fix the base of the permafrost to 100m depth, which is a typical value for coastal areas on Svalbard (Liestøl, 1975).

4 Results

4.1 Process-based lateral redistribution of snow and water

We illustrate the differential buildup of the snow cover that is simulated by the newly-implemented lateral transport processes in *CG Crocus*. The key novel feature of *CG Crocus* is the process-based redistribution of snow from higher to lower elevations, of which an example is provided in Figure 4. During calm conditions around February 18 in 2019 (event 1 in Fig. 4), a thin layer of low-density snow accumulates across all tiles. Preferential deposition during snowfall accompanied by high wind speeds is not explicitly handled in our model, but with a lateral interaction timestep of one hour, the accumulation of more and denser snow in the snowbed tile is captured (event 2 in Fig. 4). The thin snow cover on the ridge tile subject to erosion by several windy events, and completely disappears by March 9 (event 3 in Fig. 4). The explicit handling of snow redistribution distinguishes our approach from previous tiling approaches which scale incoming snowfall to obtain a differential snow cover (e.g. Aas et al., 2017).

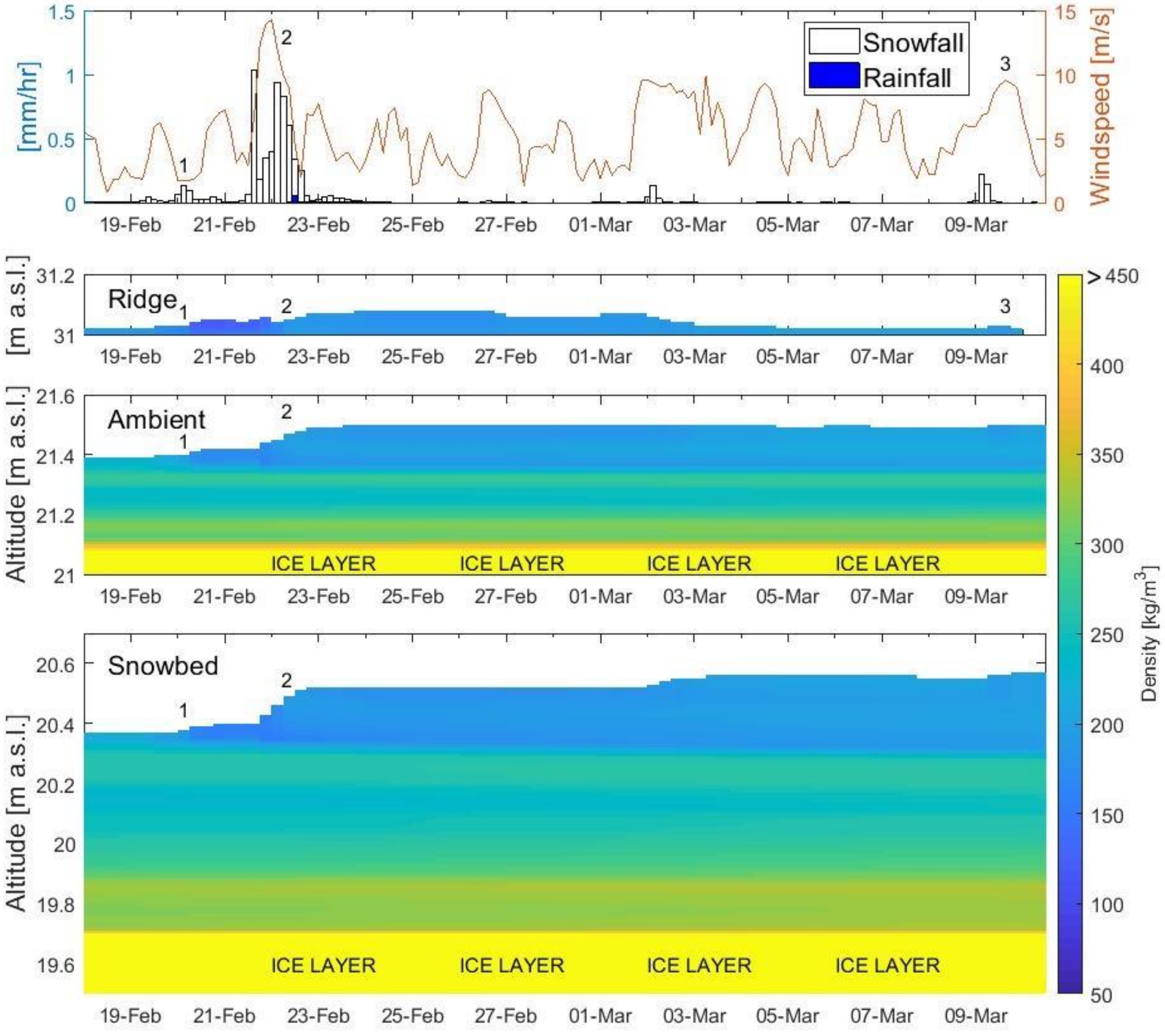

Fig. 4: Example situation for meteorological conditions (3-hourly forcing data; year 2019; top panel) leading to different accumulation and erosion for the three-tile simulation (three lower panels). "*ICE LAYER"* indicates areas with densities > 900kg/m^3.

Another novel feature of *CG Crocus* is the lateral exchange of water between snow covered tiles. Fig. 5 displays an example of the response of the different tiles to a pronounced ROS-event in April 2019. Note that before the event, there is no ice layer in the ridge tile, while the ambient and snowbed tile already feature basal ice layers (10 and 20 cm, respectively). During a smaller ROS-event, the liquid water is retained within the snowpack (event 1 in Fig. 5). When rainfall is heavier, the water percolates to the base of the snowpack where it pools up (event 2 in Fig. 5) and gradually drains to the snowbed tile. The resulting bottom water layer is subsequently insulated from the colder surface temperatures by the thick snow cover, preventing it from refreezing (event 3 in Fig. 5) and resulting in a long-lasting increase in GST for the snowbed tile. Inclusion of this process is key to reproduce the differential buildup of basal ice layers, and the grounds thermal response to ROS-events.

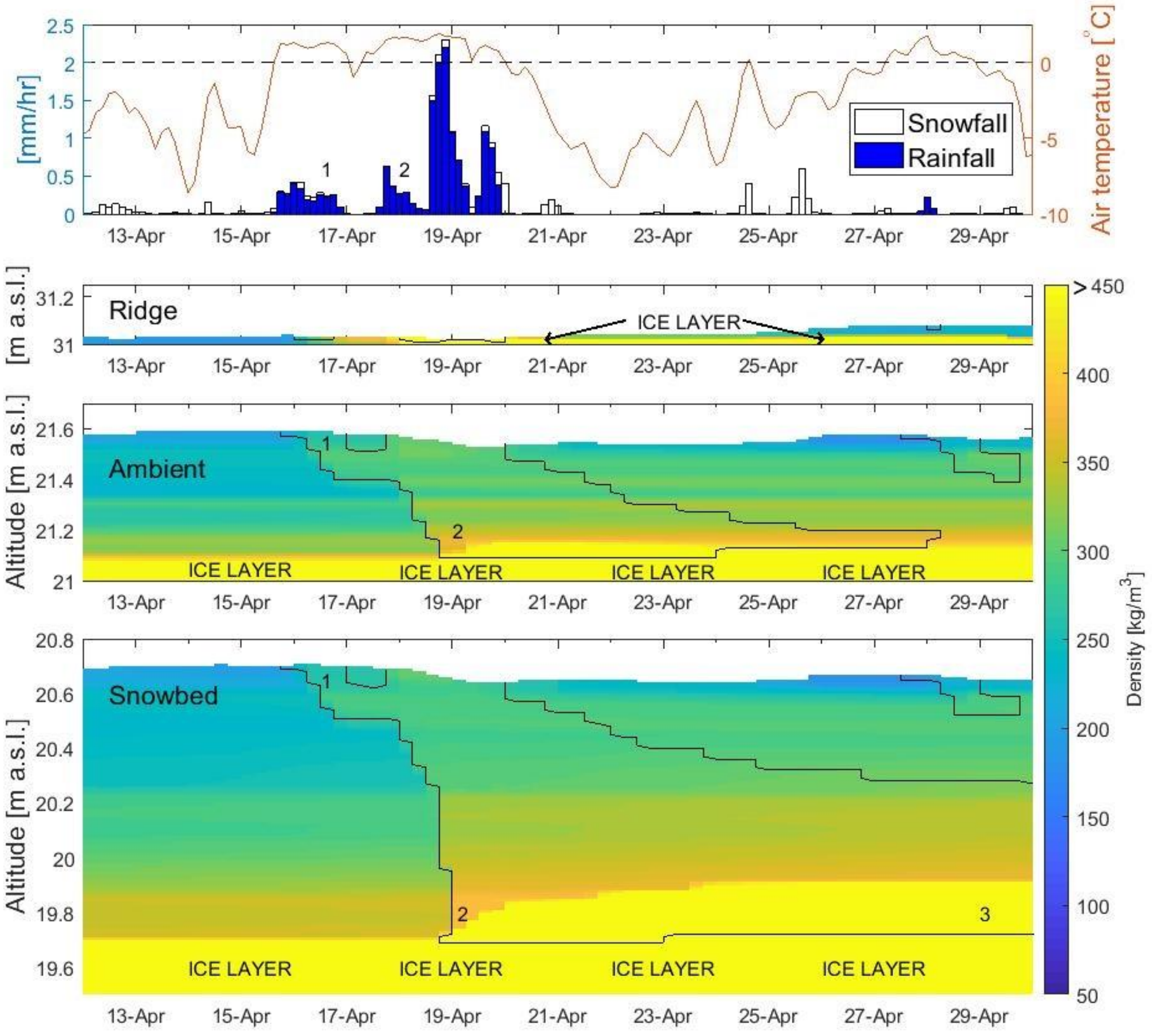

Fig. 5: Example of meteorological conditions (top panel) and snow cover response in the three tiles (lower three panels) during and after a heavy ROS-event in 2019. The text *ICE LAYER* indicates areas with densities > 900kg/m^3. The black line shows the 0°C isotherm, delineating the area where liquid water is present.

4.2 Sub-grid evolution of snow depth and SWE

Here, we compare the transient three-tile simulations against single-tile reference runs and evaluate the simulated end-of-season snow properties to field observations from the Bayelva study site. A comparison of the snow pack evolution for the three simulated snow seasons is presented in Fig. 6. The ambient tile closely follows the *single-tile control simulation*, as its exposure is equal to zero in our setup which prevents redistribution of snow (Eq. 8). The small difference in snow depth between the ambient and 1D simulation is a consequence of ROS-events, during which water cannot drain from the 1D simulation resulting in a higher snow viscosity for the wet snow and subsequent higher compaction rates. The snowbed and ridge tile, on the other hand, differ strongly from the *single-tile control simulation*. The ridge tile experiences multiple cycles of accumulation and subsequent erosion of a thin snow cover, while a thick snow cover accumulates in the snowbed throughout the season. It is also notable that the three-tiled simulations yield a difference of around a month in the melt-out date of the ridge and snowbed tile, which is in broad agreement with satellite derived melt-out curves for the Bayelva area (Aalstad et al., 2018, 2020).

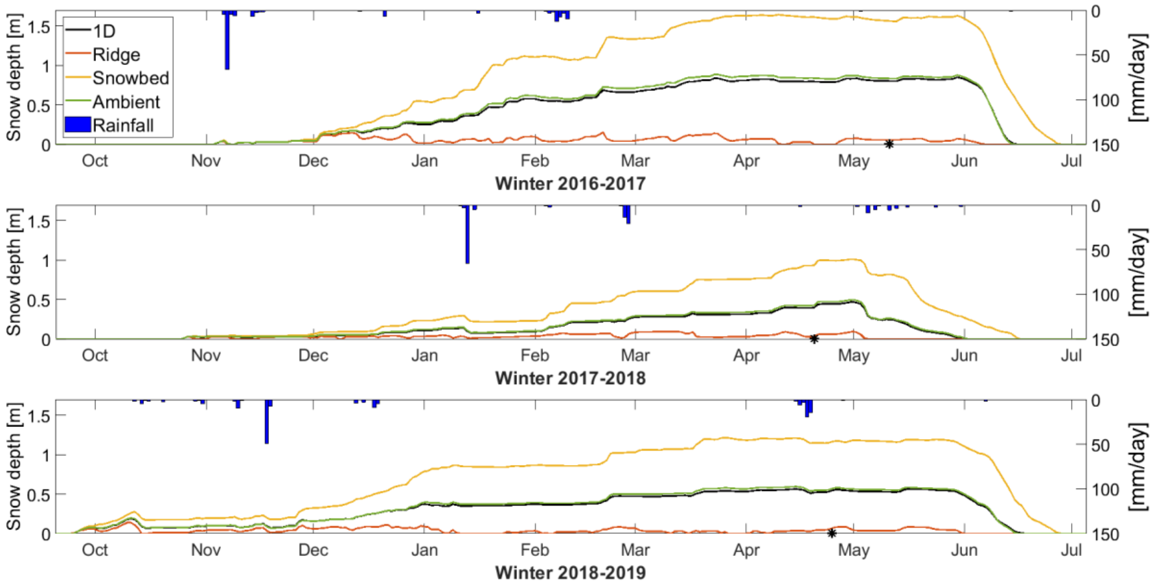

Fig. 6: Modelled daily snow depth evolution (left axis) and ROS-events (right axis), revealing differences in duration and amount of snow cover for the three simulated winters. The black dots indicate the time of the annual snow survey.

Simulated snow depth and SWE are compared to in-situ observations from the Bayelva area (Fig. 7). While snow depth is primarily affected by wind redistribution, SWE is a result of lateral exchange of both snow and water. In the majority of years, the three-tile simulations agree very well with the in-situ measurements for both the width and center of the distribution for snow depth and SWE. The simulations also capture interannual variations between the years, with the snowbed tile closely following the observed maximum for both snow depth and SWE. The ambient tile, which represents the largest area in the simulations, produces snow depths and SWE close to the peak of the observed distributions for all years except 2017.

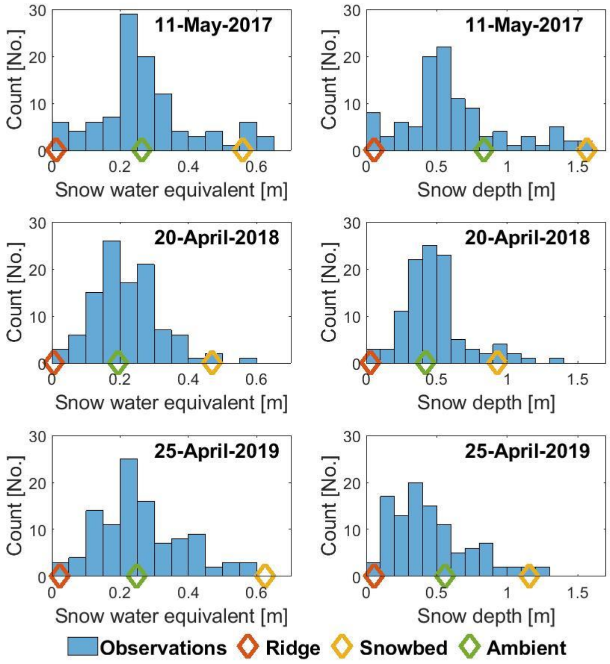

Fig. 7: Histograms of observed SWE (left column) and snow depth (right column) for the hydrological years 2017 to 2019, based on 109 (2017 and 2019) and 108 (2018) measurements conducted around the time of peak snow accumulation. The colored diamonds indicate the corresponding values from the three-tile simulation.

4.3 Sub-grid evolution of ground surface temperatures

We compare simulated GSTs against transient in-situ measurements the Bayelva area for the hydrological years 2017, 2018 and 2019. In Fig. 8, simulated GSTs from the three-tile system are compared to selected quantiles of measurements from more than 90 randomly distributed locations. Throughout most of the year, the simulated GST capture the observed spread very well, showing the influence of topographic features on the thermal regime in the study area. The observations reveal large temporal variations in the spatial differences in wintertime GST, being largest towards the end of winter, a behavior also present in the simulations. The tiling approach is capable to reproduce the observed GST increases to around zero degrees during ROS events, while evolving differently afterwards depending on the preceding snow conditions. Furthermore, the time difference in the final snow melt-out (indicated by the transition of GST to positive values) is represented well in the simulations. During summer, the spatial variation in GSTs is comparatively small, both for the observations and the three-tile simulations. In 2017, the simulated GSTs of both the snowbed and ambient tile are warmer than the observations after a mid-winter ROS-event, which is likely linked to a too thick snow cover in the simulations. Observations from Ny-Ålesund record total precipitation comparable to the output from AROME-Arctic for January (71 and 82 mm, respectively), but indicate no net increase in snow depth (MET.no, 2020), while the ambient and snowbed tile experience a respective increase of 34 and 56 cm. This triggers a substantially different response to the ROS-event in the first week of February, for which the station record from Ny-Ålesund shows a complete melting of the snow cover, while snow with trapped liquid water persists in the simulations for the ambient and snowbed tile.

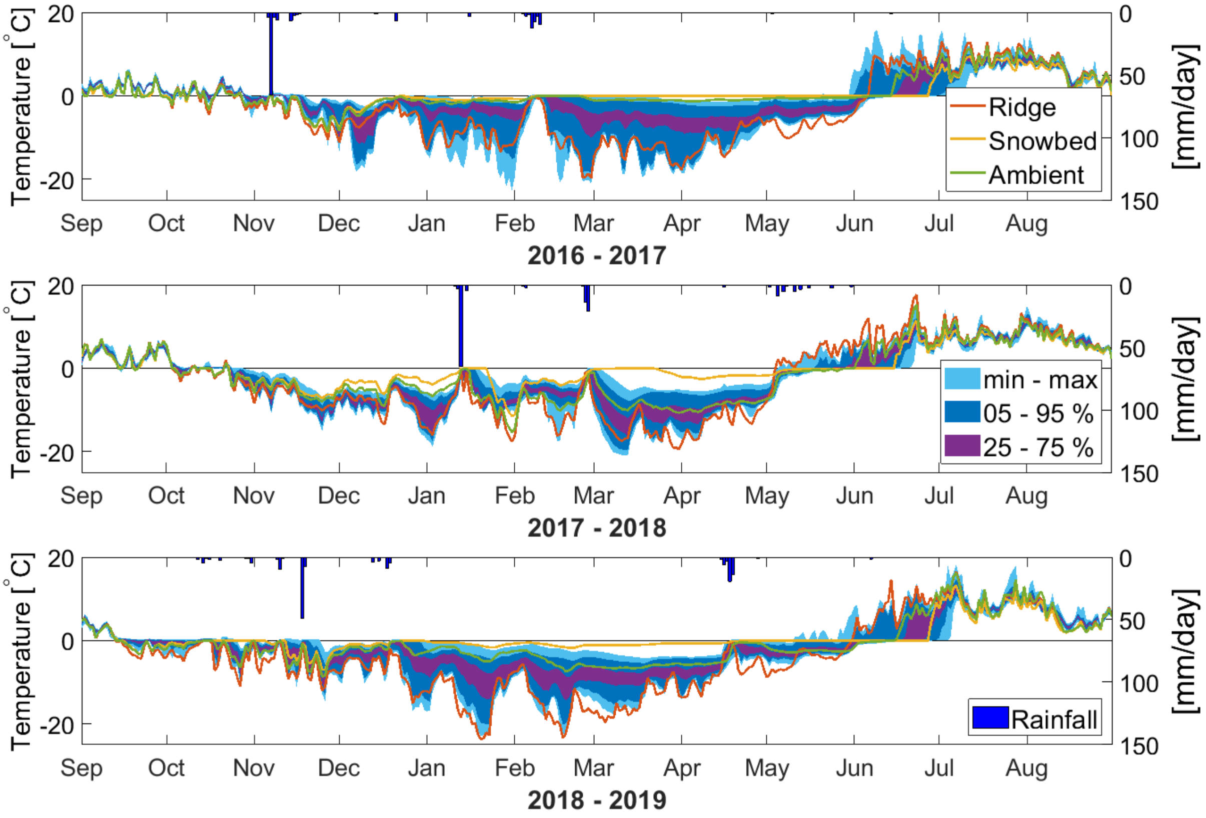

Fig. 8: Observed and simulated GST for the hydrological years 2017 to 2019 (left axis), and ROS-events (right axis). The lines show the simulated daily GSTs, while colored areas respectively delineate the 25-75 and 5-95 quantiles, as well as the minima and maxima of observed daily average GSTs.

Figure 9 shows a systematic comparison between the simulated and observed spatial spread in daily average GST. Although the three-tile setup on average underestimates the spread for days with large spatial GST differences, the simulations can largely represent the observed spatial GST variations in the study area. the spread is reproduced well for the large majority of the days.

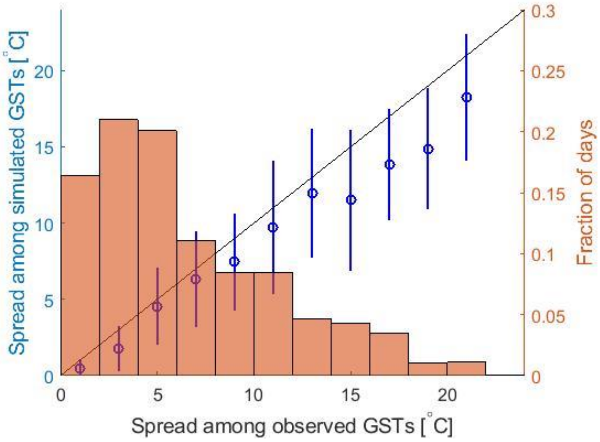

Fig. 9: Simulated vs. observed spread (difference between highest and lowest temperature) of 1096 daily GSTs for bins of 2°C (left axis). The error bars indicate the standard deviation of the simulated values within a bin. The 1:1 line is indicated in black. Histogram: Fraction of days with observed spread in each bin (right axis).

The performance of the tiling approach to reproduce the observed spatial variability is evident when comparing to results of the *single-tile control simulation* (Table 6). The observed temporal averages of GST differ by several degrees within the study area, which is generally well captured by the three-tile setup. The single-tile control run, on the other hand, can by design not reproduce the extremes of the GST distribution, which for these sites results in an over- or underestimation of up to 3°C. In particular, the three-tile model reproduces the positive average GSTs observed for the warm edge of the distribution, which could indicate the onset of permafrost degradation at localized spots within the study area (if the GST pattern persisted for more years). The single-tile simulations, on the other hand, can only deliver a single GST value which suggests warm, but thermally stable permafrost (Table 6).

Table 6: Comparison of simulated (three-tile and single-tile reference simulations) and observed average GST for the entire study period (2017-2019) for selected quantiles of the observed distribution.

Observations		Simulations, three-tile			Simulations, single-tile	
Quantile	average GST	tile	average GST	difference	average GST	difference
5%	-3.90 °C	Ridge	-3.23 °C	-0.67 °C	-0.87 °C	-3.03 °C
50%	-1.56 °C	Ambient	-0.51 °C	-1.05 °C		-0.69 °C
95%	0.63 °C	Snowbed	0.49 °C	0.14 °C		1.50 °C

A more detailed comparison of simulated and observed mean annual ground surface temperature (MAGST), freezing degree-days (FDD) and thawing degree-days (TDD) is shown in Figure 10. In general, the tiling approach is able to reproduce the annual spatial range and year-to-year variations of these metrics. During winter, the ambient tile is generally warmer than the average of the measured distribution, most notably in 2017. As the spread in summer temperatures is small, TDDs are primarily controlled by the timing of the melt-out in spring, which is captured by the simulations (Fig. 8).

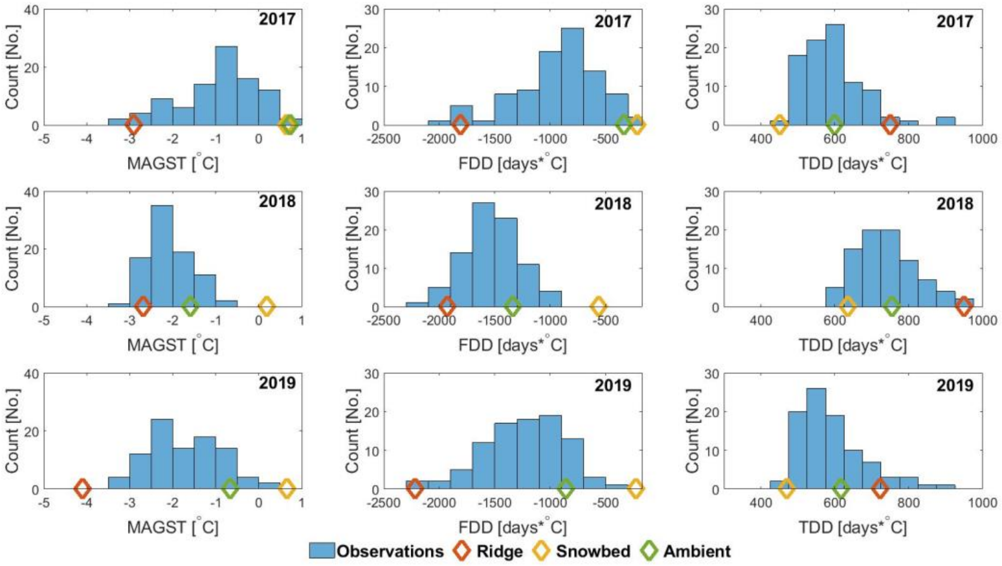

Fig. 10: Results from the three-tile simulation (colored diamonds) and histograms of observed MAGST, FDD and TDD for the hydrological years 2017 to 2019. Only observations from loggers which

provide valid measurements for at least 360 days of each of the year are included, yielding 92 GST loggers in 2017, 85 in 2018 and 92 in 2019.

5 Discussion

5.1 Representing snow cover variability with laterally coupled tiles

In the three-tile setup of *CG Crocus*, lateral fluxes of snow and water are simulated between idealized tiles which represent the spatial variability of the terrain in a simplified way as a ridge-depression-plain system. Ground and surface properties in the simulations are similar for all tiles, so that the effect of lateral snow and water fluxes can easily be identified. Fig. 6 provides clear evidence that this setup can yield crucial additional information on the spatial variability of snow cover compared to the single-tile control case. Despite of the simple geometric setup, the three-tile setup of *CG Crocus* is able to reproduce the key characteristics of the spatial variations in GST (Figs. 8, 9, 10), with a smaller spread during summer and in the early snow season, while the spread in GST is large following mid-winter ROS events and during spring melt out. This transient, process-based representation of sub-grid variability is a novel feature not possible with standard one-dimensional (i.e. single-tile) land surface models (e.g. Westermann et al., 2016).

A more accurate way to model sub-grid snow distribution would be to resolve the lateral process in a true two- or three-dimensional fashion on a meter-scale model grid. Such approaches provide a much more complete representation of the sub-grid variability (e.g. ALPINE3D; Lehning et al. (2006)), but are computationally expensive and therefore challenging to apply over large areas and/or long time series. An example of a gridded model featuring snow redistribution which successfully has been applied over large areas is SnowModel (Liston & Elder, 2006), but here the snow transport is only determined by the meteorological forcing and empirical vegetation parameters and does not take spatial and temporal differences in erodability due to snow microstructure into account. With the presented three-tile setup, the computational cost of CG Crocus is roughly increased by factor of three compared to the single-tile control simulation. However, each model realization can be run on a separate core in a parallel computing environment, so that it only inflicts a limited additional computing time.

Many model approaches that incorporate the effect of sub-grid snow distribution require observations of the snow distribution as input (e.g. Gisnås et al., 2014), or scale the snowfall based on a predefined distribution function (e.g. Aas et al., 2017; Obu et al., 2019). A weakness of such statistical approaches is the underlying assumption that the snow distribution function is constant throughout the development of the snow cover, while in reality it evolves transiently depending on meteorological conditions. In *CG Crocus*, snowfall covers the landscape uniformly, and is only redistributed when snow properties and meteorological conditions permit wind drift of snow. The bulk effect of snow redistribution is a function of the topological parameters assigned to the tiles (Table 2), and these need to be selected to fit the landscape characteristics of the study area, based on topographic information. Rather than prescribing a snow distribution, *CG Crocus* produces forcing-dependent estimates of the mean and the end-members of observed snow depth and SWE distribution (e.g. Fig. 7).

The representation of lateral exchange in *CG Crocus* reveals obvious shortcomings, which likely explain some of the discrepancies between observed and modelled GSTs (Fig. 8). Lateral water fluxes do not occur between snow-covered and snow-free tiles, which implies that the ridge tile does not drain down-slope in the roughly one month long period when the ridge is already snow-free, but the snowbed tile is still snow-covered. Still, for most years, the ridge tile captures the high GST observed in early summer for already snow-free surfaces, with the remaining difference possibly due to the assumption of flat and horizontal surfaces, while differences in slope and aspect do occur in reality. In the three-tile configuration, CG Crocus only accounts for first-order processes governing local snow and GST distribution, while a true representation of the sub-grid variation in surface texture and exposition would require strongly increasing the number of tiles and thus computation time.

Furthermore, the representation of GST during ground freezing is limited by the assumption of effective and instantaneous drainage of surface water (i.e. excess water when the soil column is saturated), while water likely pools up at some locations in reality (as observed in the field in September/October 2009). An example is the period mid-September to mid-October 2018 when all tiles feature subzero temperature, while observations show 0°C at some locations. This could be improved by implementing formation (and freezing) of a temporary layer of surface water, but would also require additional parameterizations for drainage. In addition, CG Crocus does not capture the cold near-zero GST recorded after melt out in some locations (Fig. 8), which might be related to lateral advection of snow melt water from still snow-covered locations, which is not accounted for in CG Crocus.

In the parameterization of lateral snow transport a drift factor, N_{drift}, is introduced to relate the parameterizations from CROCUS to the snow amount eroded during a lateral interaction timestep. N_{drift} is a purely empirical constant which is set to 5 in our simulations to reproduce the observed spread in snow depths. While the exact value is by no means determined by this study alone, we note that the sensitivity of N_{drift} towards GST is not strong. In the example of 2019, a doubling of N_{drift} to 10 increases the MAGST of the snowbed tile by 0.125°C and decreases the MAGST of the ridge tile by 0.035°C. If N_{drift} is halved to 2.5, the MAGST is decreased by 0.182°C for the snowbed and increased by 0.545°C for the ridge tile. The most pronounced effect of changing the N_{drift} is found at the ridge, as it primarily controls the efficiency at which erodable snow is evacuated (see Supporting information). At the ridge a lowering of the drift factor results in longer periods with a thin snow layer covering the ground, while increasing the drift factor beyond $N_{drift} = 5$ has a marginal effect as the amount of available snow is already the limiting factor. The snow depth fluctuates between < 3 and 15 cm during winter for all the presented drift factors, which is in qualitative agreement with observations from Svalbard. In principle, this drift factor could be determined from observations of wind speed and snow erosion in conjunction with pre-drift surveys of the snow properties, either in the field and/or lab environments.

The performance of CG Crocus is influenced by uncertainties in the available forcing data. We have used forcing from the AROME-Arctic NWP model, which is demonstrated to perform well in the Arctic (Køltzow et al., 2019), but also this model is limited by sparse observations for data assimilation and validation (Müller et al., 2017). Our application is especially sensitive to snowfall rates and wind speeds, as these are key to simulate the wind redistribution of snow. Thus, Fig. 7 suggests that AROME-Arctic produces realistic estimates of accumulated wintertime precipitation wind speed, as the center and range of the SWE distribution are successfully reproduced. Nevertheless, the forcing data are likely a limiting factor for model performance at the study area.

The representation of the Bayelva study area by only three landscape units can not capture the true distribution of the lateral processes. A critical point is the assumption that the exposure e_{init} (See Table 2) of each tile is only determined by its relative altitude, which necessarily makes the snowbed tile the receiver of both redistributed snow and percolating water. While this is in agreement with high snow depths in in topographic depressions, snowbeds are also observed at the lee-sides of slopes, which cannot be represented with the simple altitude-dependent exposure formulation. In situations where lateral water percolation occurs, a snowbed located on a lee-side would experience a throughput of water from higher to lower elevations, whereas the snowbed in the three-tile simulation is the receiver of water from all adjacent tiles. Thus, the simulated snowbed is subject to accumulation of liquid water, which gives rise to a prolonged zero-degree curtain effect while water refreezes. This could partly explain why the simulated GSTs for the snowbed tile are higher than the observed maxima of GST following pronounced ROS events (e.g. winter 2018 in Fig. 8). Future improvements of CG Crocus should therefore target a more realistic formulation for the exposure, taking especially the wind direction during drift events and the relative position of adjacent tiles into account.

In CG Crocus, the total mass of snow within the computational domain is conserved during drift events, not accounting for increased sublimation. Tabler (1994) found that more than half of the drifting snow sublimated over fetches of 3km, which needs to be considered in particular for systems with greater transport distances. This can be achieved by removing snow from a "drifting snow pool" following Gordon et al. (2006), or by empirically prescribing a transport distance – sublimation loss dependency (Tabler, 1994). In addition to sublimation losses, conservation of snow mass also relies on the assumption of net zero exchange of snow between the simulated domain and its surroundings. It is unclear to what extent drifting snow is conserved within the wider Bayelva area, but sites with other landscape characteristics, especially above cliffs/terrain edges or near ice-free water bodies, clearly experience a significant net loss of snow for certain wind directions. Such loss of snow to the surroundings could be simulated in CG Crocus by adding a "ghost" tile with a prescribed negative exposure whose only function is to remove snow from the system. Inclusion of these processes might amend the previously mentioned discrepancies between observed (in Ny-Ålesund) and simulated snow accumulation during January 2017, despite observed and modeled precipitation of similar magnitude (Sect. 4.3).

5.2 Outlook

The tiling setup of CG Crocus makes it possible to simulate observed small-scale differences in snow depth, basal ice layers and GST in a more physically-based fashion than traditional one-dimensional models. It builds on the excellent capabilities of the snow microphysics scheme CROCUS (Vionnet et al., 2012), which has been successfully applied in a wide range of climate conditions (e.g. Brun et al., 2013). Therefore, the tiled version of *CG Crocus* can potentially perform well also in other environments with cold climate which should be investigated in future studies.

The simple three-tile setup presented in this study can become a tool to assess the extended environmental impacts of ROS-events in a much more realistic fashion than single-tile models. In a realistic terrain configuration, CG Crocus simulations could broadly identify the terrain features experiencing complete melt out, basal ice formation or internal refreezing during and after ROS-events, which could help quantifying the stress on plant communities by basal ice formation, increased ground surface temperatures or exposure to the atmosphere in case of melt out. Thus, CG Crocus might be able to resolve a variety of processes relevant for Arctic browning at an appropriate scale (Phoenix & Bjerke, 2016; Treharne et al., 2019), making it a useful tool for process-based studies of this phenomenon. In addition, the approach can quantify the extent and distribution of "ice-locked pastures", i.e. the area inaccessible for herbivore grazing due to basal ice presence. Studies focusing on these effects often rely on measurements of snow properties towards the end of the snow season (e.g. Hansen et al., 2011; Loe et al., 2016; Putkonen et al., 2009), while CG Crocus could in addition shed light on the time evolution of ROS-impacts.

In addition, the presented model setup with laterally coupled tiles shows significant potential to improve simulations of permafrost thaw. The simulated GSTs suggest that the three-tile setup are capable to detect spatially localized thaw (Table 6), which would be obscured in traditional single-tile simulations. While simulations can not deliver the full spatial distribution of temperatures at and below the ground surface (e.g. MAGST, Fig. 10), they can represent the edges of the distribution, so that localized onset of permafrost thaw can be detected. In principle, more model tiles could be added to eventually yield a full temperature distribution, but such an ensemble would have to be carefully selected for each study area, while increasing complexity and computation time. For many applications, the three-tile setup might therefore be a reasonable compromise between model complexity and its capacity to reproduce observations.

In particular, CG Crocus could improve thermal simulations of selected landforms in permafrost regions. The thaw dynamics of polygonal tundra, thermokarst lakes, peat plateaus and palsas have previously been simulated with tiled version of CryoGrid 3 and other land surface schemes, including different formulations to achieve spatially variable snow depths. Aas et al. (2019) scaled incoming snowfall, while Martin et al., (2019) removed snow above an observed threshold and Nitzbon et al. (2019) phenomenologically calculated lateral snow transport based only on differences in surface elevation during snowfall. The first two approaches require observations of snow depths, while the latter disregards the control of internal snow properties on its erodability. It is highly likely that CG Crocus could simulate snow accumulation and snow internal processes for these landforms in a much more process based way than previous approaches. We emphasize that the tile areas and relative altitudes can be adapted for each landscape or landform (Aas et al., 2019, Nitzbon et al., 2019) which underlines its potential to perform well in a range of environments.

In principle, the presented tiling setup could also be expanded to simulate larger areas by adding more coupled tiles. For the Bayelva area, the key terrain features defining the model tiles were selected manually, while an automated routine would be required for more extensive or complex landscapes. Clustering techniques as presented by Fiddes & Gruber (2012) could for example be applied for both forcing data and terrain features (e.g. defined by slope, aspect, curvature and relative elevation) which could be an objective way to define model tiles. For large areas where the assumption of uniform meteorological conditions is no longer applicable, tiles can be assigned different model forcing which could facilitate a smooth transition between the spatial scales of available forcing data and representative landscape units.

The presented model framework holds significant potential for more realistic projections on the impacts of climate change in cold environments. Instead of prescribing lateral fluxes of snow independent of snow and weather conditions (as e.g. in Nitzbon et al., 2019), CG Crocus takes the impact of the changing meteorological forcing on snow transport explicitly into account. As parts the Arctic are projected to experience an increase in winter rainfall in the future (Bintanja & Andry, 2017), the erodability of the snow is likely to change, which in turn affects the resulting spatial distribution of snow depth and SWE. By utilizing simple, yet process-based exchange formulations for snow and water, CG Crocus has the potential to enhance our predictive capabilities on climate change impacts on snow-dominated ecosystems.

6 Conclusion

Snow microphysics parametrizations from the CROCUS snow scheme (Vionnet et al., 2012) are implemented in the CryoGrid 3 permafrost model to facilitate a more realistic evolution of the snow cover. Using the tiling capabilities of CryoGrid, lateral fluxes of snow and water are exchanged between three parallel realizations to simulate sub-grid variations in snow cover. Snow removal rates depend on microstructural properties of the snow, as well as the wind speed. Modelled snow pack properties and ground surface temperatures are compared to spatially distributed observations at the Bayelva high Arctic research site on Svalbard, using a *single-tile control simulation* to benchmark model improvements. From this study, the following main conclusions can be drawn:

1. During wind drift events, snow is removed from the high-lying model tile and deposited in the low-lying model tile which produces spatial differences in snow depth in a process-based fashion.
2. Rain-on-snow events lead to spatially different basal ice layers, with ice thickness being lowest for the high-lying model tile.
3. Redistribution of snow to a large extent reproduces the end-members and center the observed distributions of snow cover and ground surface temperatures.

The presented scheme can provide a process-based representation of snow cover variability, which constitutes a novel tool for investigating the climate change impacts on permafrost and high-latitude ecosystems. The scheme is flexible and can be adapted for application over larger areas, other geographic regions, specific landforms or topographic settings.

Acknowledgement

We acknowledge funding by an Arctic Field Grant (Research Council of Norway, no. 295839), PERMANOR (Research Council of Norway, no. 255331), Nunataryuk (EU grant agreement no. 773421), and the Department of Geosciences, University of Oslo. This work is a contribution to the strategic research initiative LATICE (Faculty of Mathematics and Natural Sciences, University of Oslo, mn.uio.no/latice).

The authors declare no conflicts of interests.

The CryoGrid source code is available under the DOI: 10.5281/zenodo.3782425.

Data from field observations are archived under the DOI: 10.11582/2020.00024.

Author Contributions:

RBZ designed the study, retrieved the forcing data, developed the model code, wrote the initial draft and prepared all figures; SW designed the observation array, and provided help and ideas at all phases of the study; JN, ML and SW designed the parallelized version of the CryoGrid model; JB provided data and model parameters for the study area; TVS provided code for retrieving forcing data; SW, RBZ, BE, JB and TVS conducted the observations of snow and GST in the Bayelva area. All authors contributed to the final manuscript with input, suggestions and text.

References

Aalstad, K., Westermann, S., & Bertino, L. (2020). Evaluating satellite retrieved fractional snow-covered area at a high-Arctic site using terrestrial photography. *Remote Sensing of Environment*, *239*. https://doi.org/10.1016/j.rse.2019.111618

Aalstad, K., Westermann, S., Schuler, T. V., Boike, J., & Bertino, L. (2018). Ensemble-based assimilation of fractional snow-covered area satellite retrievals to estimate the snow distribution at Arctic sites. *The Cryosphere*, *12*(1), 247–270. https://doi.org/10.5194/tc-12-247-2018

Aas, Kjetil S., Martin, L., Nitzbon, J., Langer, M., Boike, J., Lee, H., Berntsen, T. K., & Westermann, S. (2019). Thaw processes in ice-rich permafrost landscapes represented with laterally coupled tiles in a land surface model. *The Cryosphere*, *13*(2), 591–609. https://doi.org/10.5194/tc-13-591-2019

Aas, Kjetil Schanke, Gisnås, K., Westermann, S., & Berntsen, T. K. (2017). A tiling approach to represent subgrid snow variability in coupled land surface-atmosphere models. *Journal of Hydrometeorology*, *18*(1), 49–63. https://doi.org/10.1175/JHM-D-16-0026.1

Bintanja, R., & Andry, O. (2017). Towards a rain-dominated Arctic. *Nature Climate Change*, *7*(4), 263–267. https://doi.org/10.1038/nclimate3240

Boike, J., Juszak, I., Lange, S., Chadburn, S., Burke, E., Paul Overduin, P., Roth, K., Ippisch, O., Bornemann, N., Stern, L., Gouttevin, I., Hauber, E., & Westermann, S. (2018). A 20-year record (1998-2017) of permafrost, active layer and meteorological conditions at a high Arctic permafrost research site (Bayelva, Spitsbergen). *Earth System Science Data*, *10*(1), 355–390. https://doi.org/10.5194/essd-10-355-2018

Brun, E., Martin, E., Simon, V., Gendre, C., & Coleou, C. (1989). An Energy and Mass Model of Snow Cover Suitable for Operational Avalanche Forecasting. *Journal of Glaciology*, *35*(121), 333–342. https://doi.org/10.3189/s0022143000009254

Brun, Eric, Vionnet, V., Boone, A., Decharme, B., Peings, Y., Valette, R., Karbou, F., & Morin, S. (2013). Simulation of northern Eurasian local snow depth, mass, and density using a detailed snowpack model and meteorological reanalyses. *Journal of Hydrometeorology*, *14*(1), 203–219. https://doi.org/10.1175/JHM-D-12-012.1

Clark, M. P., Hendrikx, J., Slater, A. G., Kavetski, D., Anderson, B., Cullen, N. J., Kerr, T., Örn Hreinsson, E., & Woods, R. A. (2011). Representing spatial variability of snow water equivalent in hydrologic and land-surface models: A review. In *Water Resources Research* (Vol. 47, Issue 7). John Wiley & Sons, Ltd. https://doi.org/10.1029/2011WR010745

ECMWF. (2007). Part IV: Physical Processes. In *IFS Documentation CY31R1*. ECMWF. https://www.ecmwf.int/node/9221

Fiddes, J., & Gruber, S. (2012). TopoSUB: a tool for efficient large area numerical modelling in complex topography at sub-grid scales. *Geoscientific Model Development*, *5*(5), 1245–1257. https://doi.org/10.5194/gmd-5-1245-2012

Førland, E. J., Benestad, R., Hanssen-Bauer, I., Haugen, J. E., & Skaugen, T. E. (2011). Temperature and Precipitation Development at Svalbard 1900–2100. *Advances in Meteorology*, *2011*, 1–14. https://doi.org/10.1155/2011/893790

Gisnås, K., Westermann, S., Schuler, T. V., Litherland, T., Isaksen, K., Boike, J., & Etzelmüller, B. (2014). A statistical approach to represent small-scale variability of permafrost temperatures due to snow cover. *The Cryosphere*, *8*(6), 2063–2074. https://doi.org/10.5194/tc-8-2063-2014

Gordon, M., Simon, K., & Taylor, P. A. (2006). On snow depth predictions with the Canadian Land Surface Scheme including a parametrization of blowing snow sublimation. *Atmosphere - Ocean*, *44*(3), 239–255. https://doi.org/10.3137/ao.440303

Hachem, S., Duguay, C. R., & Allard, M. (2012). Comparison of MODIS-derived land surface temperatures with ground surface and air temperature measurements in continuous permafrost terrain. *Cryosphere*, *6*(1), 51–69. https://doi.org/10.5194/tc-6-51-2012

Hansen, Brage B., Isaksen, K., Benestad, R. E., Kohler, J., Pedersen, Å., Loe, L. E., Coulson, S. J., Larsen, J. O., & Varpe, Ø. (2014). Warmer and wetter winters: Characteristics and implications of an extreme weather event in the High Arctic. *Environmental Research Letters*, *9*(11). https://doi.org/10.1088/1748-9326/9/11/114021

Hansen, Brage Bremset, Aanes, R., Herfindal, I., Kohler, J., Sæther, B. E., & Oli, M. K. (2011). Climate, icing, and wild arctic reindeer: Past relationships and future prospects. *Ecology*, *92*(10), 1917–

1923. https://doi.org/10.1890/11-0095.1

Hanssen-Bauer, I., Førland, E. J., Hisdal, H., Mayer, S., Sandø, A. B., & Sorteberg, A. (2019). *Climate in Svalbard 2100* (Issue 1).

Køltzow, M., Casati, B., Bazile, E., Haiden, T., & Valkonen, T. (2019). An NWP Model Intercomparison of Surface Weather Parameters in the European Arctic during the Year of Polar Prediction Special Observing Period Northern Hemisphere 1. *Weather and Forecasting*, *34*(4), 959–983. https://doi.org/10.1175/WAF-D-19-0003.1

Lehning, M., Völksch Ingo, I., Gustafsson, D., Nguyen, T. A., Stähli, M., & Zappa, M. (2006). ALPINE3D: A detailed model of mountain surface processes and its application to snow hydrology. *Hydrological Processes*, *20*(10), 2111–2128. https://doi.org/10.1002/hyp.6204

Liestøl, O. (1975). Pingos, springs, and permafrost in Spitsbergen. *Norsk Polarinstitutts Årbok*, 7–29.

Loe, L. E., Hansen, B. B., Stien, A., Albon, S. D., Bischof, R., Carlsson, A., Irvine, R. J., Meland, M., Rivrud, I. M., Ropstad, E., Veiberg, V., & Mysterud, A. (2016). Behavioral buffering of extreme weather events in a high-Arctic herbivore. *Ecosphere*, *7*(6). https://doi.org/10.1002/ecs2.1374

Martin, L. C. P., Nitzbon, J., Aas, K. S., Etzelmüller, B., Kristiansen, H., & Westermann, S. (2019). Stability Conditions of Peat Plateaus and Palsas in Northern Norway. *Journal of Geophysical Research: Earth Surface*, *124*(3), 705–719. https://doi.org/10.1029/2018JF004945

MET.no. (2020). *Yr - "Ny-Ålesund" - historikk*. https://www.yr.no/nb/historikk/graf/1-2837778/Norge/Svalbard/Svalbard/Ny-Ålesund?q=2017

Müller, M., Batrak, Y., Kristiansen, J., Køltzow, M. A. Ø., Noer, G., & Korosov, A. (2017). Characteristics of a convective-scale weather forecasting system for the European Arctic. *Monthly Weather Review*, *145*(12), 4771–4787. https://doi.org/10.1175/MWR-D-17-0194.1

Nitzbon, J., Langer, M., Westermann, S., Martin, L., Aas, K. S., & Boike, J. (2019). Pathways of ice-wedge degradation in polygonal tundra under different hydrological conditions. *The Cryosphere*, *13*(4), 1089–1123. https://doi.org/10.5194/tc-13-1089-2019

Obu, J., Westermann, S., Bartsch, A., Berdnikov, N., Christiansen, H. H., Dashtseren, A., Delaloye, R., Elberling, B., Etzelmüller, B., Kholodov, A., Khomutov, A., Kääb, A., Leibman, M. O., Lewkowicz, A. G., Panda, S. K., Romanovsky, V., Way, R. G., Westergaard-Nielsen, A., Wu, T., … Zou, D. (2019). Northern Hemisphere permafrost map based on TTOP modelling for 2000–2016 at 1 km2 scale. In *Earth-Science Reviews* (Vol. 193, pp. 299–316). Elsevier B.V. https://doi.org/10.1016/j.earscirev.2019.04.023

Osborne, E., Richter-Menge, J., & Jeffries, M. (2018). Arctic Report Card 2018. In *NOAA*.

Pahaut, E. (1976). La métamorphose des cristaux de neige (Snow crystal metamorphosis). *Monographies de La Météorologie Nationale*, *96*.

Phoenix, G. K., & Bjerke, J. W. (2016). Arctic browning: extreme events and trends reversing arctic greening. *Global Change Biology*, *22*(9), 2960–2962. https://doi.org/10.1111/gcb.13261

Pörtner, H.-O., Roberts, D. C., Masson-Delmotte, V., Zhai, P., Tignor, M., Poloczanska, E., Mintenbeck, K., Alegría, A., Nicolai, M., Okem, A., Petzold, J., Rama, B., & Weyer, N. M. (2019). *IPCC Special Report on the Ocean and Cryosphere in a Changing Climate*.

Putkonen, J., & Roe, G. (2003). Rain-on-snow events impact soil temperatures and affect ungulate survival. *Geophysical Research Letters*, *30*(4). https://doi.org/10.1029/2002GL016326

Putkonen, Jaakko, Grenfell, T. C., Rennert, K., Bitz, C., Jacobson, P., & Russell, D. (2009). Rain on

Snow: Little Understood Killer in the North. *Eos, Transactions American Geophysical Union*, *90*(26), 221–222. https://doi.org/10.1029/2009EO260002

Tabler, R. D. (1994). *Design Guidelines for the Control of Blowing and Drifting Snow*.

Treharne, R., Bjerke, J. W., Tømmervik, H., Stendardi, L., & Phoenix, G. K. (2019). Arctic browning: Impacts of extreme climatic events on heathland ecosystem CO_2 fluxes. *Global Change Biology*, *25*(2), 489–503. https://doi.org/10.1111/gcb.14500

Trofaier, A. M., Westermann, S., & Bartsch, A. (2017). Progress in space-borne studies of permafrost for climate science: Towards a multi-ECV approach. *Remote Sensing of Environment*, *203*, 55–70. https://doi.org/10.1016/j.rse.2017.05.021

Vikhamar-Schuler, D., Hanssen-Bauer, I., Schuler, T. V., Mathiesen, S. D., & Lehning, M. (2013). Use of a multilayer snow model to assess grazing conditions for reindeer. *Annals of Glaciology*, *54*(62), 214–226. https://doi.org/10.3189/2013AoG62A306

Vikhamar-Schuler, Dagrun, Isaksen, K., Haugen, J. E., Tømmervik, H., Luks, B., Schuler, T. V., & Bjerke, J. W. (2016). Changes in winter warming events in the nordic arctic region. *Journal of Climate*, *29*(17), 6223–6244. https://doi.org/10.1175/JCLI-D-15-0763.1

Vionnet, V., Brun, E., Morin, S., Boone, A., Faroux, S., Le Moigne, P., Martin, E., & Willemet, J. M. (2012). The detailed snowpack scheme Crocus and its implementation in SURFEX v7.2. *Geoscientific Model Development*, *5*(3), 773–791. https://doi.org/10.5194/gmd-5-773-2012

Westermann, S., Boike, J., Langer, M., Schuler, T. V., & Etzelmüller, B. (2011). Modeling the impact of wintertime rain events on the thermal regime of permafrost. *The Cryosphere*, *5*(4), 945–959. https://doi.org/10.5194/tc-5-945-2011

Westermann, S., Langer, M., Boike, J., Heikenfeld, M., Peter, M., Etzelmüller, B., & Krinner, G. (2016). Simulating the thermal regime and thaw processes of ice-rich permafrost ground with the land-surface model CryoGrid 3. *Geoscientific Model Development*, *9*(2), 523–546. https://doi.org/10.5194/gmd-9-523-2016